Theoretical and observational study of supersoft X-ray sources

Dissertation

der Mathematisch-Naturwissenschaftlichen Fakultät
der Eberhard Karls Universität Tübingen
zur Erlangung des Grades eines
Doktors der Naturwissenschaften
(Dr. rer. nat.)

vorgelegt von
Andrey Tavleev
aus Moskau/Russland

Tübingen
2025

Gedruckt mit Genehmigung der Mathematisch-Naturwissenschaftlichen Fakultät der Eberhard Karls Universität Tübingen.

Tag der mündlichen Qualifikation:	10.07.2025
Dekan	Prof. Dr. Thilo Stehle
1. Berichterstatter:	Prof. Dr. Klaus Werner
2. Berichterstatter:	Prof. Dr. Beate Stelzer

Zusammenfassung

Superweiche Röntgenquellen (SSSs) stellen eine faszinierende Klasse astrophysikalischer Objekte dar, die sich durch ihre extrem weichen thermischen Röntgenspektren ($<$ 1 keV) auszeichnen, mit Effektivtemperaturen kT, die typischerweise im Bereich von $15-80$ eV liegen, und Leuchtkräften, die sich dem Eddington-Limit ($\sim 10^{36}-10^{38}\,\mathrm{erg\,s^{-1}}$) annähern. Man geht mittlerweile davon aus, dass es sich dabei um akkretierende Weiße Zwerge (WDs) in Doppelsternsystemen handelt, die hohen Massenakkretionsraten unterliegen und dadurch auf ihrer Oberfläche eine quasi-stetige thermonukleare Fusion erfahren. Diese Systeme, die zunächst in den Magellanschen Wolken (LMC und SMC) und später in externen Galaxien sowie in der Milchstraße identifiziert wurden, sind von zentraler Bedeutung für das Verständnis der Entwicklung von Doppelsternsystemen, der Akkretionsphysik und der Vorläufer von Typ Ia Supernovae.

SSSs stellen traditionelle Spektralanalysetechniken vor Herausforderungen. Schwarzkörperapproximationen können ihre komplexe Physik oft nicht adäquat abbilden, da sie dazu neigen, Leuchtkräfte zu überschätzen und Temperaturen zu unterschätzen – bedingt durch eine unzureichende Behandlung der Atmosphärenzusammensetzung und der Strahlungsprozesse. In dieser Dissertation wird eine umfassende theoretische und beobachtungsbasierte Untersuchung durchgeführt, um die Eigenschaften von SSSs mithilfe eines neuartigen Gitters von Modellatmosphären im Zustand lokalen thermodynamischen Gleichgewichts (LTE) für heiße WDs zu erforschen. Diese Modelle erstrecken sich über Effektivtemperaturen von 100 kK bis 1000 kK und berücksichtigen ein Spektrum von Oberflächenschwerebeschleunigungen und chemischen Zusammensetzungen – einschließlich solare, LMC/SMC-ähnliche und solche, die spezifisch für die SSS-Phase klassischer Novae (CNe) sind. Die Modelle werden öffentlich im XSPEC-Format zur Benutzung gestellt, was ein effizientes spektrales Fitting bei gleichzeitiger physikalischer Strenge ermöglicht und eine praktikable Alternative zu rechenintensiven non-LTE (NLTE) Ansätzen darstellt. Die Validierung gegen NLTE-Ergebnisse zeigte nur geringfügige Abweichungen, was ihre Nützlichkeit für die Parameterbestimmung in verschiedenen SSS-Populationen bestätigt.

Das Hauptziel dieser Arbeit besteht darin, Röntgenspektren, die von modernsten Observatorien wie *Chandra*, *XMM-Newton* und *eROSITA* gewonnen wurden, zu interpretieren. Durch die Anwendung dieser Modelle auf klassische SSSs – einschließlich gut untersuchter Quellen wie CAL 83 und RX J0513.9−6951, sowie auf die SSS Phase der klassischen Nova AT 2018bej – werden wesentliche physikalische Parameter wie Effektivtemperatur, Oberflächenschwerebeschleunigung und Elementzusammensetzung abgeleitet und ihre unterschiedlichen Entwicklungspfade aufgezeigt.

Für CAL 83 stimmen die gefundenen Parameter mit früheren NLTE-Ergebnissen überein, was die Anwendbarkeit unserer Modelle zur Analyse von SSS-Spektren unterstreicht. Es wurde zudem bestätigt, dass die Zustände abgeschalteter Röntgenstrahlung dieser Quelle mit dem Erliegen der thermonuklearen Fusion verknüpft sind, wobei die WD-Massenabschätzung dieses Szenario unterstützt.

Für das Objekt RX J0513.9 − 6951, das eine Antikorrelation zwischen optischer und Röntgen-Variabilität aufweist – üblicherweise der Kontraktion und Expansion des WDs zugeschrieben – zeigt die zeitaufgelöste Analyse der Röntgenspektren WD-Parameter, die ein alternatives Szenario begünstigen: Optisch dichte Wolken oberhalb der Akkretionsscheibe modulieren den optischen Fluss durch die Umwandlung variabler Röntgenbestrahlung, was die beobachteten Röntgen-Ein/Aus-Zustände hervorruft.

Für AT 2018bej, eine CN in ihrer SSS-Phase nach dem Ausbruch, wurde über

einen Zeitraum von einem halben Jahr nur eine geringe Entwicklung nachgewiesen, begleitet von einem Rückgang der Kohlenstoffkonzentration. Dieses Ergebnis unterstützt die Schlussfolgerung, dass LTE-Modellatmosphären effektiv zur Analyse der verfügbaren Röntgenspektren von Novae während ihres SSS-Zustands verwendet werden können.

Insgesamt erweitert diese Arbeit unser Verständnis des komplexen Zusammenspiels zwischen Akkretionsprozessen, Kernfusion und Strahlungstransport in SSSs erheblich. Die neuen Modellgitter, die der wissenschaftlichen Gemeinschaft im XSPEC-Format zur Benutzung gestellt werden, ebnen den Weg für zukünftige Beobachtungs- und theoretische Untersuchungen, die darauf abzielen, unser Wissen über WD-Atmosphären und die Physik von Röntgendoppelsternsystemen weiter zu verfeinern.

Abstract

Supersoft X-ray sources (SSSs) represent a fascinating class of astrophysical objects characterised by their extremely soft thermal X-ray spectra ($< 1\,\mathrm{keV}$), with effective temperatures typically ranging from $15 - 80\,\mathrm{eV}$ and luminosities approaching the Eddington limit ($\sim 10^{36} - 10^{38}\,\mathrm{erg\,s^{-1}}$). They are now understood to be the accreting white dwarfs (WDs) in binary systems that undergo high mass accretion rates, leading to quasi-steady thermonuclear burning on their surface. These systems, first identified in the Magellanic Clouds (LMC and SMC) and later in external galaxies and the Milky Way, are important for understanding binary star evolution, accretion physics, and the progenitors of Type Ia supernovae.

SSSs challenge traditional spectral modelling techniques. Blackbody approximations often fail to capture their complex physics, overestimating luminosities and underestimating temperatures due to insufficient treatment of atmospheric composition and radiative processes. In this dissertation, a comprehensive theoretical and observational investigation is carried out to explore the properties of SSSs using a novel grid of Local Thermodynamic Equilibrium (LTE) model atmospheres for hot WDs. These models span effective temperatures from 100 kK to 1000 kK and incorporate a range of surface gravities and chemical compositions – including solar, LMC/SMC-like, and those specific for the SSS stage of Classical Novae (CNe). Publicly released in XSPEC format, the models enable efficient spectral fitting while maintaining physical rigour, offering a practical alternative to computationally intensive Non-LTE (NLTE) approaches. Validation against NLTE results revealed only minor discrepancies, affirming their utility for parameter estimation across diverse SSS populations.

The primary objective is to interpret X-ray spectra obtained from cutting-edge observatories such as *Chandra*, *XMM-Newton*, and *eROSITA*. By applying these models to classical SSSs – including well-studied sources like CAL 83 and RX J0513.9 − 6951, as well as to the SSS phase of the CN AT 2018bej – the work derives key physical parameters such as effective temperature, surface gravity, and elemental abundances, while also unravelling their distinct evolutionary pathways.

For CAL 83, the parameters found agree with previous NLTE estimates, emphasising the applicability of our models for analysing SSS spectra. It was also confirmed that the X-ray off-states of this source are linked to the cessation of thermonuclear burning, and the WD mass estimate supports this scenario.

For RX J0513.9 − 6951, which exhibits anti-correlated optical/X-ray variability typically attributed to the contraction and expansion of the WD, time-resolved analysis of the X-ray spectra reveals WD parameters that favour an alternative scenario: optically thick clouds above the accretion disc modulate the optical flux by reprocessing variable X-ray irradiation, thereby producing the observed X-ray on/off states.

For AT 2018bej, a CN in its post-outburst SSS phase, a minor evolution was traced over a half-year timescale, accompanied by a decrease in the carbon abundance. This result supports the conclusion that LTE model atmospheres can be effectively used to analyse the available X-ray spectra of CNe during their SSS state.

Overall, the work significantly enhances our understanding of the complex interplay between accretion processes, nuclear burning, and radiative transfer in SSSs. The new model grids, made available for community use in XSPEC, pave the way for future observational and theoretical investigations aimed at refining our knowledge of WD atmospheres and the physics of X-ray binaries.

Abbreviations

Astrophysical Terms and Objects

CV	Cataclysmic Variable
WD	White Dwarf
SSS	Supersoft X-ray Source
CN	Classical Nova
RN	Recurrent Nova
NL	Nova-like
DN	Dwarf Nova
IP	Intermediate Polar
LMC	Large Magellanic Cloud
SMC	Small Magellanic Cloud
UV	UltraViolet

Observatories, Instruments, and Missions

CXO	*Chandra* X-ray Observatory
HETGS	High Energy Transmission Grating Spectrometer (on *Chandra*)
LETGS	Low Energy Transmission Grating Spectrometer (on *Chandra*)
HRC	High Resolution Camera (on *Chandra*)
XMM	X-ray Multi-Mirror Mission (*XMM-Newton*)
EPIC	European Photon Imaging Camera (on *XMM-Newton*)
RGS	Reflection Grating Spectrometers (on *XMM-Newton*)
eROSITA	extended ROentgen Survey Imaging Telescope Array
SRG	Spectrum-Roentgen-Gamma spacecraft
eRASS	eROSITA All-Sky Survey
ESA	European Space Agency
INTEGRAL	INTErnational Gamma-Ray Astrophysics Laboratory

ROSAT	ROentgen SATellite

Modelling and Analysis

LTE	Local Thermodynamic Equilibrium
NLTE / non-LTE	Non-Local Thermodynamic Equilibrium
TMAP	Tübingen NLTE Model-Atmosphere Package
BXA	Bayesian X-ray Analysis (software)

Organizations and Funding

DFG	Deutsche ForschungsGemeinschaft (German Research Foundation)

List of original publications

This dissertation is based on the following original journal publications (listed in order of mentioning in the dissertation):

Paper I "Application of hydrostatic local thermodynamic equilibrium atmosphere models to interpretations of supersoft X-ray source spectra"
Suleimanov V., **Tavleev A.**, Doroshenko V., Werner K., 2024, A&A, 688, A39

Paper II "Soft X-ray emission from the classical nova AT 2018bej"
Tavleev A., Ducci L., Suleimanov V., Maitra C., Werner K., Santangelo A., Doroshenko V., 2024, A&A, 689, A335

Paper III "Examining the evolution of the supersoft X-ray source RX J0513.9 − 6951"
Tavleev A., Suleimanov V., Werner K., Santangelo A., 2025, A&A, 694, A73

List of publications not included in the thesis

The following original publications have not been included in the dissertation (listed in reverse chronological order):

1 "Fast giant flares in discs around supermassive black holes"
Lipunova G., **Tavleev A.**, Malanchev K., (2024, under review)

2 "Analysis of accretion disc structure and stability using open code for vertical structure"
Tavleev A., Lipunova G., & Malanchev K., 2023, MNRAS, 524, 3647

3 "Physical modelling of viscous disc evolution around magnetized neutron star. Aql X-1 2013 outburst decay"
Lipunova G., Malanchev K., ... **Tavleev A.**, et al., 2022, MNRAS, 510, 1837

4 "Modelling outbursts of viscous accretion discs"
Lipunova G., Malanchev K., ... **Tavleev A.**, et al., 2022, in Astronomy at the Epoch of Multimessenger Studies, Proceedings of the VAK-2021 conference, p. 288–290

5 "Vertical structure of accretion discs in LMXB"
Tavleev A., Malanchev K., & Lipunova G., 2019, Proceedings of The MultiMessenger Astronomy conference: Gamma-Ray Bursts, Search for Electromagnetic Counterparts to Neutrino Events and Gravitational Waves. p. 229–233

Declaration

I hereby declare that the results and conclusions presented in this dissertation are solely the product of my independent research. The concepts and discoveries detailed herein are entirely original, with proper credit given to collaborators as documented in the respective publications. To the best of my knowledge, no additional sources beyond those referenced in the bibliography and related articles have been used.

Tübingen, April 1, 2025

Andrey Tavleev

Table of Contents

1 Introduction

This dissertation focuses on investigating the properties of Supersoft X-ray Sources (SSSs) through model atmospheres of white dwarfs. This section begins with a concise overview of the history of X-ray astronomy, followed by a discussion of white dwarfs as both isolated objects and in binary systems (Cataclysmic Variables). The nature and characteristics of SSSs, a particular sub-class of these systems, are then explored. The section concludes with a description of the X-ray spectra of these sources and the challenges associated with their modelling.

1.1 A brief history of X-ray astronomy

Since Earth's atmosphere blocks X-rays, the field of X-ray astronomy only emerged with the advent of space exploration. The detection of extraterrestrial X-rays began in the 1950s when instruments aboard rockets measured X-ray emission from the Sun (Chubb et al., 1957). However, it was not until the 1960s that X-ray sources beyond the solar system were identified. The first such discovery was Scorpius X-1 (Sco X-1), detected in 1962 by the group led by Riccardo Giacconi (Giacconi et al., 1962) using an Aerobee rocket.

Significant advancements in X-ray astronomy followed in the 1970s, beginning with the launch of NASA's *Uhuru* telescope in 1970. This mission catalogued over a hundred X-ray sources in the $2 - 6\,\mathrm{keV}$ energy band during its all-sky survey (Giacconi et al., 1972, 1974). A major milestone came with the *Einstein* Observatory, launched in 1978, which was the first large imaging X-ray telescope, with actual X-ray mirrors, enabling high-resolution imaging and location of thousands of X-ray sources (Harris et al., 1990).

Another notable mission was the European X-ray Observatory SATellite (*EXOSAT*, de Korte et al., 1981), operational from May 1983 to April 1986, which studied over 1500 astronomical objects.

The Röntgensatellit (*ROSAT*, Truemper, 1982, Trümper et al., 1991), a collaboration between Germany, the United Kingdom, and the United States, carried an even larger X-ray telescope into space in 1990. This mission identified more than 60 000 sources, significantly improving sensitivity in the soft X-ray band ($0.2 - 2.3\,\mathrm{keV}$) and enabling the detection of many soft/supersoft X-ray sources. The *ROSAT* all-sky survey and its catalogues are still commonly used today.

Subsequent missions – including *Chandra*, *XMM-Newton*, *RXTE*, *BeppoSAX*, *INTEGRAL*, *eROSITA* and others – have explored X-ray emission from a variety of objects, such as stars, white dwarfs, neutron stars, black holes, supernova remnants, active galactic nuclei, and intergalactic gas. These observations have reshaped our understanding of the universe, unveiling a dynamic and energetic cosmos filled with extreme astrophysical phenomena.

1.2 White dwarfs

The white dwarfs (WDs) are the terminal evolutionary state of $\sim 98\%$ of the stars in the Galaxy. A white dwarf (WD) is the final evolutionary stage of low- to intermediate-

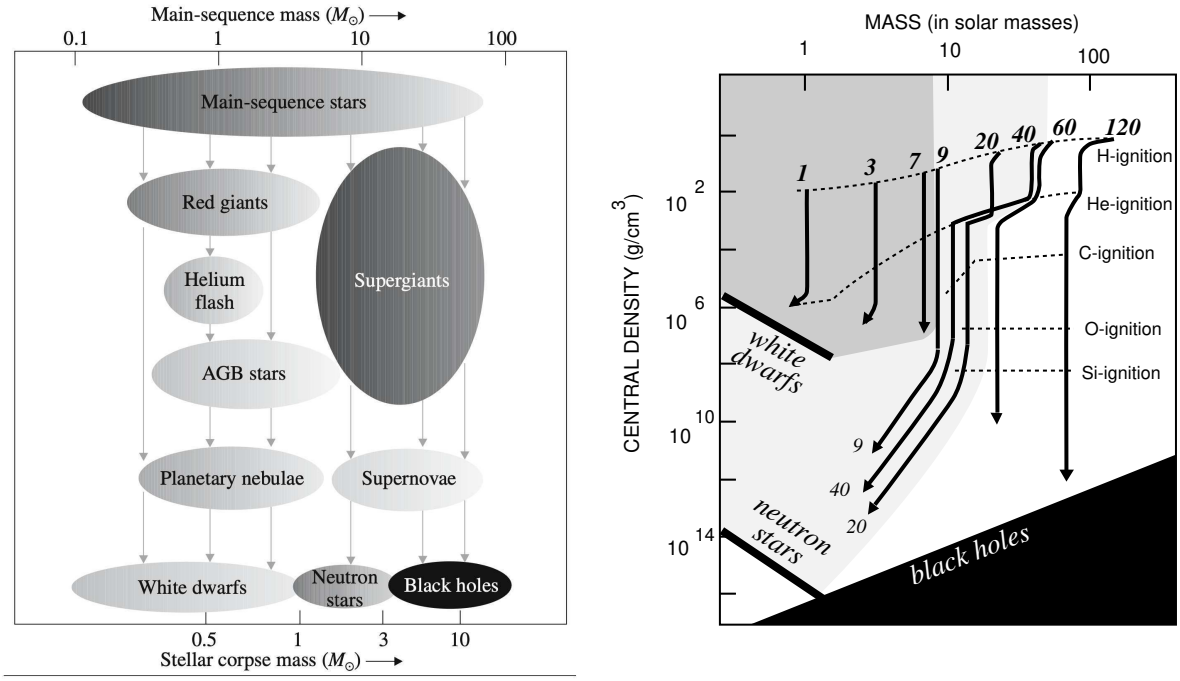

Figure 1: *Left panel:* Evolutionary path of stars with different initial (main sequence) mass. White dwarfs are the endpoints of stellar evolution of $< 8 - 10\,M_\odot$.
Right panel: Stars' evolution towards different end states on the initial mass – central density ($M - \rho$) diagram. Images are taken from Camenzind (2007) and Luminet (1998).

mass stars (up to about $8\,M_\odot$), see right panel of Fig. 1. They have exhausted their nuclear fuel and cannot support themselves against gravitational collapse by means of thermal pressure. Instead they are supported by the pressure of degenerate electrons which describes by the Fermi-Dirac statistics and the Pauli exclusion principle preventing electrons from occupying the same quantum state. This idea was first proposed by Fowler (1926). Actual models of white dwarfs, taking into account the relativistic effects in the degenerate electron equation of state were constructed by Chandrasekhar (1931), who made the fundamental discovery of a maximum mass of a white dwarf – the Chandrasekhar limit, $M_{\rm ch} \approx 1.4\,M_\odot$. Beyond this threshold, degeneracy pressure is insufficient to prevent further collapse, potentially leading to a Type Ia supernova if carbon ignition occurs. The WDs are much smaller than normal stars, with the typical radii of $5000 - 10\,000$ km, corresponding to a mean density of $\sim 10^6$ g cm^{-3}, see left panel of Fig. 1. The temperatures of hot young WDs are $> 10^5$ K, thus they are detected in far-UV (> 6 eV) and soft X-rays ($0.2 - 2.3$ keV). Often they carry strong magnetic fields (up to 100 MG), much stronger than found in normal stars.

Non-accreting isolated WDs undergo a simple cooling evolution along a constant-radius trajectory, with their cooling rate – and thus evolutionary timescale – determined by core mass. In contrast, accreting WDs in cataclysmic variables (CVs) experience heating and spin-up due to mass and angular momentum transfer. Whether non-magnetic (accreting via a disc) or magnetic (accreting via a column or curtain), they undergo thermonuclear burning and explosions. Continuous accretion introduces metal-rich gas, leading to the long-term expansion and contraction of the WD.

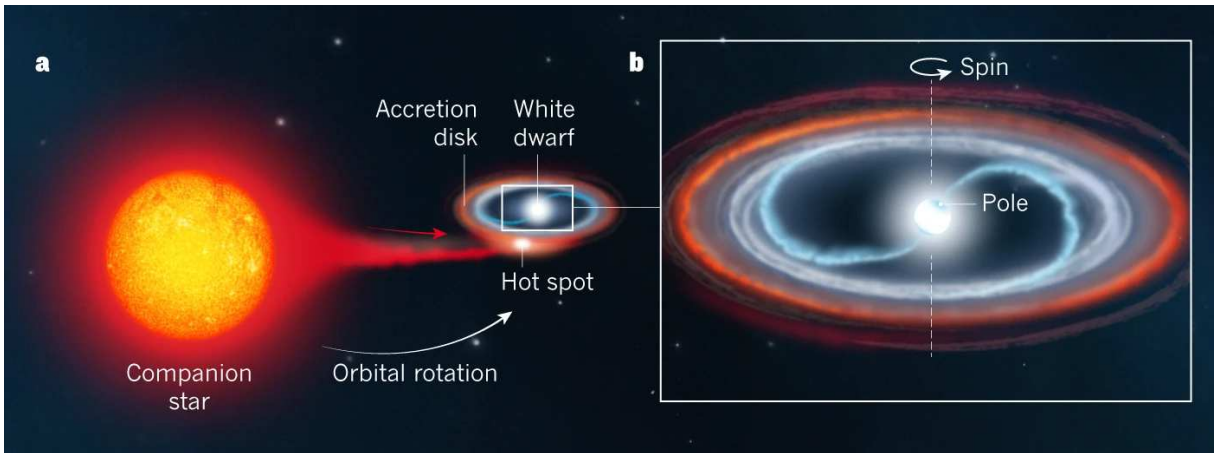

Figure 2: Schematic of a Cataclysmic Variable. Shown is a magnetic CV (Intermediate Polar), where the accretion flow is guided by magnetic field lines near the WD. The image is taken from Shore (2017).

1.3 Cataclysmic variables

Cataclysmic variables (CVs) are stellar binary systems that consist of a WD as a primary. These systems are compact – typically comparable in size to the Sun's radius – with orbital periods ranging from 1.4 to 15 hours, with a few exceptions of up to 3 days. The second component is a normal star (late-type main sequence star or slightly evolved star), which loses material onto the WD by accretion. The companion fills its so-called Roche lobe (Roche lobe overflow) and transfers matter through a L1 Lagrangian point. The non-zero angular momentum of the matter leads to the formation of an accretion disc around the WD unless strong magnetic fields disrupt its formation. The qualitative picture of a cataclysmic variable is presented in Fig. 2.

There are two principal energy sources in a cataclysmic variable: accretion and nuclear fusion. Since the WD is very dense, the gravitational potential energy is enormous, and it is converted into X-rays during the accretion. The efficiency of this process is typically around 0.03%, much lower than the 10% efficiency seen in neutron star or black hole accretion but still sufficient to make CVs significantly brighter in X-rays than typical stellar coronae. Additionally, nuclear fusion can occur on the WD's surface, with hydrogen burning into helium at an efficiency of 0.7%.

CVs can be classified into two main types. Systems where the white dwarf has a weak or negligible magnetic field ($B < 0.01\,\mathrm{MG}$), are known as non-magnetic CVs, which make up the majority of these binaries:

- **Dwarf Novae (DNe)** undergo outbursts, which are reasonably well understood as a release of gravitational energy, caused by a temporary large increase in mass transfer rate through the disc.
- **Nova-likes (NLs)** are the 'non-eruptive' CVs and resemble novae between eruptions. The absence of DN outbursts in NLs is believed to be due to their high mass transfer rates, producing ionised accretion discs in which the disc instability mechanism is suppressed.
- **Classical/Reccurent Novae (CNe/RNe)** and **Supersoft X-ray Sources (SSSs)**, which I will discuss separately below.

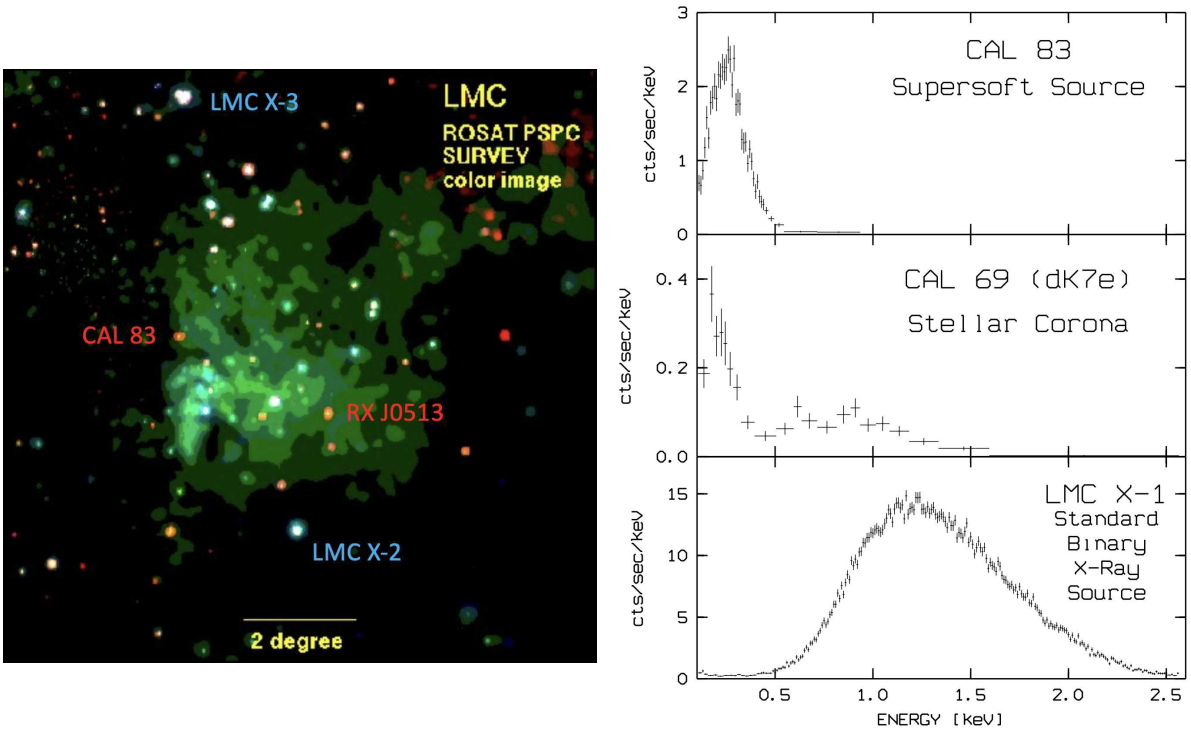

Figure 3: *Left panel:* The *ROSAT* survey of a $13.5° \times 15.5°$ region in the Large Magellanic Cloud. The positions of various X-ray sources, including SSSs CAL 83 and RX J0513.9 − 6951, analysed in this study, are shown.
Right panel: *ROSAT* count spectra of three objects in the Large Magellanic Cloud: the SSS CAL 83, the dK7e foreground star CAL 69, and the black hole candidate LMC X-1. The image was taken from Kahabka and van den Heuvel (1997).

Otherwise, if the WD carries significant magnetic field, such systems are referred to as magnetic CVs:

- **Polars (AM Her systems)**, where the WD magnetic field $B \sim 20 - 320\,\mathrm{MG}$.
- **Intermediate Polars (IPs, DQ Her systems)**, where the WD magnetic field is weaker, $B \sim 1 - 20\,\mathrm{MG}$.

In these systems, the accretion flow is guided by magnetic field lines near the white dwarf, as illustrated in the right panel of Fig. 2.

1.4 Supersoft X-ray sources

The Supersoft X-ray Sources (SSSs) were identified in the Magellanic Clouds by the *Einstein* observatory (Long et al., 1981, Seward and Mitchell, 1981), and they were later classified as a new type of X-ray source during *ROSAT* observations (Trümper et al., 1991). The *ROSAT* spectrum of the prototypical SSS CAL 83 is shown in Fig. 3 alongside a comparison with other X-ray sources. These sources are defined by their extremely soft thermal X-ray spectra, with blackbody temperatures ranging from $15 - 80$ eV ($150 - 900\,\mathrm{kK}$) and high luminosities of $\sim 10^{36} - 10^{38}\,\mathrm{erg\,s^{-1}}$, which are comparable to the Eddington luminosity of a solar mass object (Greiner, 2000, Kahabka and van den Heuvel, 1997). To date, more than 100 SSSs have been identified in approximately 20 external galaxies, the Magellanic Clouds, and our Galaxy (Greiner, 2000, Kahabka, 2006, Maitra and Haberl, 2022).

Their properties align with white dwarfs accreting at a high rate of $\sim 10^{-7}\, M_{\odot}\, \mathrm{yr}^{-1}$, undergoing (quasi-)steady thermonuclear burning on their surface (Rappaport et al., 1994, van den Heuvel et al., 1992). This burning can occur either continuously or in cycles with on/off phases.

1.4.1 The SSS stage of Classical Novae

A classical nova (CN) occurs when accreted material on a WD's surface undergoes unstable thermonuclear fusion. Due to electron degeneracy, the burning process eventually becomes explosive, triggering a thermonuclear runaway (Starrfield et al., 2016). This explosion causes the WD's envelope to expand, dramatically increasing the system's brightness by 8 to 17 magnitudes. The explosion also leads to mass ejection from the binary (see Bode and Evans, 2008, for a review). Eventually, all the types of CVs exhibit the CN explosions.

CNe may undergo the SSS phase during outbursts (Hachisu and Kato, 2006). The portion of the envelope that is not ejected during the outburst may undergo steady hydrogen burning. As the ejected envelope expands and becomes transparent after the outburst peak, the underlying hot nuclear-burning shell – responsible for soft X-ray emission – becomes visible (Bode and Evans, 2008). This scenario is supported by both theoretical models (Soraisam et al., 2016, Starrfield et al., 2004) and observational evidence (see e.g. Henze et al., 2014, Kahabka et al., 1999, Ness et al., 2003, Orio et al., 2001).

SSS systems play a crucial role in evolutionary models, as they are associated with stable burning at high accretion rates and various unstable mass transfer processes. Additionally, due to their high accretion rates and the absence of thermonuclear runaway and mass ejection from the system, the WD mass gradually grows. Given that in these systems $M_{\mathrm{WD}} > M_{\odot}$, it is possible for the WD to reach the upper limit of M_{ch}. Thus, SSSs are considered potential progenitors of Type Ia supernovae (Starrfield et al., 2016).

1.5 Modelling the spectra of SSSs

Interpreting SSS spectra is challenging. While low-resolution spectra can often be approximated by a blackbody fit, this approach lacks physical accuracy. In general, blackbody fitting tends to overestimate the interstellar neutral hydrogen column density N_{H} while underestimating temperature, leading to an overestimated luminosity (see e.g. Greiner et al., 1991, Heise et al., 1994). High-resolution spectra of SSSs are much more complex, exhibiting numerous emission and absorption lines (with the clear role of orientation effects, see Ness et al., 2013).

Theoretical spectra of hot WD atmospheres provide a physically motivated approach to interpreting observed SSS spectra. Heise et al. (1994) developed the first WD atmosphere models to explain SSS X-ray spectra, assuming local thermodynamic equilibrium (LTE). However, at high temperatures, deviations from LTE can be significant. To address this, various authors tried to use to use the model spectra of hot WD atmospheres computed without LTE assumption (non-LTE, NLTE model atmospheres). In particular, the TLUSTY (Hubeny and Lanz, 1995, 2011) has been used to model hot WD atmospheres, with the resulting spectra applied to fitting *BeppoSAX* and *ROSAT* observations of different SSSs (e.g. Hartmann and Heise, 1996, 1997, Hartmann et al., 1999, Parmar et al., 1997, 1998). Lanz et al. (2005) performed a detailed NLTE model atmosphere analysis of *Chandra* and *XMM-Newton* spectroscopy of the SSS CAL 83 in the LMC.

The multi-purpose NLTE model-atmosphere code PHOENIX (Baron et al., 2010, Hauschildt and Baron, 1999), adapted for modelling the late X-ray phase of CNe, was

used to fit the *Chandra* observations of nova V4743 Sgr (Petz et al., 2005). The WD atmosphere was treated as a 1D spherical structure, modelled as expanding but stationary over time. A solar composition was assumed, leading to some uncertainties in the fit.

Given the strong evidence for expansion in the SSS spectra of novae (Ness, 2010), an updated version of PHOENIX was developed to account for this wind-type ejecta expansion (van Rossum and Ness, 2010, van Rossum, 2012). Additionally, a four-dimensional grid of wind-type model spectra was introduced for $T_{\rm eff} = 450 - 750\,{\rm kK}$, 7 values of $\log g$, 4 values of the wind asymptotic velocity v_∞ and 3 values of mass-loss rate $\dot{M}$, while the chemical composition was set to solar (van Rossum, 2012).

The Tübingen NLTE Model-Atmosphere Package (TMAP, Rauch, 2003, Werner et al., 2003, 2012) has been successfully applied to the spectral analysis of hot, compact stars (see Rauch and Werner, 2010, for a brief summary). Using this code, Rauch et al. (2010) performed a NLTE spectral analysis of the nova V4743 Sgr in its SSS phase. Unlike Petz et al. (2005), who used an expanding atmosphere model, this study employed a plane-parallel, static model. However, it incorporated a more realistic chemical composition. A model grid was calculated for H-Ni with solar abundance ratios within $T_{\rm eff} = 450 - 1050\,{\rm kK}$ and a fixed surface gravity of $\log g = 9$ (see refs. in Rauch et al., 2010).

One of the main challenges in modelling SSS spectra, especially in CNe, is the unknown composition of the WD atmosphere, which should reflect both the composition of the accreted material and the products of nucleosynthesis. As a result, a mixture of stellar and CNO-cycle processed material is expected. This leads to a deficiency of hydrogen and an enhancement of helium, as well as a reduction in carbon and an increase in nitrogen and oxygen. These compositional changes influence the strength of absorption lines and the overall shape of the continuum (e.g. Rauch, 2003, Rauch et al., 2010).

Despite these challenges, LTE model atmospheres were employed by Ibragimov et al. (2003) and Suleimanov and Ibragimov (2003) to analyse *ROSAT* spectra of 11 SSSs. They used a modified version of Kurucz's ATLAS code. This models were also applied to fit the spectra of other SSSs (Burwitz et al., 2007, Swartz et al., 2002).

In this dissertation, I present the results of constructing and applying new LTE atmosphere model sets to interpret the *Chandra* and *XMM-Newton* spectra of two classical SSSs CAL 83 and RX J0513.9 − 6951 as well as the *eROSITA* and *XMM-Newton* spectra of the SSS stage of CN AT 2018bej. These findings are detailed in the original Papers I-III. The structure of this dissertation is as follows: Sect. 2 provides an overview of the X-ray observatories whose data have been analysed in this study and in related Papers I-III. Section 3 outlines the method used to compute model atmospheres of hot white dwarfs. A short summary of the original publications is presented in Sect. 4. The main results of this research, along with a brief discussion, are found in Sect. 5, while potential future directions are outlined in Sect. 6. Finally, the original Papers I-III are presented in Appendix A.

2 Observational Facilities and Data Analysis

2.1 X-ray observatories

The energies of X-rays typically range from 0.1 to 100 keV and cannot penetrate the Earth's atmosphere, making it impossible to observe them with ground-based instruments. However, technological advancements in the second half of the 20^{th} century enabled the development of space missions, leading to a significant increase in the number of space-based X-ray telescopes available today. In this section, I briefly describe the characteristics of the X-ray observatories whose data have been analysed in this dissertation and related papers.

2.1.1 *eROSITA*

The extended ROentgen Survey Imaging Telescope Array (*eROSITA*, Predehl et al., 2021), launched aboard the Spectrum-Roentgen-Gamma (Spektra-RG, SRG) spacecraft in July 2019, is designed as a sensitive wide-field X-ray telescope capable of delivering deep, sharp images over very large areas of the sky. Its primary goal is to map the X-ray universe with high sensitivity, providing critical insights into the distribution of dark matter, the growth of supermassive black holes, and the large-scale structure of the universe.

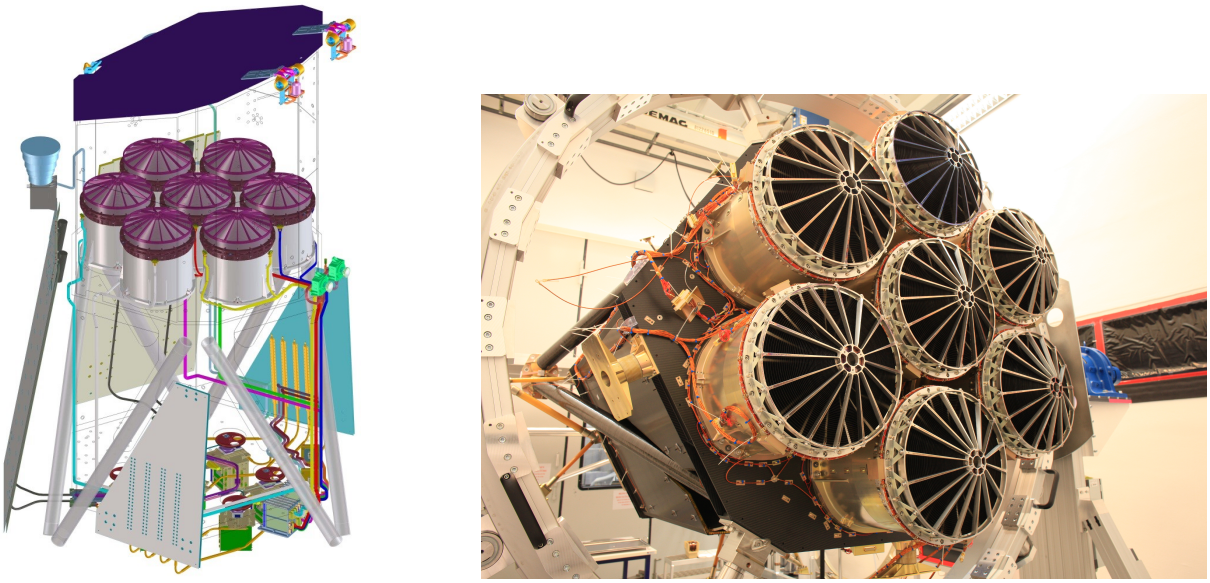

Figure 4: View of the *eROSITA* telescope. *Left panel:* Schematic view with 7 mirror assemblies (MAs: baffle, mirror, electron deflector), and 7 camera assemblies (filter wheel, camera, electronics box). The seven individual telescope modules (TMs) are arranged in a hexagonal shape. *Right panel:* Front view of the telescope with all seven MAs installed. Images are taken from Predehl et al. (2021).

In the soft X-ray band ($0.2-2.3\,\mathrm{keV}$), which we are interested in, the *eROSITA* survey was designed to be about 25 times more sensitive than the previous X-ray all-sky survey conducted by the Roentgen Satellite (*ROSAT*, Truemper, 1982, Trümper et al., 1991). In the hard band ($2.3-8\,\mathrm{keV}$) it provides the first ever true imaging survey of the sky at those energies (Merloni et al., 2024). With soft X-ray effective area and on-axis spatial resolution comparable to *XMM-Newton*, better energy resolution, and a much larger field of view, *eROSITA* is a powerful X-ray telescope.

Each mirror assemble (MA) has a charge-coupled-device (CCD) camera in its focus (see Fig. 4). The *eROSITA* CCDs each have 384×384 pixels in an image area of $28.8\,\mathrm{mm} \times 28.8\,\mathrm{mm}$. The energy resolution of each TM is $\sim 58\,\mathrm{eV}$ at $0.277\,\mathrm{keV}$ and $\sim 65\,\mathrm{eV}$ at $0.525\,\mathrm{keV}$ and the effective area is $\sim 350\,\mathrm{cm}^2$ at $0.28\,\mathrm{keV}$. The timing resolution of *eROSITA* is about 50 seconds, which allows for detailed studies of variability in X-ray sources.

2.1.2 *XMM-Newton*

Operated by the European Space Agency (ESA), the X-ray Multi-Mirror Mission (*XMM-Newton*, Jansen et al., 2001) was launched in December 1999. It is one of the most sensitive X-ray observatories ever built. The spacecraft consists of three X-ray telescopes (see Fig. 5), each comprising 58 mirrors, which provide a large collecting area over a wide energy band from 0.15 to 15 keV.

Each of the telescopes has an European Photon Imaging Camera (EPIC) in its focus. The EPIC system consists of three medium spectral resolution detectors: two Metal Oxide Semiconductor (EPIC-MOS1 and EPIC-MOS2, Turner et al., 2001) and one EPIC-pn (Strüder et al., 2001) CCD-arrays. In addition to the EPIC cameras, *XMM-Newton* is equipped with two Reflection Grating Spectrometers (RGS, den Herder et al., 2001) designed for high-resolution ($E/\Delta E = 100$ to 500) spectroscopy in the $0.3-2.1\,\mathrm{keV}$ range with a maximum effective area of about $140\,\mathrm{cm}^2$ at $0.83\,\mathrm{keV}$. The observatory also includes the Optical Monitor (OM, Mason et al., 2001), an optical/UV telescope with coverage between 170 nm and 650 nm, which enables *XMM-Newton* to perform simultaneous observations in X-ray and UV/optics. All the instruments are shown in Fig. 5, left panel.

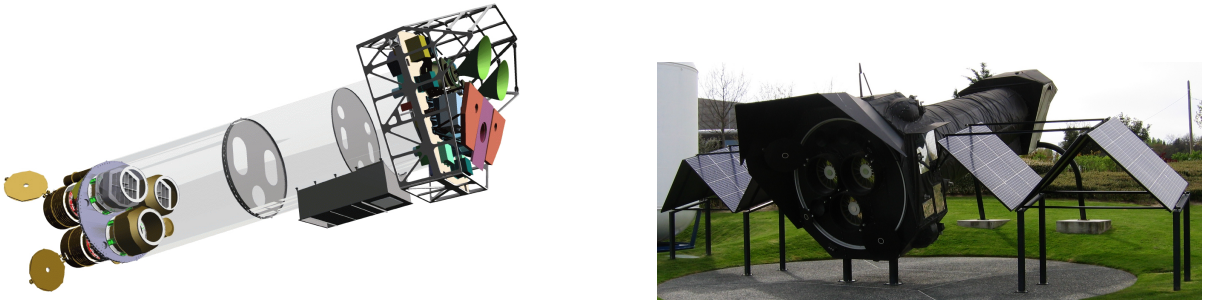

Figure 5: *XMM-Newton* payload and view on. *Left panel:* The mirror modules, two of which are equipped with Reflection Grating Arrays, are visible at the lower left. At the right end of the assembly, the focal X-ray instruments are shown: The EPIC-MOS cameras (green), the EPIC-pn camera (violet) and two RGS detectors (pink). The OM telescope is obscured by the lower mirror module. *Right panel:* Mock-up of *XMM-Newton* at the Cité de l'espace, Toulouse. Credit: Image courtesy of Dornier Satellitensysteme GmbH.

2.1.3 *Chandra*

The *Chandra* X-Ray Observatory (CXO, Weisskopf et al., 2000), the X-ray component of NASA's Great Observatories, was launched on July 23, 1999. Similar to *XMM-Newton*, it has a Wolter-I grazing-incidence X-ray telescope, the High Resolution Mirror Assembly (HRMA, Schwartz et al., 2000), that provides an very high angular resolution of 0.5″ and an effective area of about 800 cm^2 at 0.25 keV.

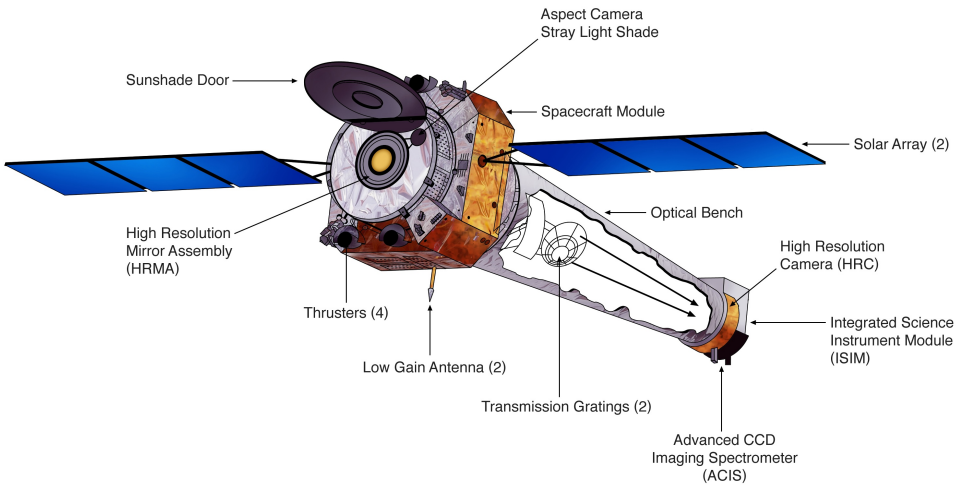

Figure 6: *Chandra* X-ray observatory and its onboard instruments. Credit: NGST & NASA/CXC.

The Integrated Science Instrument Module (ISIM) holds the two focal plane instruments, the Advanced CCD Imaging Spectrometer (ACIS, Garmire et al., 2003) and the High Resolution Camera (HRC Murray et al., 2000). The HRC consists of two independent detectors: HRC-I, designed for imaging, and HRC-S, optimised for spectroscopy. The HRC-I is a single 100 × 100 mm Micro-Channel Plate (MCP), optimised for large field of view imaging (31′) and on-axis angular resolution better than 0.5″. The HRC-S is a set of three 100 × 27 mm MCPs arranged in a strip with a total ∼ 300 × 200 mm active area. This detector is optimised for a grating spectroscopy. Located behind the mirrors are two high resolution spectrometers, the High Energy Transmission Grating Spectrometer (HETGS) and Low Energy Transmission Grating Spectrometer (LETGS). Each spectrometer is activated by swinging an assembly into position behind the mirrors. The LETG gratings are designed to cover an energy range of 0.09 to 3 keV with a spectral resolution of $40 - 2000$, while HETG gratings cover $0.4 - 10$ keV energy range with a resolution of $60 - 1000$. The observatory with all its instruments is shown in Fig. 6.

2.2 X-ray spectral analysis

In X-ray astronomy, the primary data set is an event list, which contains individual photons with their arrival times. Before the main analysis, spectra are extracted from the event lists using the data reduction software specific to each telescope. In the next step, the extracted spectra are analysed using the methods discussed in this section.

The spectrometers' outputs are only the total photons counts (C) in a certain instrument energy channel (I). This observed spectrum is related to the actual spectrum $S(E)$:

$$C(I) = T \int S(E)\, R(I, E) \mathrm{d}E, \tag{2.1}$$

where T is the total exposure time of observation and $R(I, E)$ is the response matrix of the instrument, which is proportional to the probability that a photon with energy E will be detected in channel I. Ideally, to determine the actual spectrum of the source $S(E)$ in units of photon $\mathrm{cm}^{-2}\,\mathrm{s}^{-1}\,\mathrm{keV}^{-1}$, one need to solve the inverse of equation (2.1), which is in general however not possible. Instead, the so-called *forward folding* method is used. In this approach, the appropriate theoretical spectrum is selected and convolved with the instrumental response, providing the predicted count spectrum $C_p(I)$. The parameters of the chosen spectrum are then varied to find the so-called *best-fit values*, which minimise the difference between the observed and predicted data or, more specifically, give the most desirable fit statistic. One of the software packages that provide these procedures and was used in the analysis is XSPEC [1](Arnaud, 1996, Arnaud et al., 1999), which is part of `HEASOFT`.

If the data follow the Gaussian distribution, χ^2-statistic is commonly used. It is defined by

$$\chi^2 = \sum \frac{(C(I) - C_p(I))^2}{(\sigma(I))^2}, \tag{2.2}$$

where $\sigma(I)$ is the uncertainty of channel I. If χ^2 is close enough to the number of degrees of freedom ν, it can be concluded that the best fit is found. To find the uncertainties of the model parameters, we vary the value of the interested parameter until $\Delta\chi^2 = \chi^2(\nu) - \chi^2_{\mathrm{best-fit}}$ reaches a specific value corresponding to the chosen level of confidence. For a 90% confidence level $\Delta\chi^2 = 2.706$.

When dealing with high-count data, the Gaussian distribution provides a good approximation. However, for low-count data (less than $\sim$ 30 counts per energy bin) the assumptions of Gaussian statistics are not valid. One way to address this issue is through data binning, where multiple energy bins are combined to increase the count rate, making the use of χ^2-minimisation valid. However, this approach reduces spectral resolution and detail, making it less suitable for analysing high-resolution spectra.

Instead, the Poisson distribution is used, and the corresponding maximum likelihood-based statistics is known as C-statistics (C-stat, Cash, 1979). However, C-stat lacks a well-defined criterion for accessing the goodness-of-fit, and error estimation based on Δ(C-stat) is not valid. Therefore, an alternative method of finding the best-fit parameters is used, which is known as Bayesian analysis.

2.2.1 Bayesian analysis

Bayesian analysis is a statistical approach that applies Bayes' theorem to update the probability of a model based on prior knowledge and observed data. The Bayesian method estimates the posterior probability distribution of model parameters by combining a prior distribution with the likelihood function:

$$P(\theta|D) = \frac{P(D|\theta)\,P(\theta)}{P(D)} \sim P(D|\theta)\,P(\theta). \tag{2.3}$$

Here $P(\theta|D)$ is the posterior distribution of the model parameters θ, which is unknown and needs to be determined; $P(\theta)$ is the prior distribution of parameters, representing our prior knowledge and assumptions about the parameter space (e.g. the allowed parameter range). $P(D|\theta)$, known as likelihood, describes how well the model explains the observed data. For Poisson data, C-stat is used as a likelihood, we used its XSPEC implementation

[1] https://heasarc.gsfc.nasa.gov/docs/xanadu/xspec/

`cstat`. $P(D)$, the marginal likelihood of evidence, represents basically the prior distribution of the data and does not depend on the model parameters, serving as a normalisation constant.

Unlike the minimisation methods, Bayesian analysis directly yields probability distributions for parameters rather than just point estimates and confidence intervals, allowing for a more robust statistical interpretation of spectral fitting results. The procedure here is to sample the parameter space, which follows the posterior distribution, and then estimate the parameters and their uncertainties from the computed sample. For a given sample, we estimate the best-fit value of parameter as a median of a sample, while the parameter uncertainties are derived from the 0.16 and 0.84 quantiles of the posterior distribution (which corresponds to 68% confidence level).

To sample the parameters distribution we use the Monte Carlo technique called nested sampling. It systematically samples the parameter space by maintaining a set of live points that evolve towards higher likelihood regions, gradually converging on the best-fit solution. This method is particularly effective for models with complex likelihood surfaces, including multimodal distributions or correlated parameters. In particular, the nested sampling algorithms both provide parameter estimation and compute marginal likelihood (evidence), which can be used for model comparison.

We applied the analysis software Bayesian X-ray Analysis (BXA, Buchner et al., 2014, Buchner, 2016a), which connects the nested sampling package UltraNest[2] (Buchner, 2016b, 2021) with XSPEC. Posterior probability distributions and the Bayesian evidence were derived with the nested sampling Monte Carlo algorithm MLFriends (Buchner et al., 2014, Buchner, 2019).

[2] https://johannesbuchner.github.io/UltraNest/

3 Calculation method

This section describes the methods used to compute model atmospheres of hot WDs. We adopt a standard approach for calculating hydrostatic plane-parallel model atmospheres (see e.g. Mihalas, 1978) and utilise a code based on the widely used ATLAS code by Kurucz (1970, 1993). The latter has been modified for high-temperature regimes by Ibragimov et al. (2003).

3.1 Basic assumptions

The structure of plane-parallel, horizontally homogeneous WD atmosphere in hydrostatic and radiative equilibrium is described by a set of differential equations:

- The first one is the hydrostatic equilibrium equation:

$$\frac{\mathrm{d}P_{\mathrm{tot}}}{\mathrm{d}m} = \frac{\mathrm{d}(P_{\mathrm{gas}} + P_{\mathrm{rad}})}{\mathrm{d}m} = g, \tag{3.4}$$

  were $P_{\mathrm{tot}}, P_{\mathrm{gas}}$ and P_{rad} are the total, gas and radiation pressure. The atmosphere is assumed to be thin, so the gravity $g = GM/R^2$ is assumed constant. This surface gravity g (namely $\log g$) is one of the basic parameters of the problem. Instead of the geometrical depth z of the atmosphere, we use the column density

$$\mathrm{d}m = -\rho\,\mathrm{d}z, \tag{3.5}$$

  where ρ is a plasma density. At the surface, $m(z = 0) = 0$. The units of m are $\mathrm{g\,cm^{-2}}$.

- The second equation is the radiation transfer equation for the specific intensity $I_\nu(m, \nu, \mu)$:

$$\mu\,\frac{\mathrm{d}I_\nu}{\mathrm{d}m} = (k_\nu + \sigma_\nu)(I_\nu - S_\nu), \tag{3.6}$$

  where $\mu = \cos\theta$ is the cosine of the angle between surface normal and intensity direction, and k_ν, σ_ν are the absorption and scattering coefficients at frequency ν. The source function S_ν consists of the thermal part and the scattering part:

$$S_\nu = \frac{k_\nu\,B_\nu}{k_\nu + \sigma_\nu} + \frac{\sigma_\nu\,J_\nu}{k_\nu + \sigma_\nu}. \tag{3.7}$$

  Here B_ν is a Planck function, and the scattering part is the mean intensity:

$$B_\nu = \frac{2h\nu^3}{c^2}\,\frac{1}{\exp(h\nu/k_{\mathrm{B}}T) - 1}, \quad J_\nu = \frac{1}{2}\int_{-1}^{+1} I_\nu \mathrm{d}\mu. \tag{3.8}$$

- The third equation is the equitation of radiative equilibrium:

$$\int_0^{+\infty} (k_\nu + \sigma_\nu)(S_\nu - J_\nu)\mathrm{d}\nu = 0 \quad \longrightarrow \quad \int_0^{+\infty} k_\nu B_\nu \mathrm{d}\nu = \int_0^{+\infty} k_\nu J_\nu \mathrm{d}\nu, \tag{3.9}$$

  which states that the total absorbed energy must be equal to the total emitted energy. This equation simplifies to

$$F = 4\pi \int_0^{+\infty} H_\nu \mathrm{d}\nu = \sigma_{\mathrm{SB}}\, T_{\mathrm{eff}}^4, \tag{3.10}$$

  so the total radiative flux F must be conserved. Here σ_{SB} is the Stefan-Boltzmann constant, and the effective temperature T_{eff} is the second basic parameter of the problem.

We assume the equation of state for an ideal gas:

$$P_{\mathrm{gas}} = N_{\mathrm{tot}} k_{\mathrm{B}} T, \tag{3.11}$$

where N_{tot} is the total number density of all particles, T is temperature, and k_{B} is the Boltzmann constant. We took into account the 15 most abundant chemical elements from H to Ni, and the number densities of all ionisation and excitation states of all the ions were computed using the Boltzmann and Saha equations, assuming LTE conditions:

$$\frac{N_{i,j+1}\, N_e}{N_{i,j}} = 2\, \frac{u_{i,j+1}}{u_{i,j}} \left(\frac{h^2}{2\pi m_{\mathrm{e}} k_{\mathrm{B}} T} \right)^{-3/2} \exp\left(-\frac{E_{i,j+1} - E_{i,j}}{k_{\mathrm{B}} T} \right), \tag{3.12}$$

$$\frac{N_i}{N_I} = \frac{g_i}{u_I} \exp\left(\frac{-E_i}{k_{\mathrm{B}} T} \right). \tag{3.13}$$

Here, $N_{i,j}$ and $N_{i,j+1}$ are the number densities of j-th and $(j+1)$-th ionisation states of an atom of element I in the i-th energy state, while N_I and N_i denote the number densities of all atoms of element I and all atoms of element I in the i-th energy state, respectively. The quantity $u_x = \sum g_i \exp(-E_i/k_{\mathrm{B}}T)$ for all i in X is the partition function (statistical sum), where g_i is the degeneracy (statistical weight) of the i-th state. Here, h and m_{e} are the Planck constant and the electron mass, respectively. We considered pressure ionisation and level dissolution effects using the occupation probability formalism (Hummer and Mihalas, 1988), as described by Hubeny et al. (1994).

The radiation pressure and corresponding acceleration is given by the integral:

$$\frac{\mathrm{d}P_{\mathrm{rad}}}{\mathrm{d}m} = g_{\mathrm{rad}} = \frac{4\pi}{c} \int_0^{+\infty} (k_\nu + \sigma_\nu) H_\nu \mathrm{d}\nu, \quad H_\nu = \frac{1}{2} \int_{-1}^{+1} \mu I_\nu \mathrm{d}\mu. \tag{3.14}$$

In general, the initial trial temperature distribution used in the calculation may not yield the correct total flux. Thus, the temperature distribution should be modified to minimise the error:

$$\Delta H = \frac{\sigma_{\mathrm{SB}}\, T_{\mathrm{eff}}^4}{4\pi} - \int_0^{+\infty} H_\nu \mathrm{d}\nu. \tag{3.15}$$

We use the temperature correction scheme from the ATLAS code, and the main changes concern opacities and number densities calculation.

The spectral line list, along with the necessary physical parameters such as gf-values and the energies of the low-energy levels, is taken from the CHIANTI atomic database, Version 3.0 (Dere et al., 1997). The shapes of line absorption opacity are considered as Voigt profiles. Classical damping broadening is applied together with the Tübingen approximation for Stark broadening (Cowley, 1971, Werner et al., 2003). The lines of hydrogen-like ions are considered using Griem's theory of linear Stark broadening (Griem, 1960, 1967).

Formally, the radiation pressure force in spectral lines $g_{\rm rad}$ exceeds the gravity g in the upper atmosphere layers, producing a wind. However, we employed a simple trick, suggested by Ibragimov et al. (2003), to keep the atmosphere in hydrostatic equilibrium. It was assumed that the gas pressure equals 10% of the total pressure, $P_{\rm gas} = 0.1P_{\rm tot} = 0.1gm$, at all depths where $g_{\rm rad} > g$.

The free-free opacities of all ions are calculated under the assumption that the ion's electric field is a Coulomb field of charge Ze corresponding to the ionic charge number Z, with e being the elementary charge. The corresponding Gaunt factors are computed following Sutherland (1998).

To calculate the bound-free opacities from the atomic ground states of all ions, we utilised the procedure presented by Verner et al. (1996). The most significant changes for our present model calculations are associated with the photoionisation opacities from the excited energy levels of heavy element ions. The method for estimating these opacities and the obtained results are presented in the next subsection.

3.2 Photoionisation from excited energy levels

Two different approaches for the photoionisation and free-free opacities from the excited levels can be used to consider excited levels of hydrogen/helium-like ions and of other ions separately. The approach suggested by Karzas and Latter (1961) was used for hydrogen- and helium-like ions. Photoionisation cross-sections from excited levels were computed assuming a Coulomb field of a point-like charge. This approach provides excellent results for hydrogen-like ions. It is not strictly correct for helium-like ions, but the obtained accuracy is sufficient and acceptable for us. We included five excited levels for hydrogen-like ions and ten levels for helium-like ions.

Another approach is used for ions with more than two electrons. The absorption opacities from the excited levels of these ions were computed by the Opacity Project (OP, Seaton et al., 1994) and are available as numerical tables in the TOPBase database[3]. We used these tables for creating simplified analytical fits and implemented these fits in our code. Only a few levels with the lowest excitation energies were considered, typically not exceeding a quarter of the ionisation energy. Although it should be noted that the choice of the levels under consideration was quite arbitrary.

The cross-section for each considered level was fitted using the expression suggested by Kurucz (1970):

$$\sigma(E) = \sigma_{\rm th}\left(A\bar{E}^{p/2} + (1-A)\bar{E}^{1+p/2}\right), \tag{3.16}$$

where $\bar{E} = E_{\rm th}/E$, E is the photon energy, $E_{\rm th}$ is the threshold photoionisation energy from the given level, and $\sigma_{\rm th}$ is the photoionisation cross-section at the photoionisation threshold. The cross-section is a fitting parameter as well as the parameters A and p. The values $E_{\rm th}$ and the obtained fitting parameters $\sigma_{\rm th}$, A and p together with the level statistical weight g for the approximation (3.16) for lower excited levels of C, N, O,

[3] https://cdsweb.u-strasbg.fr/topbase/topbase.html

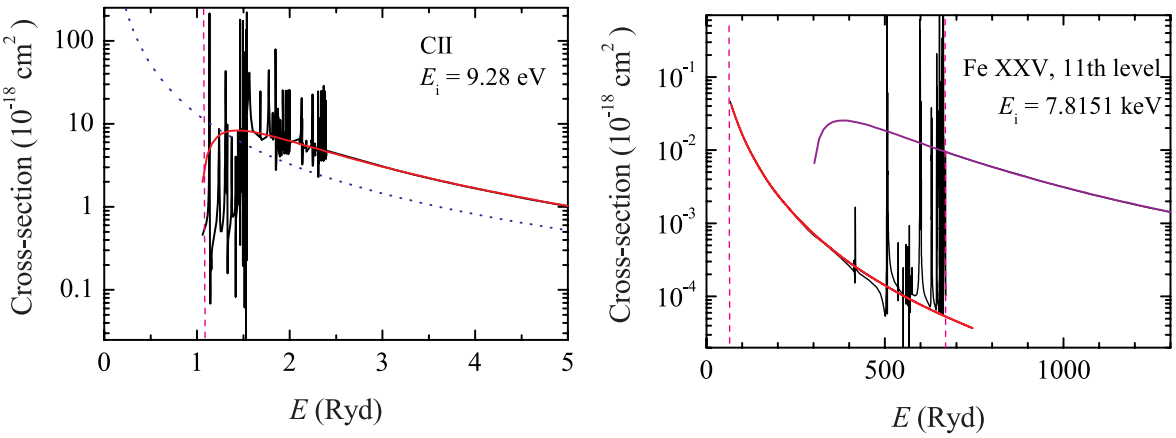

Figure 7: Comparison of the photoionisation cross-sections. for one of the CII excited levels (left panel) and the 11$^{\text{th}}$ excited level of the helium-like ion FeXXV (right panel). Shown are cross-sections computed by OP (solid black curves), the approximation used in ATLAS9 (dashed blue curves), and our fits (red curves). Vertical dashed lines correspond to the ionisation thresholds.

Ne, Na, Mg, Al, Si, S, Ar, Ca, and Fe ions are publicly available[4]. An example of the fitting is shown in Fig. 7, left panel. Note that our smooth fits ignore the auto-ionisation resonances, and OP cross-sections significantly differ from the old ones used in ATLAS9.

The excited levels of the helium-like iron ion have more complicated cross-section dependencies on the photon energy, consisting of two parts. The low-energy one just above the photoionisation threshold is well-fitted with the approach used for other helium-like ions. However, at some energy, approximately ten times larger than the photoionisation threshold energy, the cross-section sharply increases. We considered this second part as an additional photoionisation edge and approximated it using expression (3.16). The comparison of this double fitting with the computed cross-section for one of the excited levels of FeXXV is shown in Fig. 7, right panel.

[4] https://doi.org/10.5281/zenodo.10277303

4 Short summary of the original publications

This section provides a summary of the original research papers that are included in this cumulative dissertation. For each paper, a concise overview of its key contributions and findings will be presented. Additionally, my specific role and contributions to each work will be explicitly outlined, acknowledging that these studies are the result of collaborative efforts among all co-authors. The results and discussion of these works are presented in the next Sect. 5, while full versions of Papers I-III are presented in Appendix A.

4.1 Paper I — Application of hydrostatic local thermodynamic equilibrium atmosphere models to interpretations of supersoft X-ray source spectra

In Paper I, we examined the application of hydrostatic local thermodynamic equilibrium (LTE) atmosphere models to interpret the spectra of supersoft X-ray sources (SSSs). We presented a new grid of hot white dwarf model atmospheres covering effective temperatures $T_{\rm eff}$ from 100 kK to 1000 kK, eight values of surface gravity $\log g$, and three different chemical compositions (solar, LMC-like, and SMC-like).

To demonstrate the utility of these models, we applied them to *Chandra* and *XMM-Newton* X-ray spectra of two classical SSSs: CAL 83 and RX J0513.9−6951. Our analysis yielded estimated effective temperatures of 560 kK (CAL 83) and 630 kK (RX J0513.9 − 6951), with white dwarf masses ranging from 1.1 to 1.4 $M_{\odot}$, consistent with previous estimates. We discussed the reliability of LTE models compared to more complex non-LTE approaches, emphasising that despite their simplifications, LTE models provide a robust approximation for SSS spectrum analysis.

We also explored the positions of the sources on the evolutionary diagrams, concluding that RX J0513.9 − 6951 lies in the stable nuclear burning regime, and its X-ray off-states are most probably connected with the photospheric radius expansion during periods of increased mass-accretion rates. In contrary, the X-ray off-states of CAL 83 are connected with the cessation of thermonuclear burning. Our newly developed model atmosphere set, available in XSPEC format[5], provides a valuable tool for future studies of SSSs and related astrophysical phenomena.

Author's contribution

The author of the dissertation performed the actual model calculations and implemented them into XSPEC. The author also analysed the X-ray spectra and determined all the parameters of the studied sources. The part of the manuscript concerning the spectral analysis and results was written by the author.

[5] https://github.com/HEASARC/xspec_localmodels/tree/master/sss_atm

4.2 Paper II — Soft X-ray emission from the classical nova AT 2018bej

In Paper II we analysed the X-ray emission from the classical nova AT 2018bej, which was detected in its SSS phase by the *eROSITA* telescope in 2020, with follow-up observations by *XMM-Newton*. A grid of LTE model atmosphere spectra was calculated for different values of the effective temperature (from $T_{\rm eff} = 525$ to 700 kK in steps of 25 kK), surface gravity (six values), and chemical composition, assuming approximately equal hydrogen and helium number fractions, and five different values of carbon and nitrogen abundances.

Using this model grid we analysed X-ray spectra from two *eROSITA* survey epochs (eRASS1 and eRASS2) and one *XMM-Newton* spectrum. The analysis estimated the white dwarf's effective temperature at ~ 600 kK and its radius at $8000 - 8700$ km. Comparing data from different epochs, we observed a slight decrease in temperature, an increase in the white dwarf's radius, and a minor drop in carbon abundance. These results suggest ongoing but slowly evolving steady hydrogen burning on the WD's surface. The inferred mass of $1.05 - 1.15\,M_{\odot}$ aligns with theoretical predictions of WDs in the SSS phase.

The study also compared LTE models with non-LTE models available, showing that LTE models can reasonably fit the spectra but may slightly overestimate temperature and underestimate surface gravity. Despite these minor uncertainties, the LTE approach effectively reproduced the observed X-ray emission, demonstrating its utility in modelling classical novae in their SSS state. The findings provide valuable insights into the post-nova evolution of white dwarfs, particularly the role of carbon abundance changes in nova atmospheres. Future long-term observations could further clarify the evolutionary processes in such systems.

Author's contribution

The author made most of the study presented in the paper (models calculating, X-ray spectral analysis) and wrote most of the text. The source's discovery and initial X-ray analysis of the *eROSITA* data was made by Lorenzo Ducci.

4.3 Paper III — Examining the evolution of the supersoft X-ray source RX J0513.9–6951

In Paper III, we investigate the properties of the WD in the supersoft X-ray source RX J0513.9 − 6951 in the Large Magellanic Cloud (LMC), which undergoes periodic transitions between optically bright and faint states that are anti-correlated with its X-ray luminosity. While in Paper I we analysed only a single spectrum of this source to demonstrate the applicability of our models, this study examines eight high-resolution X-ray spectra from *XMM-Newton* and six grating *Chandra* spectra, using the atmosphere models described in Paper I. The primary goal of this research is to test the contraction model, which suggests that changes in the accretion rate cause the WD to expand and contract, leading to variations in its observed emission. The obtained fitting parameters (effective temperature $T_{\rm eff}$, surface gravity $\log g$, and bolometric luminosity L) evolve on the $T_{\rm eff} - \log g$ and $T_{\rm eff} - L$ planes. This evolution follows the model tracks of WDs with masses of $1.05 - 1.15\,M_{\odot}$ and thermonuclear burning on the surface.

However, we show that the photospheric radius and bolometric luminosity of the WD increase when the optical flux decreases, contradicting the contraction model. Instead,

the study proposes an alternative scenario in which X-ray and UV radiation is reprocessed into the optical band due to multiple scattering in the optically thick cloud system above the accretion disc. More significant illumination can lead to rarefying of the cloud slab, thereby reducing the reprocessing efficiency and making the source fainter in the optical band.

Author's contribution

Similar to Paper II, while we used the archived preliminary processed spectra, the author conducted the spectral and theoretical analysis of the data, produced all the figures and tables and wrote most of the text. The alternative evolution model of the source was proposed and described in the Discussion section by Valery Suleimanov.

5 Results and discussion

In this section, I will summarise the methods and key results presented in Papers I–III, with the full journal versions available in Appendix A. The primary focus of this dissertation is to examine the properties of Supersoft X-ray sources using model atmospheres of white dwarfs. The method for computing such atmospheres was briefly introduced in Sect. 3. I will first describe the computed model grids and then present and discuss the results of applying these models to specific X-ray sources.

5.1 Model atmospheres

5.1.1 Computed model grids

The model parameters are the effective temperature $T_{\rm eff}$ and $\Delta \log g = \log g - \log g_{\rm Edd}$, which characterises the distance of the model from the Eddington limit

$$\log g_{\rm Edd} = \log(\sigma_{\rm e}\sigma_{\rm SB}\, T_{\rm eff}^4\, c^{-1}) = 4.818 + 4\, \log(T_{\rm eff}/10^5\,{\rm K}), \tag{5.17}$$

where $\sigma_{\rm SB}$ is the Stefan-Boltzmann constant, c is the speed of light, and $\sigma_{\rm e} = 0.2(1+X) \approx 0.34\,{\rm cm^2\,g^{-1}}$. Here $X \approx 0.7374$ is the hydrogen mass fraction.

We computed three sets of two-parameter plane-parallel hot WD model atmospheres with different chemical compositions. All the sets have the same solar hydrogen/helium mix and different abundances of heavy elements: the solar one ($A = 1$), half the solar abundance ($A = 0.5$), which corresponds to the LMC heavy element abundance, and ten times less than the solar one ($A = 0.1$), which is close to the heavy element abundance in the SMC.

The temperature $T_{\rm eff}$ ranges from 100 to 1000 kK in steps of 25 kK. The parameter $\Delta \log g$ has eight values in the grid: 0.1, 0.2, 0.4, 0.6, 1.0, 1.4, 1.8, and 2.2. Altogether, 296 spectra were computed in every set and implemented as table model[6] for XSPEC.

Figures 8 and 9 present the emergent model spectra for different temperatures, gravity and compositions. Note that Fig. 8 shows the spectra convolved with a Gaussian kernel at a resolution $R = 300$, similar to the *Chandra* resolution, to simulate the observed spectrum of the sources. The spectra are dominated by numerous absorption lines (a region of the CV ground stage is shown in Fig. 9, right panel), and these structures remain visible in the convolved spectra. Additionally, the convolved spectra exhibit emission-like structures, which are, in fact, parts of the spectrum with a small number of absorption lines.

An additional set was computed for analysing the spectra of the SSS stage of nova AT 2018bej. The chemical composition of the WD atmosphere during the SSS phase after the nova explosion is significantly different from that of the accreted matter (see e.g. Rauch et al., 2010) due to thermonuclear fusion products being brought to the surface. Therefore, it is necessary to calculate the model atmospheres with chemical compositions close to the expected one.

It was assumed that the initial chemical composition was LMC-like (solar H/He mix and half-solar heavy elements abundance). Then, some part of the hydrogen was transformed into helium via the CNO-cycle, resulting in an increase in the number fraction

[6] https://github.com/HEASARC/xspec_localmodels/tree/master/sss_atm

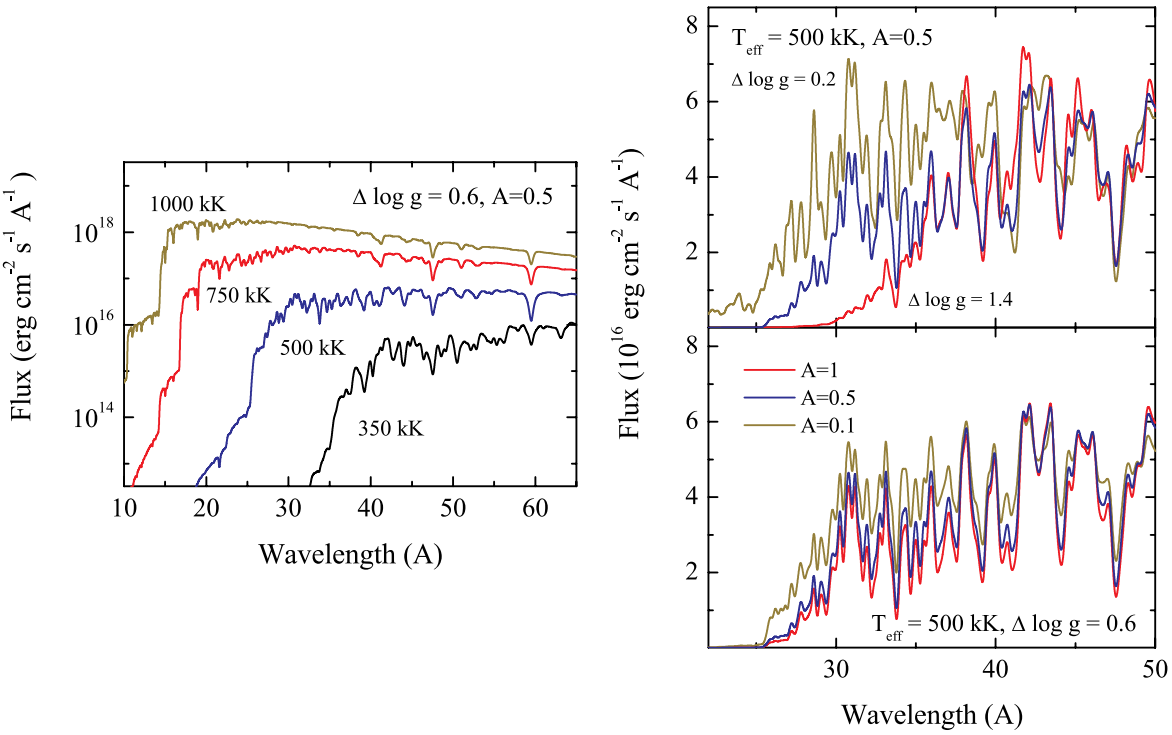

Figure 8: *Left panel:* The model spectra with various $T_{\rm eff}$, fixed $\Delta \log g = 0.6$ and $A = 0.5$. *Right panel:* Comparison of the model spectra ($T_{\rm eff} = 500\,$kK, $\Delta \log g = 0.6$, $A = 0.5$, in blue) with the spectra computed for different $\Delta \log g$ *(top panel)* and A *(bottom panel).*

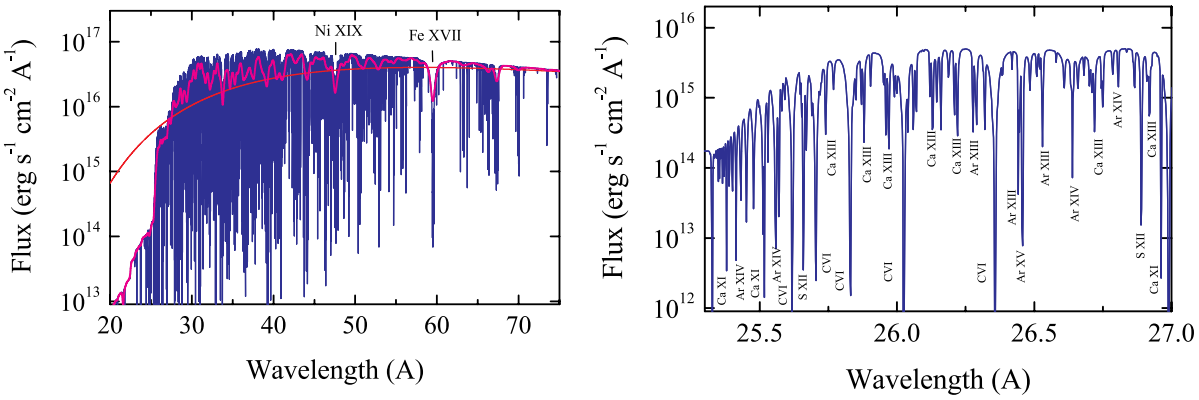

Figure 9: *Left panel:* Model spectrum with $T_{\rm eff} = 500\,{\rm kK}, \Delta \log g = 0.6$ and $A = 0.5$. The Planck function with the same temperature is also shown in red. The convolved spectrum with resolution $R = 300$ is shown in magenta. *Right panel:* Details of the upper spectrum near the CV ground state edge with spectral line identifications.

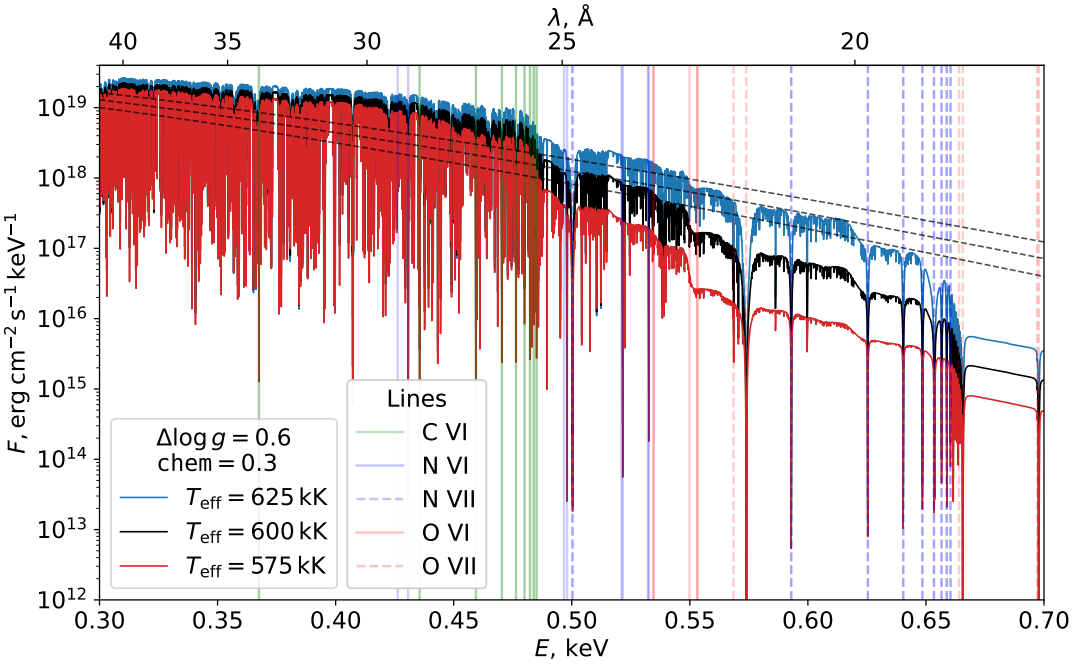

Figure 10: Emergent spectra of `chem`-model atmospheres with different $T_{\rm eff}$ values. The spectral series for some CNO ions are also indicated. The grey dashed lines represent the corresponding blackbody spectra.

of CNO and difference in H/He abundances. We considered various ratios of $A_{\rm H}/A_{\rm He}$ and ultimately adopted 0.46/0.54. The number fraction of carbon was considered as an additional free parameter of the model. Thus, in addition to $T_{\rm eff}$ and $\Delta \log g$, a new parameter has been introduced – the number fraction of carbon '`chem`' in solar units. The number fraction of nitrogen is varied from 1.89 to 0.5 in solar units depending on '`chem`' in assumption that (0.5 − `chem`) of carbon (in solar units) is transformed into nitrogen. Thus, the resulting abundance of carbon '`chem`' changes from 0 (all C→N, $A_{\rm C}/A_{\rm N} = 0/1.89 * {\rm solar}$) to 0.5 (LMC composition, no C→N, $A_{\rm C}/A_{\rm N} = 0.5/0.5 * {\rm solar}$). The abundance of other elements is assumed to be 0.5∗solar (we use solar abundances from Asplund et al. (2009)).

Altogether 288 models were calculated for $T_{\rm eff}$ from 525 kK to 700 kK in steps of 25 kK, $\Delta \log g$ = 0.1, 0.2, 0.4, 0.6, 1.0, 1.4, and `chem` = 0.0, 0.1, 0.2, 0.3, 0.4, 0.5. We refer to this model as the `chem`-model hereafter. The chosen $T_{\rm eff}$ and $\Delta \log g$ ranges were based on a preliminary analysis of the AT 2018bej spectra using a simple blackbody model and the model set described above. All the spectra were implemented as a tabular XSPEC-format model.

Figures 10 and 11 present the model spectra for varying values of $T_{\rm eff}$ and $\Delta \log g$, with `chem` fixed at 0.3. Different absorption edges corresponding to photoionisation from the ground state of CVI (0.49 keV), NVI (0.55 keV), and NVII (0.66 keV) are clearly visible. These features cause significant deviations from the blackbody flux (indicated by dashed-grey lines). The spectra exhibit a dense array of absorption lines, with spectral series of certain CNO ions highlighted. However, the effective temperature primarily determines the overall spectral shape. For better visualisation, the spectra in Fig. 11 have been convolved with a Gaussian kernel with the *XMM-Newton* RGS resolution of $R \approx 650$ in the soft X-ray energy range. The gravity mainly affects the 0.48 − 0.65 keV energy range.

Figure 12 presents the convolved model spectra for different values of the `chem`-parameter. Variations in chemical composition primarily influence the 0.48–0.65 keV energy range. Although these effects are relatively small, the high spectral resolution

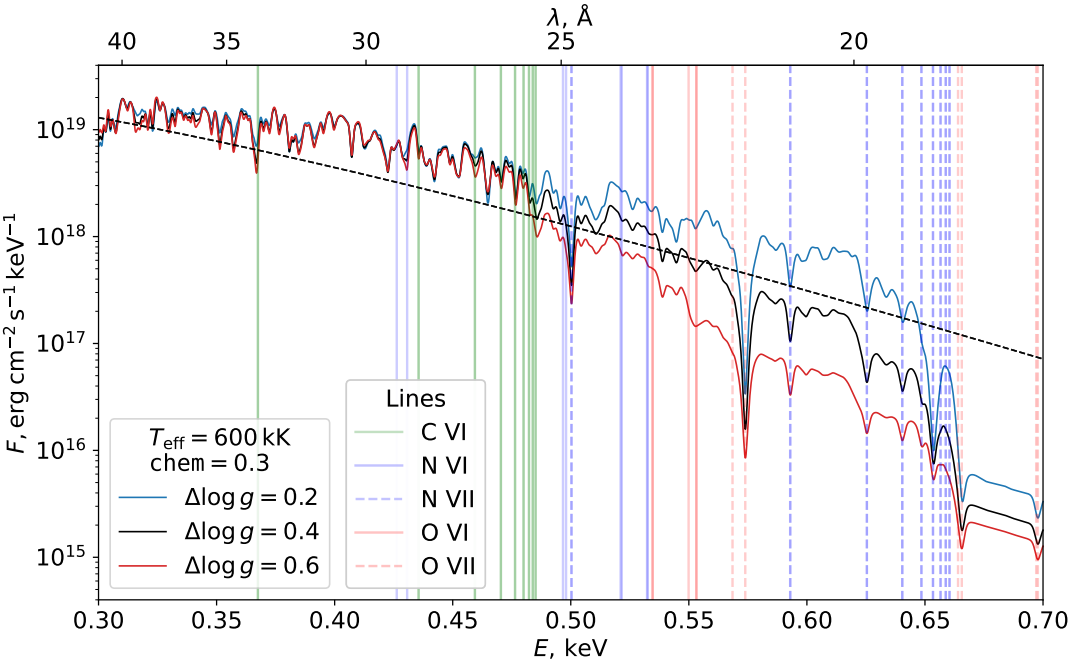

Figure 11: Emergent `chem`-model spectra with various surface gravity (three values of gravity $\Delta \log g$). The spectra are smoothed using a Gaussian kernel with resolution $R \approx 650$. Notations are the same as in Fig. 10.

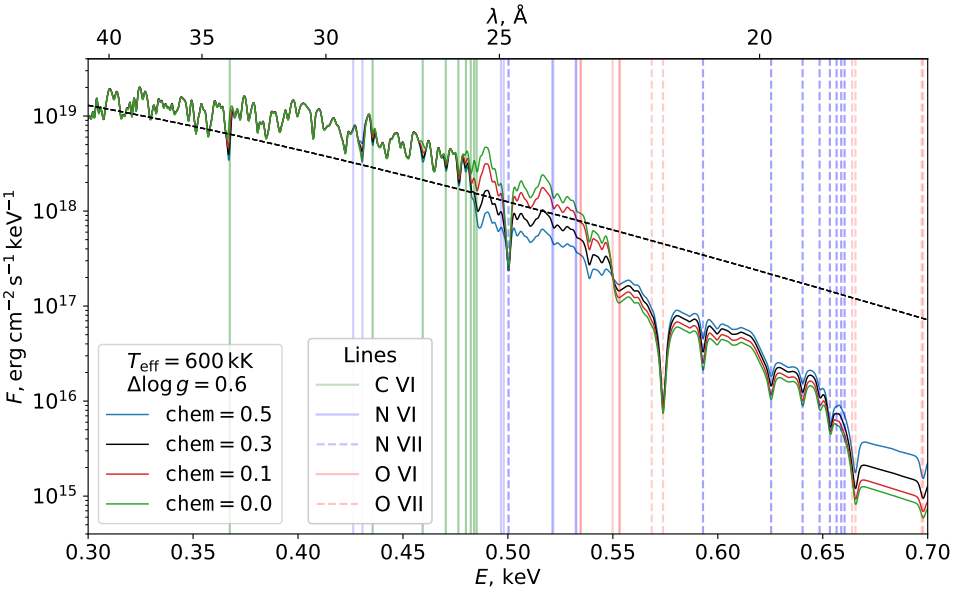

Figure 12: Emergent `chem`-model spectra with different values of the `chem` parameter. The spectra are also smoothed (see Fig. 11). Notations are the same as in Fig. 10.

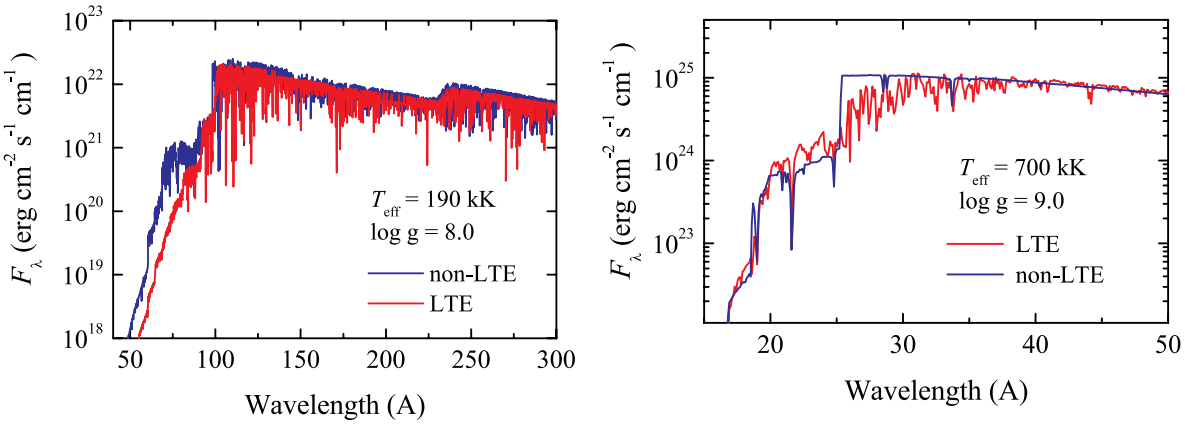

Figure 13: Comparison of the emergent spectra of the model atmospheres computed by our code (red curves), and the TMAP NLTE code (Rauch, 2003, blue curves). All models have solar chemical composition, $T_{\rm eff} = 190\,{\rm kK}$, $\log g = 8.0$ (left panel), and $T_{\rm eff} = 700\,{\rm kK}$, $\log g = 9.0$ (right panel).

of *XMM-Newton* is sufficient to accurately distinguish them.

5.1.2 Comparison with NLTE models

The models from the first three sets were compared with NLTE models by Rauch (2003), as shown in Fig. 13. The left panel presents a comparison with the hottest available NLTE model, which has a solar composition and includes elements from H to Ni[7]. Both spectra were binned with a step size of 0.1Å. The overall spectral shapes are similar, with some differences appearing at shorter wavelengths where the emergent flux is negligible. These discrepancies may arise from NLTE effects and differences in the number of excited levels considered. Additionally, variations in the spectral line lists used in each model lead to differing contributions from individual lines.

The right panel of Fig. 13 shows a comparison with the hottest available NLTE model[8] that has a temperature closer to that of SSSs. However, this model only includes elements from H to Ca, meaning the number of spectral lines considered is clearly insufficient. Despite this limitation, the overall agreement between the spectra remains strong.

Rauch et al. (2010) computed models with a significantly larger number of spectral lines and specific chemical compositions typical of post-nova supersoft phases. Figure 14 compares the emergent spectrum of Rauch's NLTE model 006[9] with our LTE model of the same chemical composition. Both spectra were binned to a 0.002 Å interval within the $10 - 60$ Å wavelength range. The general shapes of the spectra are similar, differences arise in the absorption-edge regions. Due to an over-ionisation of the ions in the NLTE model, absorption jumps appear shallower than in LTE. A sharp jump at 0.45 keV in the NLTE spectrum, linked to ionisation from an excited level of SiXI, is much smoother in our model.

Differences in spectral line lists also lead to variations in line distribution. Additionally, line broadening in H-like ions varies, as shown in the lower left panel of Fig. 14, where NVI and NVII lines are displayed. While radiative damping and Doppler broadening primarily shape resonance line widths, the NVII resonance line in the NLTE spectrum

[7] http://astro.uni-tuebingen.de/~rauch/TMAF/flux_H-Ni.html
[8] http://astro.uni-tuebingen.de/~rauch/TMAF/flux_H-Ca.html
[9] http://astro.uni-tuebingen.de/~rauch/TMAF/flux_HHeCNONeMgSiS_gen.html

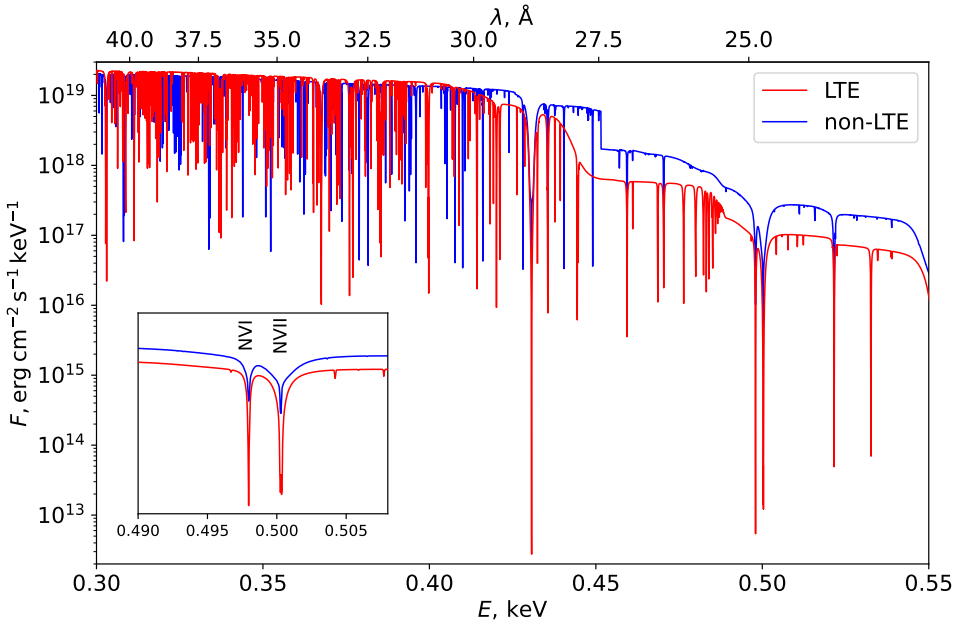

Figure 14: Comparison of the model atmospheres spectra computed by our code (in red) and the TMAP non-LTE code (Rauch et al., 2010, in blue). Both models have $T_{\rm eff} = 600\,{\rm kK}$, $\log g = 9$. The chemical composition corresponds to model 006 from Rauch's grid. The lower left panel shows in detail the comparison of absorption line profiles.

is further influenced by the Stark effect. Differences in level populations also affect line depths – LTE models tend to have cooler upper layers, leading to stronger absorption. This suggests that lower chemical abundances may be required in LTE models compared to NLTE models to reproduce the same observed spectral line absorption.

Finally, we examined the uncertainties that arise from using LTE models instead of NLTE models. It can be shown that an NLTE spectrum with a lower temperature $T_{\rm eff}$ can closely resemble an LTE spectrum with a higher temperature when surface gravity $\log g$ is fixed. Similarly, reducing surface gravity while keeping the temperature constant leads to a comparable effect. As a result, LTE models may overestimate temperature by about 10% and/or underestimate $\log g$ by approximately 0.5 dex, but we note that both effects occur simultaneously.

These discrepancies arise because elements under NLTE conditions are over-ionised compared to the LTE case. Consequently, LTE atmospheres require higher temperatures and/or lower plasma densities to compensate for this effect.

5.2 Application to the Supersoft X-ray Sources

The computed model sets were used to analyse the spectra of three SSSs. in Paper I, we applied these models to study the spectra of two well-knows SSSs: CAL 83 and RX J0513.9 − 6951, though only a single spectrum of the later was examined. Later, in Paper III, we conducted a more detailed analysis of RX J0513.9 − 6951, tracing its evolution and comparing it with existing theoretical models. In Paper II, the `chem-` model set was used to investigate the supersoft post-nova phase of the cataclysmic nova AT 2018bej. In this section I will summarise the main results of these studies, beginning with Papers I and III and concluding with Paper II.

5.2.1 CAL 83

The prototypical SSS CAL 83 was first detected by the *Einstein* observatory in the LMC (Long et al., 1981) and has since been observed by multiple X-ray observatories, including *ROSAT* (Greiner et al., 1991), *BeppoSAX* (Parmar et al., 1998), *XMM-Newton* (Paerels et al., 2001), *Chandra* (Lanz et al., 2005), and *NICER* (Orio et al., 2022). Its X-ray flux is variable, occasionally switching to an off-state (Greiner and Di Stefano, 2002, Kahabka, 1997). X-ray pulsations with a period of about 67 s, likely linked to the WD's spin, were identified by Odendaal et al. (2014). Recently, Stecchini et al. (2023) analysed available *XMM-Newton* spectra of the source.

The optical counterpart is a blue variable star with $V \approx 17$ mag (Cowley et al., 1984), exhibiting prominent Balmer and HeII emission lines (Crampton et al., 1987). A review of its optical and ultraviolet (UV) observations is provided by Skopal (2022), while Gänsicke et al. (1998) estimated an interstellar neutral hydrogen column density of $N_{\rm H} = 6.5 \times 10^{20}\,{\rm cm}^{-2}$.

Model atmospheres of hot WDs have been used to fit the soft X-ray spectra of CAL 83 from various observatories. LTE models by Heise et al. (1994) with fixed $\log g = 9$ yielded a WD's effective temperature $T_{\rm eff} = 510.5^{+73}_{-7}$ kK from *BeppoSAX* data (Parmar et al., 1998). For *ROSAT* observations, Ibragimov et al. (2003) computed LTE models for several $\log g$ values, but the poor energy resolution of *ROSAT* observations prevented constraining surface gravity. The obtained $T_{\rm eff}$ varies from 504 ± 17 kK at $\log g = 8.0$ to 620 ± 25 kK at $\log g = 9.5$, assuming the interstellar column density is fixed at $N_{\rm H} = 6.33 \times 10^{20}\,{\rm cm}^{-2}$.

Non-LTE model atmospheres, computed with the publicly available code TLUSTY (Hubeny, 1988) were applied to grating spectra from *XMM-Newton* (Paerels et al., 2001) and *Chandra* (Lanz et al., 2005). The former provided only rough estimates of $T_{\rm eff} \sim 520$ kK and $\log g \sim 8.5$. However, in the latter study, models were computed specifically for CAL 83, yielding more reliable results (see Table 1).

We simultaneously fitted *Chandra* and *XMM* spectra of CAL 83 using our model grid with LMC composition ($A = 0.5$). Details of the fitting method are provided in Sect. 2.2. In the Bayesian analysis, we set a uniform prior distribution was set for the hydrogen column density $N_{\rm H}$ (in range $(1-10) \times 10^{20}\,{\rm cm}^{-2}$), effective temperature $T_{\rm eff}$ (in range $100 - 1000$ kK), white dwarf mass M (in range $0.3 - 1.4\,M_\odot$) and radius R (in range $(2-20) \times 10^8$ cm). Note that we set the strict upper limit for the WD mass. Additionally, the WD radius must exceed the theoretical limit for a cold WD of the same mass (see e.g. Nauenberg, 1972). Therefore we further used the $M - R$ relation for cold WDs as an additional lower limit for the radius at the given WD mass.

The obtained best-fit parameters are listed in Table 1. The derived absorption column density $N_{\rm H} \sim 5.13 \times 10^{20}\,{\rm cm}^{-2}$ is slightly lower than the fiducial value $(6.5 \pm 1) \times 10^{20}\,{\rm cm}^{-2}$ found previously by Gänsicke et al. (1998). To account for this discrepancy, we performed additional fits with fixed values of $N_{\rm H} = 6.5 \times 10^{20}\,{\rm cm}^{-2}$ and $5.5 \times 10^{20}\,{\rm cm}^{-2}$ (the average column density in the direction of LMC). These results, also presented in Table 1, show that the fit quality decreases, with the WD mass approaching the upper limit.

Figure 15 compares the observed *Chandra* spectrum with the best-fit model with $N_{\rm H}$ as a free parameter. Despite using LTE model atmospheres, the parameters found are very close to those found by Lanz et al. (2005), see Table 1. Thus, our LTE atmosphere models can achieve similar accuracy to NLTE models in describing SSSs. However, our model grid spans a broader parameter space, making it applicable to other sources as well.

We also fitted the *XMM* and *Chandra* spectra with the blackbody model. Allowing $N_{\rm H}$ to vary leads to very large $N_{\rm H}$ values, a non-physically large WD radius, and a lower $T_{\rm eff}$. In this case the derived bolometric luminosity exceeds the Eddington limit for a solar

Table 1: Obtained parameters of SSS CAL 83.

Parameter	CAL 83	CAL 83	CAL 83	CAL 83[a]	CAL 83 (bb)
$N_{\rm H}$, 10^{20} cm^{-2}	6.5[b]	5.5[b]	$5.13\pm^{0.11}_{0.12}$	6.5 ± 1.0	5.13[b]
$T_{\rm eff}$, kK	533 ± 2	556 ± 1	560 ± 2	550 ± 25	$540\pm^{3}_{2}$
$M/M_{\odot}$	1.39 ± 0.01	$1.39\pm^{0.01}_{0.02}$	$1.29\pm^{0.06}_{0.07}$	1.3 ± 0.3	
R[c], 10^8 cm	7.8 ± 0.1	6.3 ± 0.1	6.0 ± 0.1	7.0 ± 0.7	8.6 ± 0.2
L[c], 10^{37} erg s^{-1}	3.5 ± 0.1	2.7 ± 0.1	2.5 ± 0.1	3.5 ± 1.2	4.4 ± 0.2
$\log g$	8.48 ± 0.02	8.66 ± 0.01	8.67 ± 0.03	8.5 ± 0.1	
$\Delta \log g$	0.75 ± 0.02	0.86 ± 0.01	0.86 ± 0.03	≈ 0.7	
`cstat` (dof)[d]	7005.47 (3807)	6823.29 (3807)	6811.52 (3806)		6438.81 (3808)

Notes: (a) – parameters obtained by Lanz et al. (2005); (b) – hydrogen column density $N_{\rm H}$ is fixed; (c) – the distance to the LMC is assumed to be 50 kpc (Pietrzyński et al., 2019); (d) – C-statistics and the number of degrees of freedom for the best fit found using Bayesian analysis.

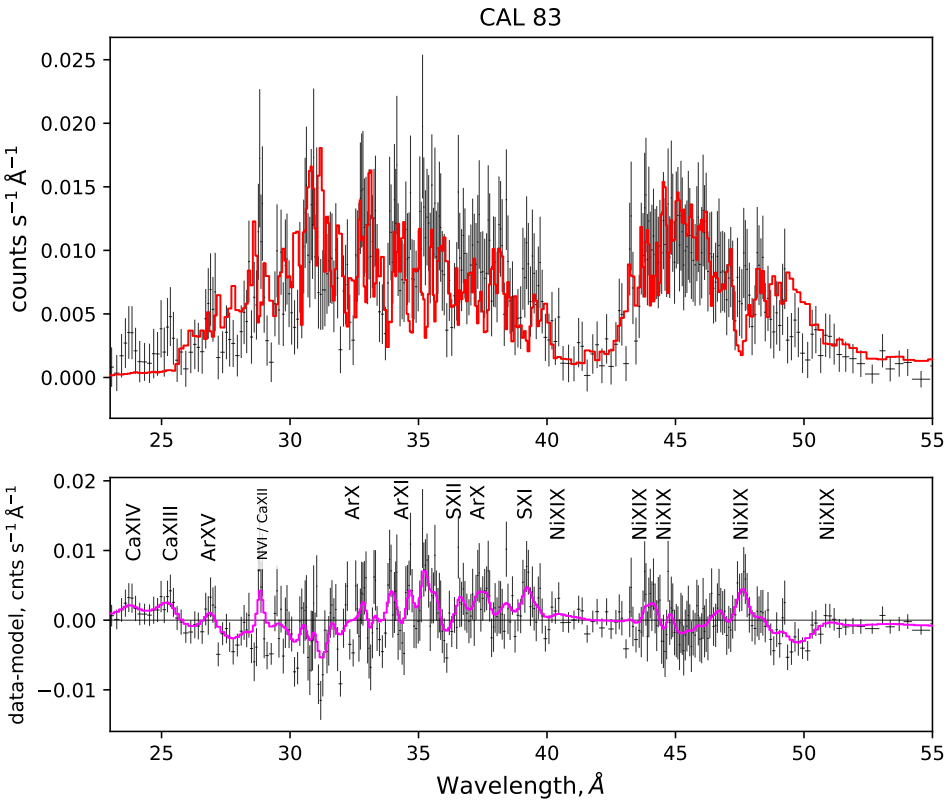

Figure 15: *Upper panel:* Best-fit model of the CAL 83 spectrum. The observed spectrum (*Chandra*, black curve) and the model fit (red curve) are shown. *Lower panel:* Residuals of the fit, along with smoothed residuals (magenta curves). Possible identifications of the most prominent residual features as resonance lines of highly ionised heavy elements are indicated. The best-fit parameters are presented in Table 1.

mass object. However, when $N_{\rm H}$ was fixed to the value obtained from model atmosphere fitting, the blackbody fit produced results comparable to those of the best-fit atmosphere model (see Table 1). Although the blackbody model yielded a slightly better formal fit quality, both models remain statistically acceptable. Notably, atmosphere models provided consistent results without requiring $N_{\rm H}$ to be fixed, unlike the blackbody fits.

The spectra of highly inclined SSSs are known to feature strong emission lines (see e.g. Ness et al., 2013), and similar features likely appear in CAL 83. For example, three emission features between $24 - 28$ Å can be attributed to resonance lines of CaXIV ($\sim$ 24 Å), CaXIII ($\sim$ 25.2 Å), and ArXV ($\sim$ 26.8 Å). Additional flux excesses at longer wavelengths may also correspond to emission lines from highly ionised elements. These features likely originate from line-driven winds off the hot WD surface, impacting spectral fitting accuracy and requiring further modelling.

Residuals from our model fit (Table 1) could reveal the most prominent emission lines (see lower panel in Fig. 15). While incorporating a few $(5 - 6)$ emission lines improves the fit (reduced χ^2 decrease by ~ 0.2), it does not significantly alter the inferred WD atmosphere parameters.

Our spectral fitting showed that the WD mass in CAL 83 is high ($> 1.2\,M_{\odot}$) with a tendency to approach its upper limit. Therefore, for a more reliable mass determination, we compared our results with theoretical models. Several groups have computed WD envelope models with hydrogen thermonuclear burning (see e.g. Nomoto et al., 2007, Wolf et al., 2013). Specifically, Nomoto et al. (2007) calculated $R - T_{\rm eff}$ dependencies for various WD masses with hydrogen-rich envelopes. We converted these into $T_{\rm eff} - \log g$ dependencies, and plotted them with the position of CAL 83, obtained from the fit with free $N_{\rm H}$ (see Fig. 16, left panel). The derived WD mass from these model tracks is lower than our spectral fitting results, about $1.1 - 1.15\,M_{\odot}$.

Another theoretical dependencies were computed by Wolf et al. (2013), shows $\log T_{\rm eff} - \log L/L_{\odot}$ tracks, where L is a luminosity. These tracks are presented in Fig. 16 (right panel) with added position of CAL 83. In this case, the derived mass is lower, $1.05 - 1.1\,M_{\odot}$. Based on these comparisons, we estimate the WD mass in CAL 83 to lie within $1.05 - 1.2\,M_{\odot}$, in marginal agreement with theoretical predictions.

The luminosity of the hot WD in CAL 83 is significantly lower than the predicted value for the steady state burning band. It means that this source lies below the stable thermonuclear burning band, as found earlier (Suleimanov and Ibragimov, 2003). Consequently, thermonuclear burning likely occurs episodically, and the X-ray off-states correspond to the cessation of thermonuclear burning (Kahabka, 1995, 1998). In the latter study, it is proposed that a short (< 100 days) off-states in CAL 83 are possible if the WD is quite massive, $M > 1.2\,M_{\odot}$. Our estimate of the WD mass in CAL 83 supports this condition.

5.2.2 RX J0513.9–6951

The luminous transient soft X-ray source RX J0513.9 − 6951 (hereafter RXJ0513) in the LMC was discovered in the *ROSAT* All-Sky Survey (Cowley et al., 1993, Pakull et al., 1993, Schaeidt et al., 1993). Optical spectra revealed strong emission lines of H, HeII and several higher ionisation emission features with broad wings, suggesting an accretion disc around a WD (Crampton et al., 1996, Southwell et al., 1996). The Massive Compact Halo Objects project (MACHO) survey (Alcock et al., 1996) provided a 3.5 yr light curve of the V $\sim 17^m$ (absolute $M_V \sim -1.5$) optical counterpart of this source, which revealed recurrent low states (dropping by $\sim 1^m$), which last $20 - 40$ days and repeat every $100 - 200$ days. Moreover, these optical low states are accompanied by X-ray

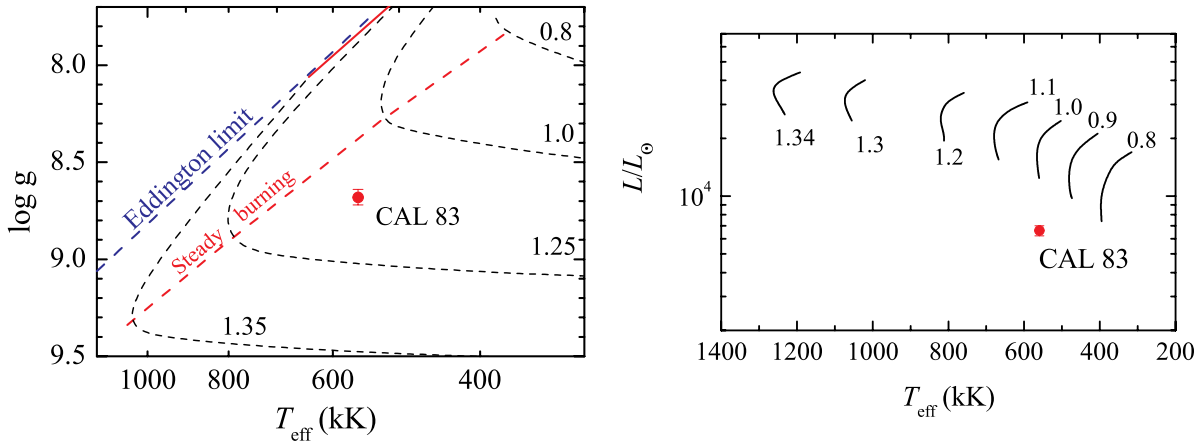

Figure 16: *Left panel:* Position of CAL 83 in the $T_{\rm eff} - \log g$ plane. Model dependencies for various WD masses (Nomoto et al., 2007) are shown by black dashed curves with indicated WD masses (in solar masses). The boundaries of the stable thermonuclear burning band are shown by the solid (upper boundary) and the dashed (lower boundary) red lines. The Eddington limit for solar H/He abundances is shown by the blue dashed line. *Right panel:* Position of CAL 83 in the $T_{\rm eff} - L/L_\odot$ plane. Model dependencies were taken from Wolf et al. (2013). Only the model curves with steady-state thermonuclear burning are shown.

outbursts, so the optical and X-ray states are strictly anti-correlated (Southwell et al., 1996). This variability is explained by the so-called contraction model (e.g. Hachisu and Kato, 2003a,b, Reinsch et al., 1996, 2000, Southwell et al., 1996), which suggests that the observed changes occur due to a change in the mass accretion rate, and therefore, a change in the intensity of thermonuclear burning on the WD surface. High accretion causes WD expansion, shifting radiation out of the X-ray band and making the source faint in X-ray. At the same time the expanded WD effectively illuminates the accretion disc, resulting in high optical flux due to the reprocessing of the WD radiation. This scenario corresponds to the optically bright and X-ray faint state. Conversely, lower accretion leads to WD contraction, enhancing soft X-ray emission. However, reduced accretion disc illumination results in faint optical brightness. The origin of the periodicity in the mass accretion rate changes is not completely clear and may arise from the periodic changes in the accretion disc viscosity (Reinsch et al., 2000), accretion wind (Hachisu and Kato, 2003a,b) or WD irradiation of the companion star (Zhao et al., 2022).

McGowan et al. (2005) confirmed the contraction model by observing RXJ0513 with the *XMM-Newton* telescope to obtain high-resolution spectra of the object and track the X-ray evolution of the WD. However, they interpreted SSS spectra with a blackbody model, which lack physical accuracy. We analysed eight high-resolution XMM (denoted as X1-8) and six *Chandra* spectra (denoted as C0-5) of RXJ0513 using the LTE atmosphere grid with LMC chemical composition. Our goal is to test the contraction model of the source's variability by tracking the evolution of the WD parameters and comparing them with the optical brightness of the source.

For the Bayesian analysis, we set the same prior distributions and parameters constraints ($N_{\rm H}$, $T_{\rm eff}$, M, R) as those used for CAL 83 (see previous Sect. 5.2.1).

We first fitted the spectra with a free absorption parameter $N_{\rm H}$, finding significant variation: $(1-3.5)\times10^{20}\,{\rm cm}^{-2}$ for *XMM-Newton* and $(3.7-5.4)\times10^{20}\,{\rm cm}^{-2}$ for *Chandra*, both lower than the average Galactic value (Doroshenko, 2024). Since fitting parameters strongly depend on $N_{\rm H}$, we adopted $N_{\rm H} = (5.5\pm1)\times10^{20}\,{\rm cm}^{-2}$ from UV analysis (Gänsicke et al., 1998) for consistency.

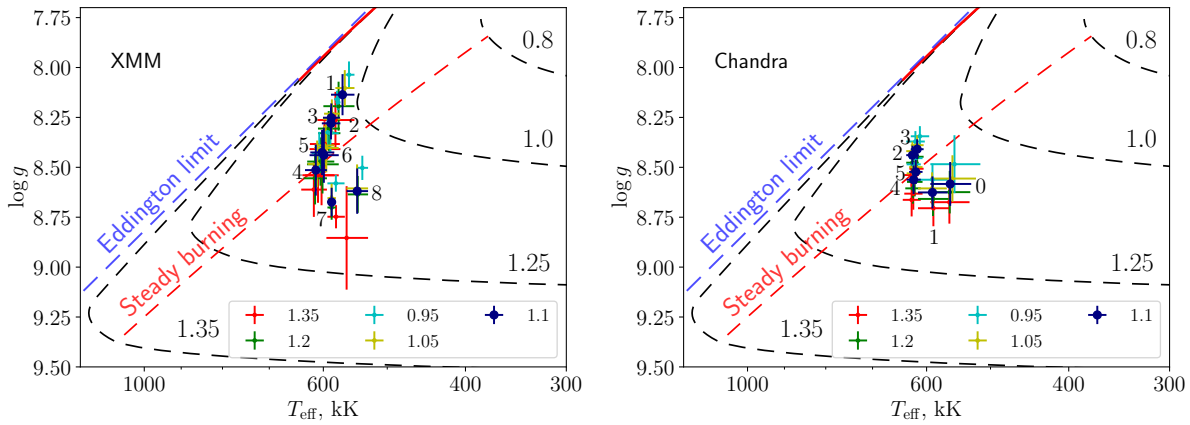

Figure 17: Positions of the source in the $T_{\rm eff} - \log g$ plane according to different *XMM-Newton* (left panel) and *Chandra* (right panel) observations. The WD mass was fixed, and different colours indicate different masses from 0.95 to 1.35 $M_\odot$. For clarity, only a portion of the mass range is shown. The fits with $M = 1.1\,M_\odot$ are additionally indicated by the increased marker size. Model dependencies for various WD masses, taken from (Nomoto et al., 2007), are shown by black dashed curves. The numbers at the curves indicate WD masses (in solar masses). The lower boundary of the stable thermonuclear burning band is shown by the dashed red line. The Eddington limit for solar H/He abundances is shown by the blue dashed line. The numbers denote different spectrum numbers.

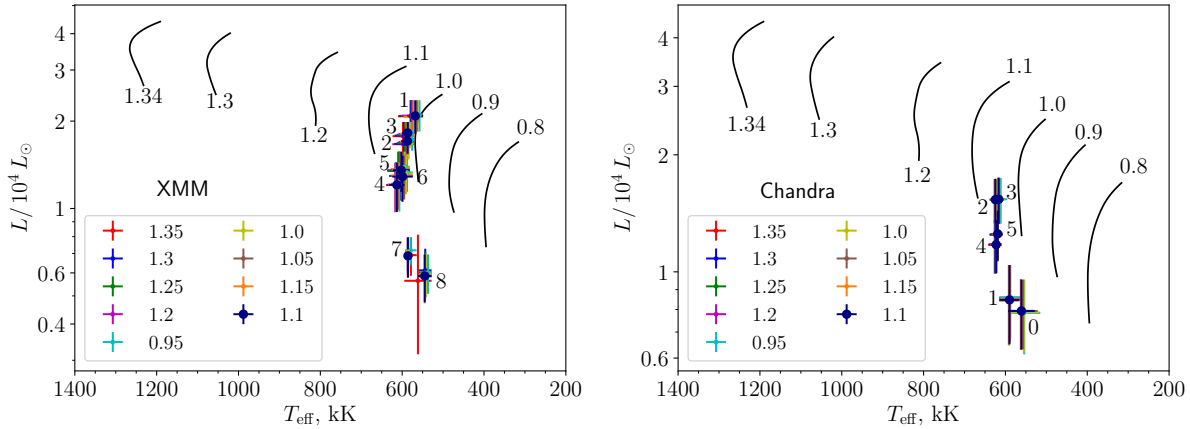

Figure 18: Positions of the source in the $T_{\rm eff} - L$ plane according to different *XMM-Newton* (left panel) and *Chandra* (right panel) observations. The WD mass was fixed, and different colours indicate different masses from 0.95 to 1.35 $M_\odot$. The fits with $M = 1.1\,M_\odot$ are additionally indicated by the increased marker size. Model dependencies were taken from Wolf et al. (2013). Only the model curves with steady-state thermonuclear burning are shown. The numbers denote different spectrum numbers.

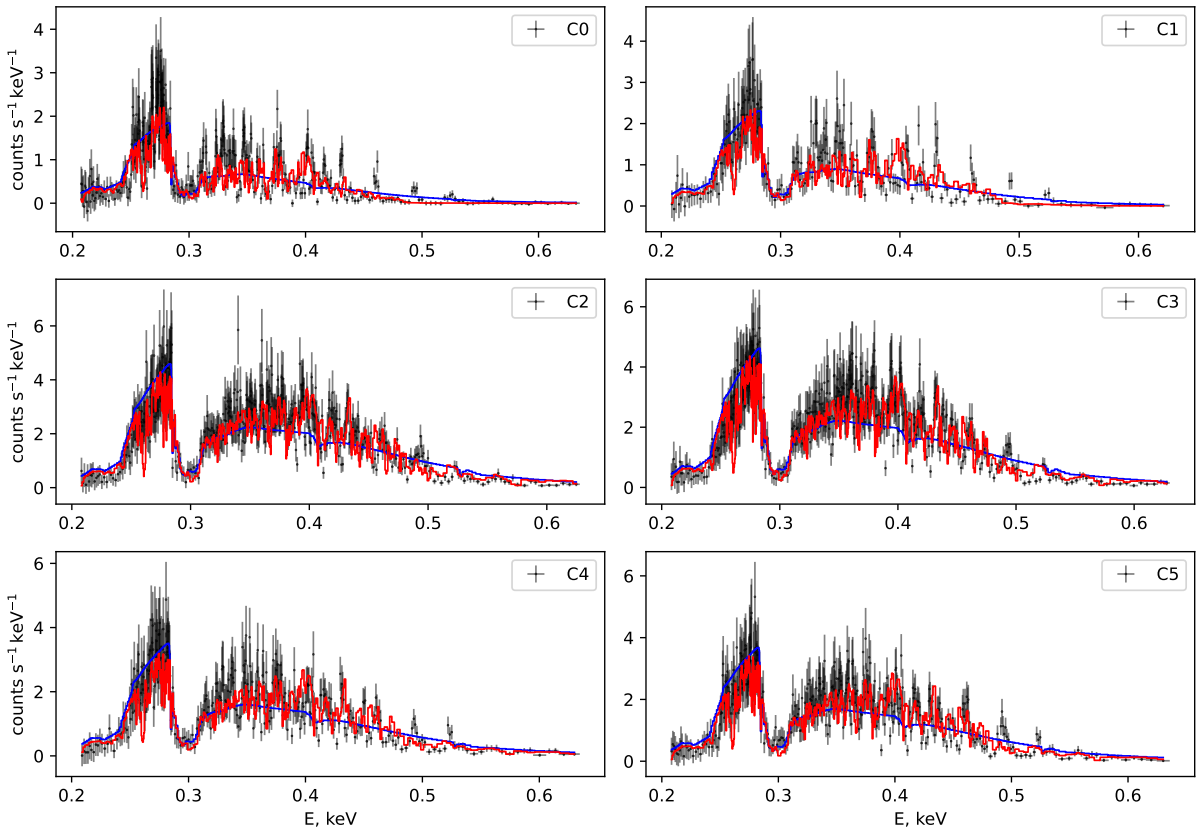

Figure 19: *Chandra* spectra of RXJ0513 with the best-fit LTE models (in red). The absorbed blackbody models are also shown (in blue). The obtained model parameters are listed in Table 2. The hydrogen column density is fixed at $N_{\rm H} = 5.5 \times 10^{20}\,{\rm cm}^{-2}$, and the mass is set at $M = 1.1\,M_{\odot}$.

Similar to the CAL 83 case, the obtained WD mass varies significantly (from 0.8 to $1.38\,M_{\odot}$ for the different observations), if we consider the mass as a free parameter. To estimate the mass more reliably, we compared the derived $\log g$, $T_{\rm eff}$, and bolometric luminosity L for each observation with theoretical models of thermonuclear burning WDs.

We fitted all spectra using nine fixed WD masses from 0.95 to $1.35\,M_{\odot}$ in steps of $0.05\,M_{\odot}$ and compared the results with theoretical $T_{\rm eff} - \log g$ and $T_{\rm eff} - L$ dependencies by Nomoto et al. (2007) and Wolf et al. (2013). As shown in Figs. 17 and 18, the best-fit values correspond to a mass range of $1.0 - 1.15\,M_{\odot}$. Eventually, we adopt $M = 1.1\,M_{\odot}$ as the correct WD mass (with uncertainty about $0.1\,M_{\odot}$), and the parameters corresponding to this WD mass are indicated in Figs. 17 and 18 by an increased marker size.

5.2.2.1 Results and source's evolution

The final results of our analysis are summarised in Tables 2 and 3, while Fig. 19 presents the comparison between observed and model spectra for *Chandra* spectra. Our LTE models yield higher $T_{\rm eff}$ values than those found by McGowan et al. (2005), who used a blackbody model to fit the *XMM* EPIC-PN spectra of RXJ0513. However, the radii obtained are significantly smaller than those from blackbody fits. It should be noted that we fixed the hydrogen column density $N_{\rm H}$ at 5.5×10^{20}, whereas McGowan et al. (2005) used a value of 6.2×10^{20}.

The optical light curve from McGowan et al. (2005) and Burwitz et al. (2008) is

Table 2: Spectral parameters of the LTE and blackbody model fit for the *Chandra* spectra.

	$T_{\rm eff}$ kK	R^a km	$\log g$	L $10^{37}\,{\rm erg\,s^{-1}}$	$T_{\rm eff}^{\rm bb}$ kK	$R_{\rm bb}^a$ km	$L_{\rm bb}$ $10^{37}\,{\rm erg\,s^{-1}}$
C0	561 ± 33	6297 ± 660	8.58 ± 0.11	3.0 ± 0.6	559 ± 24	7776 ± 984	4.3 ± 1.2
C1	590 ± 25	5993 ± 550	8.63 ± 0.08	3.2 ± 0.7	589 ± 24	7159 ± 970	4.4 ± 1.4
C2	625 ± 11	7351 ± 401	8.44 ± 0.05	5.9 ± 0.8	706 ± 18	6121 ± 417	6.7 ± 1.1
C3	616 ± 11	7569 ± 432	8.41 ± 0.05	5.9 ± 0.8	702 ± 25	6191 ± 519	6.8 ± 1.2
C4	623 ± 13	6370 ± 544	8.56 ± 0.07	4.5 ± 0.7	662 ± 17	6322 ± 533	5.5 ± 1.1
C5	619 ± 12	6683 ± 512	8.52 ± 0.06	4.8 ± 0.7	675 ± 23	6114 ± 519	5.7 ± 1.1

Notes: (a) – the distance to the LMC is assumed to be 50 kpc (Pietrzyński et al., 2019); $N_{\rm H} = 5.5 \times 10^{20}\,{\rm cm^{-2}}$ and $M = 1.1\,M_\odot$ are fixed for all of the fits.

Table 3: Spectral parameters of the LTE and blackbody model fit for the *XMM-Newton* spectra.

	$T_{\rm eff}$ kK	R^a km	$\log g$	L $10^{37}\,{\rm erg\,s^{-1}}$	$T_{\rm eff}^{\rm bb}$ kK	$R_{\rm bb}^a$ km	$L_{\rm bb}$ $10^{37}\,{\rm erg\,s^{-1}}$
X1	568 ± 19	10324 ± 1150	8.14 ± 0.10	8.0 ± 1.1	553 ± 16	17765 ± 2227	21.3 ± 3.5
X2	587 ± 16	8775 ± 797	8.28 ± 0.08	6.5 ± 0.6	537 ± 16	18575 ± 2615	20.7 ± 4.0
X3	586 ± 14	9065 ± 727	8.25 ± 0.07	7.0 ± 0.6	553 ± 16	16961 ± 2178	19.4 ± 3.5
X4	613 ± 19	6748 ± 980	8.51 ± 0.13	4.6 ± 0.9	519 ± 8	17984 ± 1512	17.0 ± 2.8
X5	602 ± 21	7417 ± 923	8.43 ± 0.11	5.2 ± 0.8	522 ± 18	18680 ± 3012	18.7 ± 4.3
X6	599 ± 25	7348 ± 1135	8.44 ± 0.14	4.9 ± 0.9	502 ± 19	21202 ± 3744	20.7 ± 5.2
X7	586 ± 7	5562 ± 441	8.67 ± 0.07	2.6 ± 0.4	439 ± 24	27610 ± 8135	20.7 ± 9.0
X8	545 ± 17	6007 ± 685	8.62 ± 0.11	2.2 ± 0.4	413 ± 31	29897 ± 9880	18.7 ± 8.5

Notes: (a) – the distance to the LMC is assumed to be 50 kpc (Pietrzyński et al., 2019); $N_{\rm H} = 5.5 \times 10^{20}\,{\rm cm^{-2}}$ and $M = 1.1\,M_\odot$ are fixed for all of the fits.

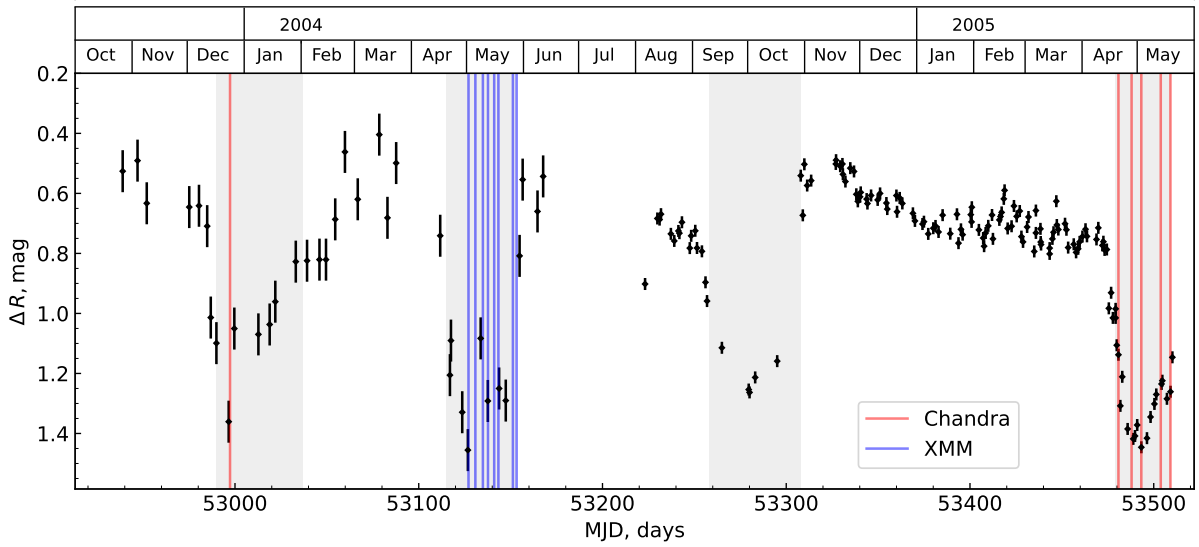

Figure 20: Optical monitoring of RX J0513.9 − 6951, differential magnitudes in the R-filter, obtained by McGowan et al. (2005) and Burwitz et al. (2008). The times of the observed optical low states are shaded in grey. The dates of X-ray *Chandra* and *XMM-Newton* observations are shown in red and blue.

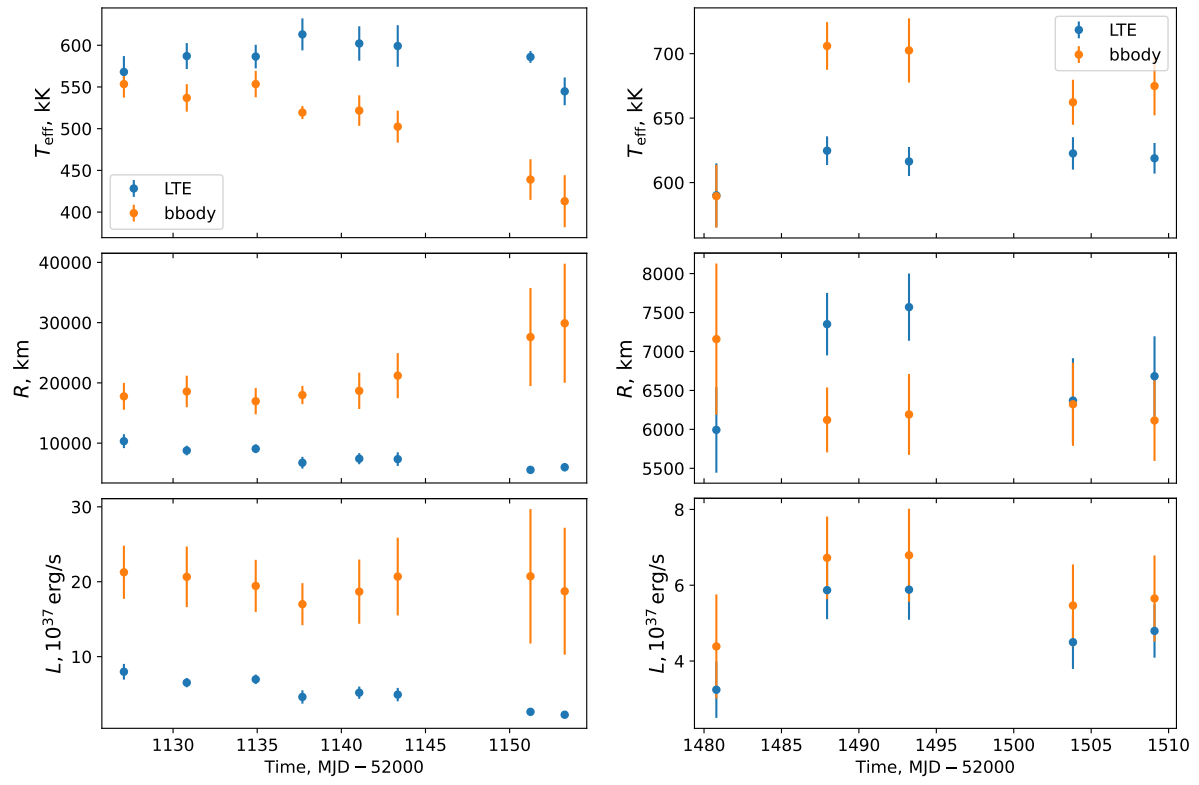

Figure 21: Evolution of temperature, radius, and luminosity of the WD in RXJ0513 over time during the *XMM-Newton* (left panels) and *Chandra* (right panels) observations. Results are shown for both the model atmosphere fit and the blackbody fit. The WD mass is fixed, $M = 1.1\,M_\odot$.

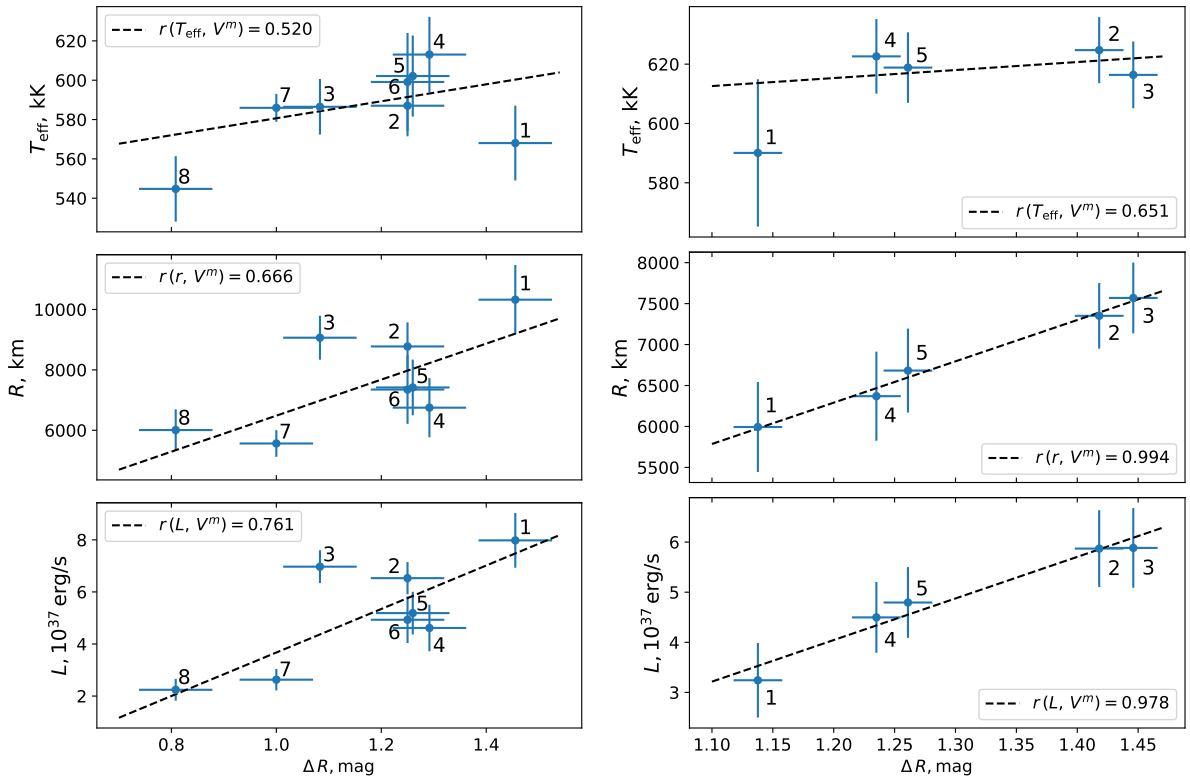

Figure 22: Temperature, radius, and bolometric luminosity of the WD in RXJ0513 versus the optical brightness of the source for the *XMM-Newton* (left panels) and *Chandra* (right panels) spectra. The numbers denote the spectrum number. The linear approximation as well as the Pearson correlation coefficients between the optical flux and WD parameters are also shown.

presented in Fig. 20, with X-ray observation dates marked. The spectra cover three optical low states, corresponding to the C0, X1-8, and C1-5 observational sequences. During X1-6 observations the source remains optically faint, while X7-8 show an increase in optical brightness, marking the transition to the optical high state. Similarly, spectrum C1 signals the start of the optical low state; the source remains optically faint during C2-3, and the transition to the optical high state occurs during C4-5.

Figure 21 shows the evolution of WD parameters over time. In *XMM-Newton* observations, temperature initially rises, while the radius and luminosity decrease. Later, the temperature starts to decrease, then temperature, radius and luminosity all reach minimum values during the transition to the optical high state. In *Chandra* observations, temperature, radius, and luminosity increase during the transition from the high to low optical state. But later, only radius and luminosity decrease when the source brightens optically. The temperature remains stable.

Blackbody fitting results, also in Fig. 21, show that for *Chandra* the parameters align with model atmosphere fits, except the slight overestimates in luminosity. However, for *XMM-Newton* data blackbody fits yield significantly larger radii and luminosities, making them unsuitable for SSS spectral analysis.

Fig. 22 demonstrate a strong correlation (especially in *Chandra* data) between WD radius, bolometric luminosity, and optical brightness – larger WD size and luminosity correspond to lower optical brightness.

Comparing the source's position on the $T_{\rm eff} - \log g$ diagram with theoretical tracks (see Fig. 17) reveals that RXJ0513 lies below the steady-burning strip during its optical high

state (*XMM* X7-8 observations), suggesting the absence of thermonuclear burning and cooling. Conversely, the source undergoes steady burning when it is optically faint. The same trend holds for *Chandra* observations: the source is below the steady-burning strip when optically bright (observations C1, C4 and C5), but shifts above or to its boundary when optically fainter.

Blackbody modelling of *XMM-Newton* spectra (Fig. 21, left panels, in orange) shows a clear $T_{\rm eff}$ drop and radius increase, see also Table 3. However, these results deviate from model atmosphere fits, producing significantly larger radii and luminosities. Blackbody fits for *Chandra* data align more closely with model atmospheres.

5.2.2.2 Discussion

The found correlation between WD photospheric radius and optical brightness in R-band, as well as between the bolometric luminosity and R-band brightness contradicts the predictions of the contraction model. In that model, the opposite correlation between the WD photospheric radius and its optical brightness is expected. It is assumed that a cooler, expanded WD enhances accretion disc illumination, leading to a high optical and low X-ray state, while a hotter, compact WD provides less illumination, causing a low optical and high X-ray state. However, our findings contradict this: RXJ0513's bright optical state corresponds to low X-ray luminosity, placing it below the stable-burning strip in the $T_{\rm eff} - \log g$ plane. We propose an alternative model for the RXJ0513 variability, based on the reprocessing of X-ray emission into optical light in the disc.

The contradiction with the contraction model could be explained if we take into account the effects of thermalisation of hard radiation and its re-emission in the optical part of the spectrum. The disc photosphere itself inefficiently transforms external soft X-ray radiation into the optical band, with a reprocessing efficiency of only $\eta \sim 0.05 - 0.1$, $F_{\rm opt} = \eta\, F_{\rm soft\,X-ray}$ (see e.g. Suleimanov et al., 1999).

However, the efficiency can increase to $\eta \sim 0.3 - 0.5$ if we assume a system of optically thick (in soft X-ray) clouds above the disc. Multiple scattering of soft X-ray and far UV radiation between clouds enhances the total reprocessing efficiency (Suleimanov et al., 2003). Figure 23 illustrates this model. The efficiency η depends on the effective optical depth of the cloud slab (Suleimanov et al., 2003):

$$\tau_{\rm eff} \approx \pi\, R_{\rm cl}^2\, N_{\rm cl}\, L, \tag{5.18}$$

where $R_{\rm cl}$ is the cloud size, $N_{\rm cl}$ is the cloud number density, and L is the geometrical thickness of the cloud slab. The reprocessing efficiency reaches the maximum at $\tau_{\rm eff} \approx 1 - 10$.

In our proposed model, soft X-ray flux illuminating the accretion disc is efficiently converted into optical/UV emission by multiple scatterings within optically thick (in the soft X-ray band) clouds embedded in a disc wind or corona. These clouds may form due to thermal instability in the matter above the disc, irradiated by far UV/soft X-ray flux (see e.g. Jimenez-Garate et al., 2002).

When the WD has lower luminosity and a smaller radius – similar to a cold WD – the cloud system is dense enough to achieve high reprocessing efficiency, leading to a low X-ray, but high optical state. Conversely, when the WD is more luminous with an expanded photosphere, the cloud slab becomes rarefied, reducing reprocessing and resulting in a high X-ray, but low optical state. Figure 23 illustrates these two states.

This proposed toy model qualitatively explains the observed properties of RXJ0513 and may open a window for observational investigations of thermal instability in plasma irradiated by hard UV/soft X-ray flux.

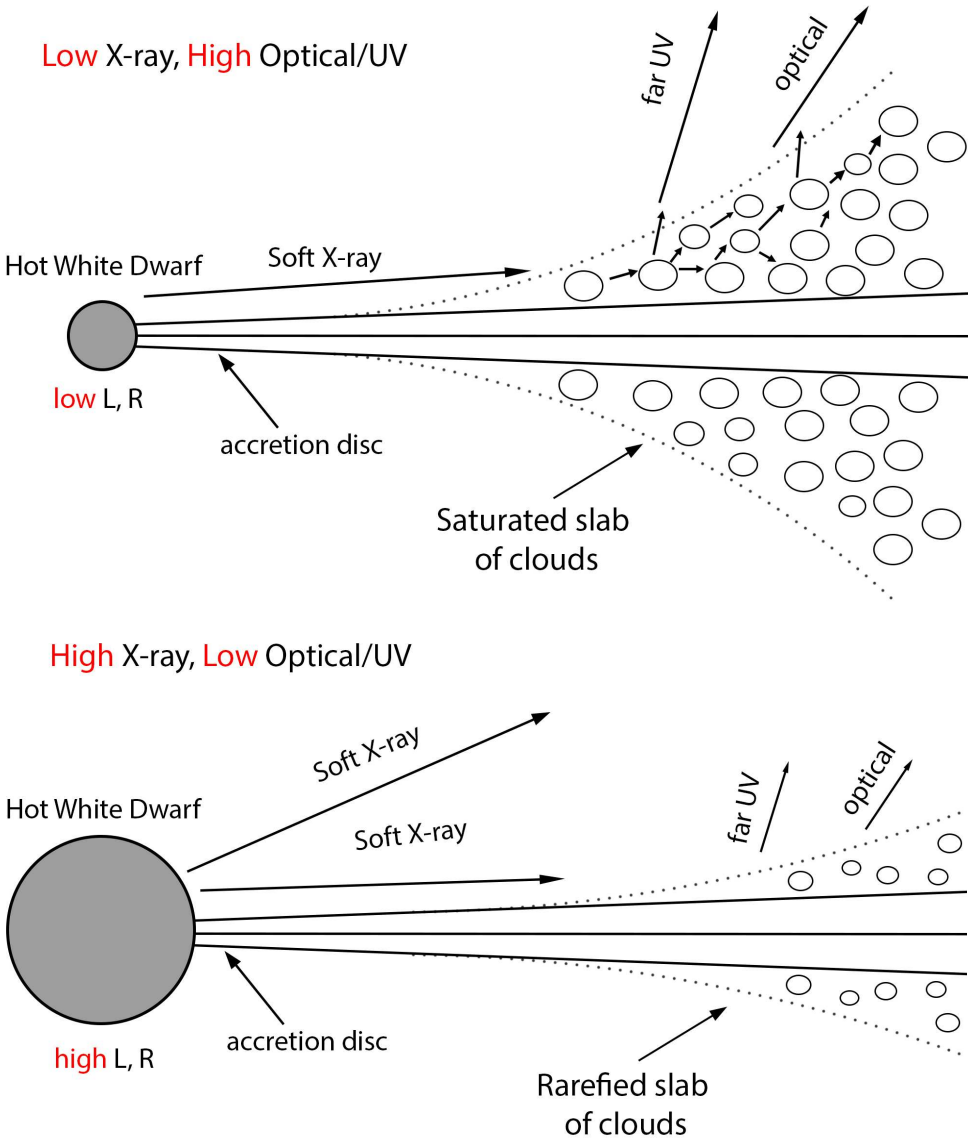

Figure 23: Qualitative picture of the proposed high and low optical states for RXJ0513. Shown are the WD, the accretion disc, and blobs or clouds above the disc. Upper panel – high optical state; the low luminous WD is compact, and its X-ray emission is effectively reprocessed into optical light due to multiple scattering between clouds. Lower panel – low optical state; the luminous WD with an expanded photosphere evaporates most of clouds decreasing the reprocessing efficiency and reducing the optical flux.

5.2.3 AT 2018bej

This X-ray source was discovered in 2020 by *eROSITA* during the first part of its eRASS all-sky survey. Its position is consistent with the known classical nova (CN) AT 2018bej/ASAS-SN 18jj in the LMC (Chomiuk et al., 2018, Ducci et al., 2020). The thermal X-ray spectrum, with low temperature of ∼30 eV (∼350 kK) and high luminosity $> 10^{37}$ erg s^{-1}, indicated that the supersoft source (SSS) phase of CNe was observed for this nova (Ducci et al., 2020). The source was later observed during eRASS2–eRASS4 surveys in 2020 and 2021, but it was barely visible in eRASS3, and undetectable in eRASS4, so we do not analyse these data. Following the *eROSITA* discovery, a high-resolution spectral observation was conducted by *XMM-Newton* Reflection Grating Spectrometer (RGS) instrument on 2020 March 14, 10 days after the last eRASS1 observation.

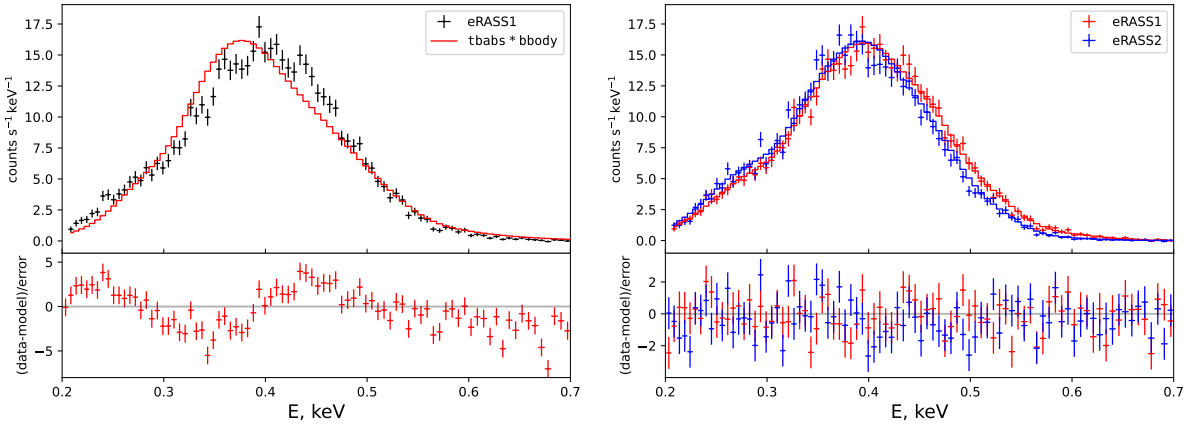

Figure 24: *eROSITA* spectra of AT 2018bej. *Left panel:* The eRASS1 spectrum. Also shown is the absorbed blackbody model. The obtained blackbody parameters are presented in Table 4. *Right panel:* Model atmosphere best-fit of the eRASS1 (in red) and eRASS2 (in blue) spectra. The obtained parameters are presented in Table 5.

Table 4: Preliminary fit of AT 2018bej with a blackbody model.

	eRASS1	XMM
$N_{\rm H}$, 10^{20} cm^{-2}	14.2 ± 0.5	23.3 ± 0.3
$T_{\rm eff}$, kK	423 ± 8	346 ± 2
R^a, 10^8cm	$103 \pm^{15}_{13}$	~ 600
L, 10^{37} erg s^{-1}	$240 \pm^{70}_{60}$	3700 ± 100
`cstat` (dof)	412.90 (128)	5481.75 (3325)

Notes: (a) – the distance to the LMC is assumed to be 50 kpc (Pietrzyński et al., 2019).

Initially, the *eROSITA* and RGS spectra were fitted using a simple blackbody model. The left panel of Fig. 24 shows the blackbody fit of the *eROSITA* spectrum. However, these results are considered non-physical, as the emitting radii of $(1-6)\cdot10^5$ km (assuming a LMC distance of 50 kpc, see Table 4) are inconsistent with typical WD radii. Moreover the resulting luminosity exceeds the Eddington limit for typical WD masses. This is not surprising, as it is well known that blackbody fits tend to overestimate $N_{\rm H}$ and

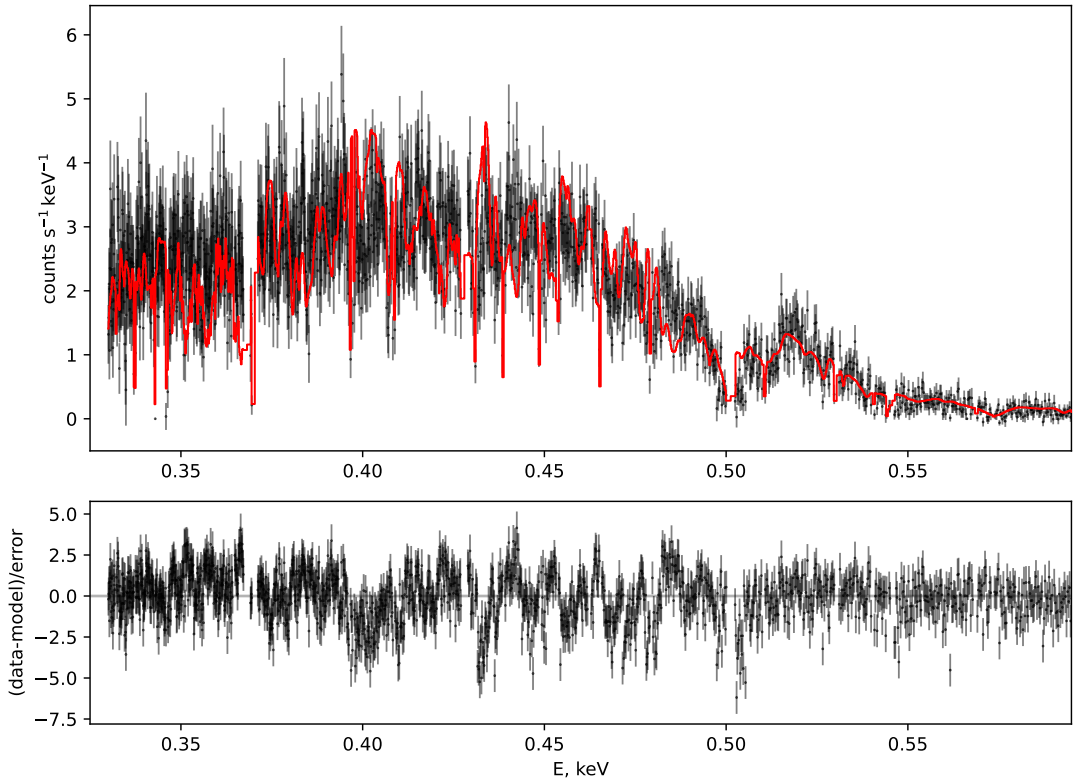

Figure 25: The *XMM-Newton* RGS spectrum together with best-fit LTE model. Shown is spectrum of RGS 1 instrument. The best-fit parameters can be found in Table 5. The hydrogen column density is fixed at $N_{\rm H} = 5.74 \times 10^{20}\,{\rm cm}^{-2}$.

underestimate the temperature (see e.g. Greiner et al., 1991, Heise et al., 1994). Therefore hot WD model atmosphere spectra are required to accurately describe SSS spectra.

We fitted the eRASS1, eRASS2, and *XMM-Newton* spectra with our `chem`-model (see Sect. 5.1.1). For the Bayesian analysis, we set a uniform prior distribution for $N_{\rm H}$ (in the range $(1-10)\times10^{20}\,{\rm cm}^{-2}$), '`chem`' parameter (in the range $0-0.5$), effective temperature $T_{\rm eff}$ (in the range $525-700\,{\rm kK}$), WD mass M (in range $0.3-1.4\,M_\odot$) and radius R (in range $(2-20)\times10^3\,{\rm km}$). Again, a strict upper limit of $M = 1.4\,M_\odot$ for mass was set, as well as the lower limit for radius based on the theoretical limit for a cold WD of the same mass (see e.g. Nauenberg, 1972).

Table 5 summarises our results, while Fig. 24 shows the comparison between the observed and model *eROSITA* spectrum. The parameters' posterior distributions for all spectra are narrow enough and have only one mode, resulting in smaller errors, though the WD mass tends to its upper limit, particularly for the *XMM-Newton* case.

Table 5: Spectral parameters of the LTE model fit for AT 2018bej.

	eRASS1	eRASS2	XMM	XMM[a]	eRASS1[d]	eRASS2[d]
$N_{\rm H}$, $10^{20}\,{\rm cm}^{-2}$	$5.88\pm^{0.17}_{0.16}$	5.69 ± 0.15	$3.06\pm^{0.12}_{0.13}$	5.88^{a}	$5.83\pm^{0.14}_{0.16}$	
$T_{\rm eff}$, kK	$597\pm^{4}_{9}$	$541\pm^{10}_{14}$	631 ± 1	604 ± 1	$578\pm^{14}_{11}$	$554\pm^{8}_{11}$
$M/M_{\odot}$	$1.25\pm^{0.09}_{0.08}$	$0.81\pm^{0.13}_{0.08}$	1.39 ± 0.01	1.39 ± 0.01	$1.07\pm^{0.08}_{0.11}$	
R^{b}, km	$8780\pm^{476}_{267}$	$11001\pm^{799}_{629}$	$5934\pm^{74}_{77}$	$8038\pm^{43}_{42}$	$9541\pm^{601}_{750}$	$10393\pm^{678}_{514}$
L, $10^{37}\,{\rm erg\,s}^{-1}$	$7.0\pm^{0.8}_{0.6}$	$7.4\pm^{1.2}_{1.1}$	4.0 ± 0.1	6.1 ± 0.1	$7.3\pm^{1.2}_{1.3}$	$7.3\pm^{1.0}_{0.9}$
$\log g$	$8.33\pm^{0.06}_{0.04}$	$7.95\pm^{0.09}_{0.07}$	8.72 ± 0.01	8.46 ± 0.01	$8.19\pm^{0.06}_{0.08}$	$8.12\pm^{0.07}_{0.06}$
$\Delta \log g$	$0.41\pm^{0.06}_{0.05}$	$0.20\pm^{0.10}_{0.08}$	0.70 ± 0.01	0.51 ± 0.01	$0.33\pm^{0.08}_{0.09}$	0.33 ± 0.07
$A_{\rm C}$, sol	0.24 ± 0.04	$0.20\pm^{0.05}_{0.04}$	0.22 ± 0.01	0.27 ± 0.01	0.21 ± 0.04	0.16 ± 0.04
$A_{\rm N}$, sol	1.14 ± 0.11	$1.33\pm^{0.11}_{0.14}$	1.28 ± 0.03	1.14 ± 0.03	1.30 ± 0.11	1.44 ± 0.11
`cstat` (dof)[c]	125.00 (125)	144.74 (125)	6548.12 (3323)	7019.75 (3324)	272.91 (252)	

Notes: (a) – hydrogen column density $N_{\rm H}$ is fixed; (b) – the distance to the LMC is assumed to be 50 kpc (Pietrzyński et al., 2019); (c) – the C-statistics and degrees of freedom of the best value found by the Bayesian analysis; (d) – eRASS1 and eRASS2 spectra were fitted simultaneously with a common WD mass M parameter.

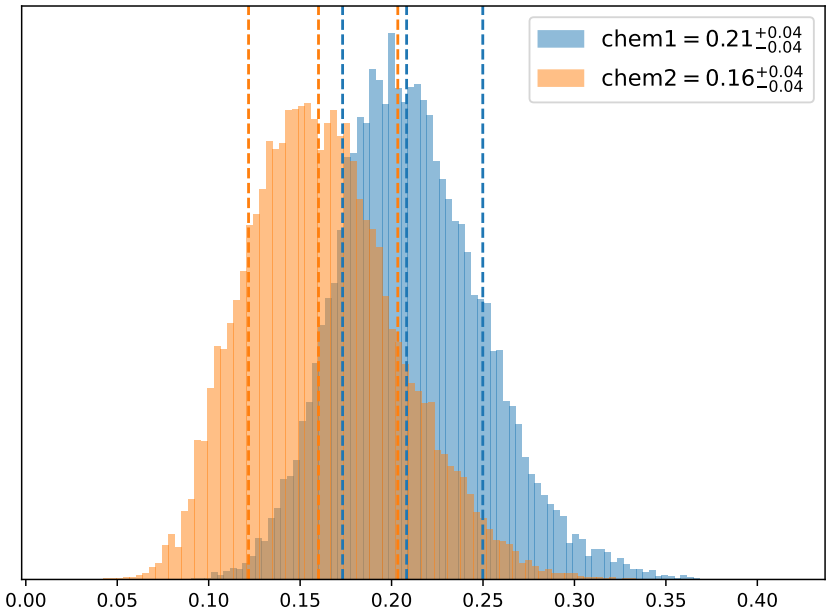

Figure 26: One-dimensional distribution for eRASS1 (in blue) and eRASS2 (in orange) '`chem`'-parameter. Spectra were fitted simultaneously using the Bayesian approach, and the WD mass parameter was common for both spectra. Vertical lines show the 16-, 50- and 84-percentiles for '`chem`' distribution.

The derived hydrogen column density $N_{\rm H}$ differs significantly between the *eROSITA* and *XMM-Newton* spectra. For eRASS1, $N_{\rm H} \approx 5.88 \times 10^{20}\,{\rm cm}^{-2}$, see Table 5, while for *XMM-Newton* $N_{\rm H} \approx 3.06 \times 10^{20}\,{\rm cm}^{-2}$.

The last value is lower than the Galactic absorption column in the direction of the source, $5.6^{+0.7}_{-0.8} \times 10^{20}{\rm cm}^{-2}$ based on the extinction/absorption maps presented in Doroshenko (2024). The HI survey (HI4PI Collaboration et al., 2016) provides the close result $6.5^{+0.1}_{-0.1} \times 10^{20}$ cm^{-2}. Therefore, we consider the *eROSITA*-derived $N_{\rm H}$ value to be more reliable and fix it when fitting the *XMM-Newton* spectrum. Specifically, we fixed $N_{\rm H} = 5.88 \times 10^{20}\,{\rm cm}^{-2}$. The corresponding results are also shown in Table 5, and Fig. 25 shows the RGS1 spectrum comparison.

Interestingly, for both the *XMM-Newton* and eRASS1 spectra, regardless of the other parameters' values, the carbon abundance '`chem`' parameters are consistent, ≈ 0.27 and ≈ 0.24 respectively, both well constrained. The eRASS2 spectrum also provides a good fit, yielding a slightly lower '`chem`' of ≈ 0.20.

With *eROSITA* spectra available for two different epochs, we can examine the evolution of the system parameters, particularly the carbon abundance. To do this, we performed a Bayesian analysis of the eRASS1 and eRASS2 spectra simultaneously using the `chem`-model, assuming that the WD mass is the same in both fits, and, therefore, it is a common free parameter for all spectra. The same uniform priors were set for the hydrogen column density, '`chem`'-parameter, effective temperature, WD mass and radius. The obtained parameter values listed in Table 5.

The posterior distributions of the '`chem`'-parameters are well-constrained, and the corresponding errors are relatively small, as shown in Fig. 26. Note that the hydrogen column density is a free parameter in this case, and it converged to a reasonable value of $5.83 \times 10^{20}\,{\rm cm}^{-2}$. The inferred WD mass, $\approx 1.07\,M_\odot$, is also well-determined.

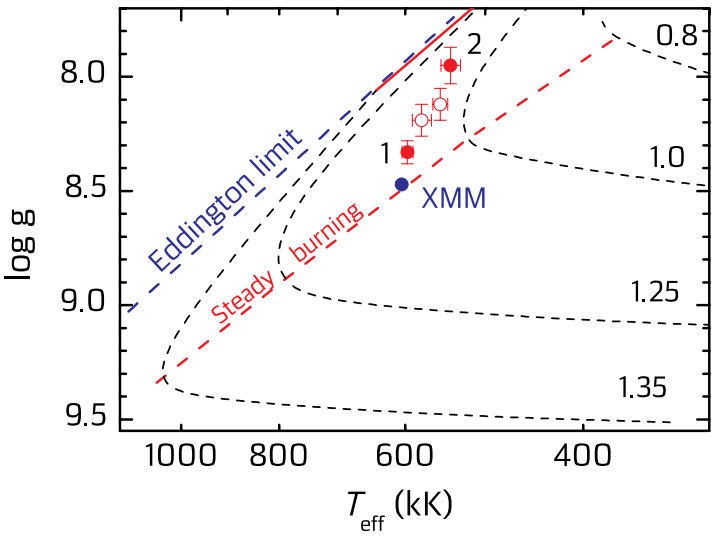

Figure 27: Positions of the source in the $T_{\rm eff} - \log g$ plane according to different eRASS observations (red circles with the number 1 and 2), and according to joint fit (red empty circles), see Table 5. The *XMM-Newton* spectrum fit with fixed $N_{\rm H}$ is shown by the blue circle. Model dependencies for various WD masses, taken from (Nomoto et al., 2007), are shown by black dashed curves. The numbers at the curves indicate WD masses (in solar masses). The boundaries of the stable thermonuclear burning band are shown by the solid (upper boundary) and dashed (lower boundary) red lines. The Eddington limit for solar H/He abundances is shown by the blue dashed line.

5.2.3.1 Discussion

Our combined analysis of the eRASS1 and eRASS2 data allows us to investigate the evolution of the source on a half-year scale. While the WD's effective temperature slightly decreases and the photospheric radius slightly increases, these variations are within the uncertainties. Formally, the carbon abundance appears to decline from 0.21 to 0.16 of the solar value, but given the errors of '`chem`' determination, this difference is not statistically significant, as seen in Fig. 26. Overall, while low-resolution spectral data suggest possible changes in the source parameters, including its chemical composition, longer time-separated observations are needed for a more definitive evolutionary study.

Again, the mass obtained from fitting different spectra varies, with a tendency to approach its upper limit. Therefore, for a more reliable mass determination, we compare the obtained results with theoretical predictions by Nomoto et al. (2007). Figure 27 shows the theoretical $T_{\rm eff} - \log g$ tracks alongside our fit results, including all eRASS observations, the XMM observation with fixed $N_{\rm H}$, and the joint *eROSITA* fit with a common M-parameter.

The source consistently aligns with model predictions for WDs of $1.1 - 1.15\,M_\odot$, although the eRASS2 fit has larger uncertainties. This mass estimate agrees well with our joint eRASS1 and eRASS2 fit, suggesting a likely WD mass of $M = 1.05 - 1.15\,M_\odot$.

Additionally, all fit positions lie above the steady-burning limit for WDs (red dashed line in Fig. 27). This confirms our assumption that the source undergoes steady hydrogen burning on its surface. Furthermore, the eRASS2 position shifts further from the lower boundary of the stable burning strip, indicating an increase in the intensity of the thermonuclear burning from eRASS1 to eRASS2 observations. This fact is supported by the increased bolometric luminosity.

To summarise, our simplified LTE approach provides a satisfactory description of the X-ray spectra of the supersoft X-ray stage of a classical nova and could be useful for interpreting similar objects.

6 Future research

Taken together, Papers I–III contribute to a deeper understanding of supersoft X-ray sources, offering insights into the physical properties of hot accreting white dwarfs. Overall, LTE atmosphere models serve as a valuable tool for analysing SSS spectra. While NLTE models provide a more detailed treatment of the number densities of the ions including excited levels, LTE models offer a practical and effective approach for estimating WD parameters and investigating accreting WDs in various astrophysical environments.

While the current study focused on a limited number of SSSs, future work should apply LTE atmosphere models to a broader range of objects, including numerous other persistent SSSs in the Milky Way and Magellanic Clouds to determine whether similar trends in temperature, mass, and composition hold across different systems. New SSSs are continuously discovered in X-ray surveys, such as the *eROSITA* eRASS survey, and their spectral analysis with LTE models will contribute to a more comprehensive understanding of these objects. Applying LTE models to a diverse sample of SSSs will improve the statistical robustness of WD parameter estimates and help identify variations in their physical properties.

The SSS stage of classical novae makes them valuable targets for atmospheric modelling. Spectral modelling of their evolution will provide insight into how WD atmosphere parameters change as nuclear burning subsides. Analysing the impact of different chemical compositions on the duration and luminosity of the SSS phase will help to determine whether SSS stages of novae follow a predictable evolutionary path and better understand the role of nuclear burning efficiency in long-term accretion and binary evolution.

A major limitation of current LTE models is their assumption of static atmospheres, whereas in reality, radiation pressure in spectral lines can drive atmospheric expansion, especially at the high temperatures found in SSSs. To address this, models must incorporate spherical moving atmospheres with proper radiation transfer. Many SSSs exhibit strong winds that influence their spectra and produce numerous emission lines. Developing self-consistent atmosphere models that account for wind-driven expanding envelopes is crucial for accurately interpreting emission features and determining mass-loss rates. These factors directly impact binary evolution and the likelihood of SSSs as Type Ia supernova progenitors.

Bibliography

Alcock, C. et al. Optical variability of the Large Magellanic Cloud supersoft source RX J0513.9-6951 from MACHO project photometry. MNRAS, 280(4):L49–L53, June 1996. doi: 10.1093/mnras/280.3.L49.

Arnaud, K.A. XSPEC: The First Ten Years. In Jacoby, G.H. and Barnes, J., editors, *Astronomical Data Analysis Software and Systems V*, volume 101 of *Astronomical Society of the Pacific Conference Series*, page 17, January 1996.

Arnaud, K., Dorman, B. and Gordon, C. XSPEC: An X-ray spectral fitting package. Astrophysics Source Code Library, record ascl:9910.005, October 1999.

Asplund, M. et al. The Chemical Composition of the Sun. ARA&A, 47(1):481–522, September 2009. doi: 10.1146/annurev.astro.46.060407.145222.

Baron, E., Chen, B. and Hauschildt, P.H. PHOENIX: A General-purpose State-of-the-art Stellar and Planetary Atmosphere Code. Astrophysics Source Code Library, record ascl:1010.056, October 2010.

Bode, M.F. and Evans, A. *Classical Novae*, volume 43. 2008.

Buchner, J. et al. X-ray spectral modelling of the AGN obscuring region in the CDFS: Bayesian model selection and catalogue. A&A, 564:A125, April 2014. doi: 10.1051/0004-6361/201322971.

Buchner, J. BXA: Bayesian X-ray Analysis. Astrophysics Source Code Library, record ascl:1610.011, October 2016a.

Buchner, J. UltraNest: Pythonic Nested Sampling Development Framework and UltraNest. Astrophysics Source Code Library, record ascl:1611.001, November 2016b.

Buchner, J. Collaborative Nested Sampling: Big Data versus Complex Physical Models. PASP, 131(1004):108005, October 2019. doi: 10.1088/1538-3873/aae7fc.

Buchner, J. UltraNest - a robust, general purpose Bayesian inference engine. *The Journal of Open Source Software*, 6(60):3001, April 2021. doi: 10.21105/joss.03001.

Burwitz, V. et al. First high-resolution Chandra LETGS spectrum of the transient supersoft X-ray source RX J0513.9-6951. *Advances in Space Research*, 40(8): 1294–1298, January 2007. doi: 10.1016/j.asr.2006.11.036.

Burwitz, V. et al. Variability in the cycle length of the supersoft source RX J0513.9-6951. A&A, 481(1):193–198, April 2008. doi: 10.1051/0004-6361:20067010.

Camenzind, M. *Compact objects in astrophysics : white dwarfs, neutron stars, and black holes*. 2007. doi: 10.1007/978-3-540-49912-1.

Cash, W. Parameter estimation in astronomy through application of the likelihood ratio. ApJ, 228:939–947, March 1979. doi: 10.1086/156922.

Chandrasekhar, S. The Maximum Mass of Ideal White Dwarfs. ApJ, 74:81, July 1931. doi: 10.1086/143324.

Chomiuk, L. et al. ASAS-SN 18jj is a classical nova in the LMC. *The Astronomer's Telegram*, 11610:1, May 2018.

Chubb, T.A. et al. Rocket Observation of X-Ray Emission in a Solar Flare. Nature, 179 (4565):861–862, April 1957. doi: 10.1038/179861a0.

Cowley, A.P. et al. Optical counterparts of the Large Magellanic Cloud X-ray point sources. ApJ, 286:196–208, November 1984. doi: 10.1086/162587.

Cowley, A.P. et al. Detection, Identification, and Observed Properties of Large Magellanic Cloud Supersoft X-Ray Sources. ApJ, 418:L63, December 1993. doi: 10.1086/187117.

Cowley, C.R. An approximate Stark broadening formula for use in spectrum synthesis. *The Observatory*, 91:139–140, August 1971.

Crampton, D. et al. CAL 83: A Puzzling X-Ray Source in the Large Magellanic Cloud. ApJ, 321:745, October 1987. doi: 10.1086/165667.

Crampton, D. et al. The Large Magellanic Cloud Supersoft X-Ray Binary RX J0513.9-6951. ApJ, 456:320, January 1996. doi: 10.1086/176653.

de Korte, P.A.J. et al. The X-Ray Imaging Telescopes on EXOSAT. Space Sci. Rev., 30 (1-4):495–511, March 1981. doi: 10.1007/BF01246070.

den Herder, J.W. et al. The Reflection Grating Spectrometer on board XMM-Newton. A&A, 365:L7–L17, January 2001. doi: 10.1051/0004-6361:20000058.

Dere, K.P. et al. CHIANTI - an atomic database for emission lines. A&AS, 125: 149–173, October 1997. doi: 10.1051/aas:1997368.

Doroshenko, V. 3D-$N_{\rm H}$-tool. *arXiv e-prints*, art. arXiv:2403.03127, March 2024. doi: 10.48550/arXiv.2403.03127.

Ducci, L. et al. SRG/eROSITA discovery of a bright supersoft X-ray emission from the classical nova AT 2018bej in the Large Magellanic Cloud. *The Astronomer's Telegram*, 13545:1, March 2020.

Fowler, R.H. On dense matter. MNRAS, 87:114–122, December 1926. doi: 10.1093/mnras/87.2.114.

Gänsicke, B.T. et al. Hubble Space Telescope ultraviolet spectroscopy of the supersoft X-ray binaries CAL83 and RXJ0513.9-6951. A&A, 333:163–171, May 1998.

Garmire, G.P. et al. Advanced CCD imaging spectrometer (ACIS) instrument on the Chandra X-ray Observatory. In Truemper, J.E. and Tananbaum, H.D., editors, *X-Ray and Gamma-Ray Telescopes and Instruments for Astronomy.*, volume 4851 of *Society of Photo-Optical Instrumentation Engineers (SPIE) Conference Series*, pages 28–44, March 2003. doi: 10.1117/12.461599.

Giacconi, R. et al. The Uhuru catalog of X-ray sources. ApJ, 178:281–308, December 1972. doi: 10.1086/151790.

Giacconi, R. et al. The Third UHURU Catalog of X-Ray Sources. ApJS, 27:37, February 1974. doi: 10.1086/190288.

Giacconi, R. et al. Evidence for x Rays From Sources Outside the Solar System. Phys. Rev. Lett., 9(11):439–443, December 1962. doi: 10.1103/PhysRevLett.9.439.

Greiner, J. and Di Stefano, R. X-ray off states and optical variability in CAL 83. A&A, 387:944–954, June 2002. doi: 10.1051/0004-6361:20020463.

Greiner, J., Hasinger, G. and Kahabka, P. ROSAT observation of two supersoft sources in the Large Magellanic Cloud. A&A, 246:L17–L20, June 1991.

Greiner, J. Catalog of supersoft X-ray sources. New A, 5(3):137–141, May 2000. doi: 10.1016/S1384-1076(00)00018-X.

Griem, H.R. Stark Broadening of Higher Hydrogen and Hydrogen-Like Lines by Electrons and Ions. ApJ, 132:883, November 1960. doi: 10.1086/146987.

Griem, H.R. Stark Broadening by Electron and Ion Impacts of NA Hydrogen Lines of Large Principal Quantum Number. ApJ, 148:547, May 1967. doi: 10.1086/149176.

Hachisu, I. and Kato, M. A New Clue to the Transition Mechanism between Optical High and Low States of the Supersoft X-Ray Source RX J0513.9-6951, Implied By the Recurrent Nova CI Aquilae 2000 Outburst Model. ApJ, 588(2):1003–1008, May 2003a. doi: 10.1086/374303.

Hachisu, I. and Kato, M. RX J0513.9-6951: The First Example of Accretion Wind Evolution, a Key Evolutionary Process to Type Ia Supernovae. ApJ, 590(1):445–459, June 2003b. doi: 10.1086/374968.

Hachisu, I. and Kato, M. A Universal Decline Law of Classical Novae. ApJS, 167(1): 59–80, November 2006. doi: 10.1086/508063.

Harris, D.E. et al. The Einstein Observatory catalog of IPC X ray sources. Volume 1E: Documentation. *Einstein Observatory Catalog of IPC X-ray Sources*, 1, January 1990.

Hartmann, H.W. and Heise, J. Hot High-Gravity NLTE Model Atmospheres Applied to Supersoft Sources. In Greiner, J., editor, *Supersoft X-Ray Sources*, volume 472, page 25. 1996. doi: 10.1007/BFb0102241.

Hartmann, H.W. and Heise, J. Hot high-gravity NLTE model atmospheres as soft X-ray sources. A&A, 322:591–597, June 1997.

Hartmann, H.W. et al. Constraining the spectral parameters of RX J0925.7-4758 with the BeppoSAX LECS. A&A, 346:125–133, June 1999. doi: 10.48550/arXiv.astro-ph/9903243.

Hauschildt, P.H. and Baron, E. Numerical solution of the expanding stellar atmosphere problem. *Journal of Computational and Applied Mathematics*, 109(1):41–63, September 1999. doi: 10.48550/arXiv.astro-ph/9808182.

Heise, J., van Teeseling, A. and Kahabka, P. The spectra and luminosity of super-soft X-ray sources. A&A, 288:L45–L48, August 1994.

Henze, M. et al. X-ray monitoring of classical novae in the central region of M 31 III. Autumn and winter 2009/10, 2010/11, and 2011/12. A&A, 563:A2, March 2014. doi: 10.1051/0004-6361/201322426.

HI4PI Collaboration et al. HI4PI: A full-sky H I survey based on EBHIS and GASS. A&A, 594:A116, October 2016. doi: 10.1051/0004-6361/201629178.

Hubeny, I. A computer program for calculating non-LTE model stellar atmospheres. *Computer Physics Communications*, 52(1):103–132, December 1988. doi: 10.1016/0010-4655(88)90177-4.

Hubeny, I. and Lanz, T. Non-LTE Line-blanketed Model Atmospheres of Hot Stars. I. Hybrid Complete Linearization/Accelerated Lambda Iteration Method. ApJ, 439:875, February 1995. doi: 10.1086/175226.

Hubeny, I., Hummer, D.G. and Lanz, T. NLTE model stellar atmospheres with line blanketing near the series limits. A&A, 282:151–167, February 1994.

Hubeny, I. and Lanz, T. TLUSTY: Stellar Atmospheres, Accretion Disks, and Spectroscopic Diagnostics. Astrophysics Source Code Library, record ascl:1109.021, September 2011.

Hummer, D.G. and Mihalas, D. The Equation of State for Stellar Envelopes. I. an Occupation Probability Formalism for the Truncation of Internal Partition Functions. ApJ, 331:794, August 1988. doi: 10.1086/166600.

Ibragimov, A.A. et al. Supersoft X-ray Sources. Parameters of Stellar Atmospheres. *Astronomy Reports*, 47(3):186–196, March 2003. doi: 10.1134/1.1562213.

Jansen, F. et al. XMM-Newton observatory. I. The spacecraft and operations. A&A, 365:L1–L6, January 2001. doi: 10.1051/0004-6361:20000036.

Jimenez-Garate, M.A., Raymond, J.C. and Liedahl, D.A. The Structure and X-Ray Recombination Emission of a Centrally Illuminated Accretion Disk Atmosphere and Corona. ApJ, 581(2):1297–1327, December 2002. doi: 10.1086/344364.

Kahabka, P. Recurrent supersoft X-ray sources. A&A, 304:227, December 1995.

Kahabka, P. Discovery of an X-Ray Off-State in the Supersoft Source CAL 83. In Wickramasinghe, D.T., Bicknell, G.V. and Ferrario, L., editors, *IAU Colloq. 163: Accretion Phenomena and Related Outflows*, volume 121 of *Astronomical Society of the Pacific Conference Series*, page 730, January 1997.

Kahabka, P. Modelling the temporary X-ray off-state of CAL 83. A&A, 331:328–334, March 1998.

Kahabka, P. and van den Heuvel, E.P.J. Luminous Supersoft X-Ray Sources. ARA&A, 35:69–100, January 1997. doi: 10.1146/annurev.astro.35.1.69.

Kahabka, P. et al. Luminous supersoft X-ray emission from the recurrent nova U Scorpii. A&A, 347:L43–L46, July 1999.

Kahabka, P. Supersoft X-ray sources. *Advances in Space Research*, 38(12):2836–2839, January 2006. doi: 10.1016/j.asr.2005.10.058.

Karzas, W.J. and Latter, R. Electron Radiative Transitions in a Coulomb Field. ApJS, 6:167, May 1961. doi: 10.1086/190063.

Kurucz, R.L. Atlas: a Computer Program for Calculating Model Stellar Atmospheres. *SAO Special Report*, 309, February 1970.

Kurucz, R.L. VizieR Online Data Catalog: Model Atmospheres (Kurucz, 1979). *VizieR Online Data Catalog*, art. VI/39, October 1993.

Lanz, T. et al. Non-LTE Model Atmosphere Analysis of the Large Magellanic Cloud Supersoft X-Ray Source CAL 83. ApJ, 619(1):517–526, January 2005. doi: 10.1086/426382.

Long, K.S., Helfand, D.J. and Grabelsky, D.A. A solf X-ray study of the Large Magellanic Cloud. ApJ, 248:925–944, September 1981. doi: 10.1086/159222.

Luminet, J.P. Black Holes: A General Introduction. In Hehl, F.W., Kiefer, C. and Metzler, R.J.K., editors, *Black Holes: Theory and Observation*, volume 514, page 3. 1998. doi: 10.1007/978-3-540-49535-2_1.

Maitra, C. and Haberl, F. Discovery of four super-soft X-ray sources in XMM-Newton observations of the Large Magellanic Cloud. A&A, 657:A26, January 2022. doi: 10.1051/0004-6361/202142159.

Mason, K.O. et al. The XMM-Newton optical/UV monitor telescope. A&A, 365: L36–L44, January 2001. doi: 10.1051/0004-6361:20000044.

McGowan, K.E. et al. XMM spectroscopy of the transient supersoft source RXJ0513.9 - 6951: probing the dynamic white dwarf photosphere. MNRAS, 364(2):462–474, December 2005. doi: 10.1111/j.1365-2966.2005.09566.x.

Merloni, A. et al. The SRG/eROSITA all-sky survey. First X-ray catalogues and data release of the western Galactic hemisphere. A&A, 682:A34, February 2024. doi: 10.1051/0004-6361/202347165.

Mihalas, D. *Stellar atmospheres*. 1978.

Murray, S.S. et al. In-flight performance of the Chandra high-resolution camera. In Truemper, J.E. and Aschenbach, B., editors, *X-Ray Optics, Instruments, and Missions III*, volume 4012 of *Society of Photo-Optical Instrumentation Engineers (SPIE) Conference Series*, pages 68–80, July 2000. doi: 10.1117/12.391591.

Nauenberg, M. Analytic Approximations to the Mass-Radius Relation and Energy of Zero-Temperature Stars. ApJ, 175:417, July 1972. doi: 10.1086/151568.

Ness, J.U. Observational evidence for expansion in the SSS spectra of novae. *Astronomische Nachrichten*, 331(2):179–182, February 2010. doi: 10.1002/asna.200911322.

Ness, J.U. et al. A Chandra Low Energy Transmission Grating Spectrometer Observation of V4743 Sagittarii: A Supersoft X-Ray Source and a Violently Variable Light Curve. ApJ, 594(2):L127–L130, September 2003. doi: 10.1086/378664.

Ness, J.U. et al. Obscuration effects in super-soft-source X-ray spectra. A&A, 559:A50, November 2013. doi: 10.1051/0004-6361/201322415.

Nomoto, K. et al. Thermal Stability of White Dwarfs Accreting Hydrogen-rich Matter and Progenitors of Type Ia Supernovae. ApJ, 663(2):1269–1276, July 2007. doi: 10.1086/518465.

Odendaal, A. et al. Optical and X-ray properties of CAL 83 - II. An X-ray pulsation at ∼67 s. MNRAS, 437(3):2948–2956, January 2014. doi: 10.1093/mnras/stt2111.

Orio, M., Covington, J. and Ögelman, H. X-ray emission from classical and recurrent novae observed with ROSAT. A&A, 373:542–554, July 2001. doi: 10.1051/0004-6361:20010537.

Orio, M. et al. NICER Monitoring of Supersoft X-Ray Sources. ApJ, 932(1):45, June 2022. doi: 10.3847/1538-4357/ac63be.

Paerels, F. et al. A high resolution spectroscopic observation of CAL 83 with XMM-Newton/RGS. A&A, 365:L308–L311, January 2001. doi: 10.1051/0004-6361:20000069.

Pakull, M.W. et al. Optical/UV counterpart of the supersoft transient X-ray source RX J0513.9-6951 in the Large Magellanic Cloud. A&A, 278:L39–L42, November 1993.

Parmar, A.N. et al. A BeppoSAX observation of the super-soft source CAL87. A&A, 323:L33–L36, July 1997. doi: 10.48550/arXiv.astro-ph/9706008.

Parmar, A.N. et al. A BeppoSAX LECS observation of the super-soft X-ray source CAL 83. A&A, 332:199–203, April 1998. doi: 10.48550/arXiv.astro-ph/9712040.

Petz, A. et al. Modeling CHANDRA low energy transmission grating spectrometer observations of classical novae with PHOENIX. I. V4743 Sagittarii. A&A, 431: 321–328, February 2005. doi: 10.1051/0004-6361:20041396.

Pietrzyński, G. et al. A distance to the Large Magellanic Cloud that is precise to one per cent. Nature, 567(7747):200–203, March 2019. doi: 10.1038/s41586-019-0999-4.

Predehl, P. et al. The eROSITA X-ray telescope on SRG. A&A, 647:A1, March 2021. doi: 10.1051/0004-6361/202039313.

Rappaport, S., Di Stefano, R. and Smith, J.D. Formation and Evolution of Luminous Supersoft X-Ray Sources. ApJ, 426:692, May 1994. doi: 10.1086/174106.

Rauch, T. A grid of synthetic ionizing spectra for very hot compact stars from NLTE model atmospheres. A&A, 403:709–714, May 2003. doi: 10.1051/0004-6361:20030412.

Rauch, T. and Werner, K. Non-LTE model atmospheres for supersoft X-ray sources. *Astronomische Nachrichten*, 331(2):146, February 2010. doi: 10.1002/asna.200911316.

Rauch, T. et al. Non-local Thermal Equilibrium Model Atmospheres for the Hottest White Dwarfs: Spectral Analysis of the Compact Component in Nova V4743 Sgr. ApJ, 717(1):363–371, July 2010. doi: 10.1088/0004-637X/717/1/363.

Reinsch, K. et al. Optical low states of the supersoft X-ray source RX J0513.9-6951. A&A, 309:L11–L14, May 1996.

Reinsch, K. et al. A limit-cycle model for the binary supersoft X-ray source RX J0513.9-6951. A&A, 354:L37–L40, February 2000. doi: 10.48550/arXiv.astro-ph/0001081.

Schaeidt, S., Hasinger, G. and Truemper, J. Discovery of a variable supersoft X-ray source in the Large Magellanic Cloud during the ROSAT all-sky survey. A&A, 270: L9–L12, March 1993.

Schwartz, D.A. et al. Absolute effective area of the Chandra high-resolution mirror assembly (HRMA). In Truemper, J.E. and Aschenbach, B., editors, *X-Ray Optics, Instruments, and Missions III*, volume 4012 of *Society of Photo-Optical Instrumentation Engineers (SPIE) Conference Series*, pages 28–40, July 2000. doi: 10.1117/12.391566.

Seaton, M.J. et al. Opacities for stellar envelopes. MNRAS, 266:805, February 1994. doi: 10.1093/mnras/266.4.805.

Seward, F.D. and Mitchell, M. X-ray survey of the Small Magellanic Cloud. ApJ, 243: 736–743, February 1981. doi: 10.1086/158641.

Shore, S.N. Astronomy: Cosmic exhumation. Nature, 548(7669):526–527, August 2017. doi: 10.1038/548526a.

Skopal, A. Multiwavelength Modeling the SED of Luminous Supersoft X-Ray Sources in Large Magellanic Cloud and Small Magellanic Cloud. AJ, 164(4):145, October 2022. doi: 10.3847/1538-3881/ac897d.

Soraisam, M.D. et al. Population of post-nova supersoft X-ray sources. MNRAS, 455(1): 668–679, January 2016. doi: 10.1093/mnras/stv2359.

Southwell, K.A. et al. The Nature of the Supersoft X-Ray Source RX J0513-69. ApJ, 470:1065, October 1996. doi: 10.1086/177931.

Starrfield, S. et al. Surface Hydrogen-burning Modeling of Supersoft X-Ray Binaries: Are They Type Ia Supernova Progenitors? ApJ, 612(1):L53–L56, September 2004. doi: 10.1086/424513.

Starrfield, S., Iliadis, C. and Hix, W.R. The Thermonuclear Runaway and the Classical Nova Outburst. PASP, 128(963):051001, May 2016. doi: 10.1088/1538-3873/128/963/051001.

Stecchini, P.E. et al. Revisiting multiwavelength data on the supersoft X-ray source CAL 83. MNRAS, 522(3):3472–3480, July 2023. doi: 10.1093/mnras/stad1144.

Strüder, L. et al. The European Photon Imaging Camera on XMM-Newton: The pn-CCD camera. A&A, 365:L18–L26, January 2001. doi: 10.1051/0004-6361:20000066.

Suleimanov, V., Meyer, F. and Meyer-Hofmeister, E. Efficiency of soft X-ray radiation reprocessing in supersoft X-ray sources. A&A, 350:63–72, October 1999.

Suleimanov, V., Meyer, F. and Meyer-Hofmeister, E. High efficiency of soft X-ray radiation reprocessing in supersoft X-ray sources due to multiple scattering. A&A, 401:1009–1015, April 2003. doi: 10.1051/0004-6361:20030159.

Suleimanov, V.F. and Ibragimov, A.A. Supersoft X-ray Sources: Basic Parameters. *Astronomy Reports*, 47(3):197–205, March 2003. doi: 10.1134/1.1562214.

Sutherland, R.S. Accurate free-free Gaunt factors for astrophysical plasmas. MNRAS, 300(2):321–330, October 1998. doi: 10.1046/j.1365-8711.1998.01687.x.

Swartz, D.A. et al. Chandra Discovery of Luminous Supersoft X-Ray Sources in M81. ApJ, 574(1):382–397, July 2002. doi: 10.1086/340926.

Truemper, J. The ROSAT mission. *Advances in Space Research*, 2(4):241–249, January 1982. doi: 10.1016/0273-1177(82)90070-9.

Trümper, J. et al. X-ray survey of the Large Magellanic Cloud by ROSAT. Nature, 349 (6310):579–583, February 1991. doi: 10.1038/349579a0.

Turner, M.J.L. et al. The European Photon Imaging Camera on XMM-Newton: The MOS cameras. A&A, 365:L27–L35, January 2001. doi: 10.1051/0004-6361:20000087.

van den Heuvel, E.P.J. et al. Accreting white dwarf models for CAL 83, CAL 87 and other ultrasoft X-ray sources in the LMC. A&A, 262:97–105, August 1992.

van Rossum, D.R. and Ness, J.U. Expanding atmosphere models for SSS spectra of novae. *Astronomische Nachrichten*, 331(2):175, February 2010. doi: 10.1002/asna.200911321.

van Rossum, D.R. A Public Set of Synthetic Spectra from Expanding Atmospheres for X-Ray Novae. I. Solar Abundances. ApJ, 756(1):43, September 2012. doi: 10.1088/0004-637X/756/1/43.

Verner, D.A. et al. Atomic Data for Astrophysics. II. New Analytic FITS for Photoionization Cross Sections of Atoms and Ions. ApJ, 465:487, July 1996. doi: 10.1086/177435.

Weisskopf, M.C. et al. Chandra X-ray Observatory (CXO): overview. In Truemper, J.E. and Aschenbach, B., editors, *X-Ray Optics, Instruments, and Missions III*, volume 4012 of *Society of Photo-Optical Instrumentation Engineers (SPIE) Conference Series*, pages 2–16, July 2000. doi: 10.1117/12.391545.

Werner, K. et al. Model Photospheres with Accelerated Lambda Iteration. In Hubeny, I., Mihalas, D. and Werner, K., editors, *Stellar Atmosphere Modeling*, volume 288 of *Astronomical Society of the Pacific Conference Series*, page 31, January 2003. doi: 10.48550/arXiv.astro-ph/0209535.

Werner, K., Dreizler, S. and Rauch, T. TMAP: Tübingen NLTE Model-Atmosphere Package. Astrophysics Source Code Library, record ascl:1212.015, December 2012.

Wolf, W.M. et al. Hydrogen Burning on Accreting White Dwarfs: Stability, Recurrent Novae, and the Post-nova Supersoft Phase. ApJ, 777(2):136, November 2013. doi: 10.1088/0004-637X/777/2/136.

Zhao, W. et al. A robust model for the origin of optical quasi-periodic variability in supersoft X-ray sources. A&A, 666:A81, October 2022. doi: 10.1051/0004-6361/202243759.

Appendix A: Original Publications

Published works are presented here as originally published, with the permission of the publishers. Copyright holders with the corresponding copyright notices are listed below.

Paper I

V. Suleimanov, A. Tavleev, V. Doroshenko, K. Werner

"Application of hydrostatic local thermodynamic equilibrium atmosphere models to interpretations of supersoft X-ray source spectra"

Astronomy & Astrophysics, 2024, 688, A39

I

A&A, 688, A39 (2024)
https://doi.org/10.1051/0004-6361/202449370

Astronomy & Astrophysics

Application of hydrostatic local thermodynamic equilibrium atmosphere models to interpretations of supersoft X-ray source spectra

V. F. Suleimanov, A. S. Tavleev, V. Doroshenko, and K. Werner

Institut für Astronomie und Astrophysik, Kepler Center for Astro and Particle Physics, Universität Tübingen, Sand 1, 72076 Tübingen, Germany
e-mail: suleimanov@astro.uni-tuebingen.de

Received 28 January 2024 / Accepted 23 May 2024

ABSTRACT

Supersoft X-ray sources (SSSs) are accreting white dwarfs (WDs) with stable or recurrent thermonuclear burning on their surfaces. High-resolution X-ray spectra of such objects are rather complex, often consist of several components, and are difficult to interpret accurately. The main emission source is the hot surface of the WD and the emergent radiation can potentially be described by hot WD model atmospheres. We present a new set of such model atmosphere spectra computed in the effective temperature range from 100 kK to 1000 kK, for eight values of surface gravity and three different chemical compositions. These compositions correspond to the solar one as well as to the Large and Small Magellanic Clouds, with decreased heavy element abundances, at one-half and one-tenth of the solar value. The presented model grid covers a broad range of physical parameters and, thus, it can be applied to a wide range of objects. It is also publicly available in XSPEC format. As an illustration, we applied it here for the interpretation of *Chandra* and XMM grating spectra of two classical SSSs, namely, CAL 83 (RX J0543.5−6823) and RX J0513.9−6951. The obtained effective temperatures and surface gravities of $T_{\rm eff} \approx 560$ kK, $\log g \approx 8.6$–8.7, and $T_{\rm eff} \approx 630$ kK, $\log g \approx 8.5$–8.6, respectively, are in a good agreement with previous estimations for both sources. The derived WD mass estimations are within 1.1–1.4 $M_\odot$ for CAL 83 and 1.15–1.4 $M_\odot$ for RX J0513.9−6951. The mass of the WD in CAL 83 is consistent with the mass predicted from the respective model of recurrent thermonuclear burning.

Key words. accretion, accretion disks – stars: atmospheres – white dwarfs – X-rays: binaries – X-rays: individuals: CAL 83 – X-rays: individuals: RX J0513.9-6951

1. Introduction

Supersoft sources (SSSs) are close binary systems that involve a white dwarf (WD) undergoing accretion as the primary component. The accretion rate is high enough for (quasi-)stable thermonuclear burning to occur on the WD surface (van den Heuvel et al. 1992). These sources were initially discovered in the Large Magellanic Cloud (LMC) by the *Einstein* observatory in the early 1980s (Long et al. 1981) and were classified as a distinct class of sources following ROSAT observations (Trümper et al. 1991; Greiner et al. 1991). The X-ray spectra of SSSs observed by ROSAT were very soft, with blackbody temperatures $kT \sim 30$–40 eV. Formally, these temperatures and the observed fluxes led to luminosities exceeding the Eddington limit for a solar mass object at the LMC distance. This issue was resolved through the implementation of hot WD model atmosphere spectra for interpreting the X-ray spectra of SSSs (Heise et al. 1994). The results of early investigations of SSSs in this context were presented and discussed by Kahabka & van den Heuvel (1997).

In addition to the classical SSSs, super-soft X-ray phases occur during nova explosions. The hot WD with ongoing thermonuclear burning on the surface becomes visible in soft X-rays after the dispersal of an optically thick envelope (see, e.g., Kahabka et al. 1999; Orio et al. 2001; Ness et al. 2003; Schwarz et al. 2011, and references therein).

Model atmospheres and their theoretical spectra are important ingredients in investigating the nature of SSSs and determining their basic parameters. The first models were computed (Heise et al. 1994) under the assumption of local thermodynamic equilibrium (LTE), but non-LTE model atmospheres of hot WDs were subsequently developed as well (Hartmann & Heise 1997). The first non-LTE models did not include spectral lines, but later a number of spectral lines were incorporated (Hartmann et al. 1999), using the publicly available code `TLUSTY` (Hubeny 1988). For the interpretation of the X-ray spectrum of the bright classical SSS CAL 83, Lanz et al. (2005) used more accurate non-LTE model atmospheres. Such models were further developed to analyse the super-soft phase of nova V4743 Sgr (Rauch et al. 2010), where various chemical compositions of the atmospheres as well as the metal-line blanketing effects were considered. These models were calculated using the Tübingen non-LTE Model Atmosphere Package (`TMAP`, Werner et al. 2003; Rauch & Werner 2010). Unfortunately, the accurate computation of non-LTE models is very computation-time expensive, so only small regions of physical parameter space can be probed and models are typically tailored to individual objects.

In addition to non-LTE effects in hydrostatic model atmospheres, expansion due to radiation pressure force in spectral lines could also be important for high temperatures reached in the SSSs. Expanding model atmospheres were thus considered and computed by van Rossum & Ness (2010) and van Rossum (2012) using the publicly available code `PHOENIX` (see, e.g., Hauschildt et al. 1997). Further observational evidence of SSS atmosphere expansion was presented

by Ness (2010). Again, modelling these effects, especially in a non-LTE approximation, is challenging, precluding a full exploration of the parameter space.

On the other hand, LTE model atmospheres of hot WDs can be computed much faster, and, despite their simplicity, were successfully used to interpret ROSAT spectra of SSSs (Ibragimov et al. 2003; Suleimanov & Ibragimov 2003), and a few SSSs found in M81 (Swartz et al. 2002). However, the high-resolution grating spectra obtained by *Chandra* and *XMM-Newton* observatories demonstrated that the hot WD model spectra cannot completely describe observations and reproduce only the common spectral shape with separate strong absorption lines in some cases. This holds true for both hydrostatic and expanding non-LTE model atmospheres (Ness 2020), suggesting that there may be some missing physical processes and additional X-ray emission sources, such as inner accretion disc or boundary layers. Nevertheless, basic SSS parameters appear to be well recovered. Moreover, LTE atmospheres have some advantages compared to sophisticated non-LTE expanding model atmospheres. Hydrostatic LTE model atmospheres are simpler to compute and, what is more important, allow us to consider an almost unlimited number of chemical elements, ions, and spectral lines. Therefore, extended sets of LTE model atmospheres computed for various chemical compositions could potentially be useful for the approximate estimation of basic physical parameters of hot WDs in SSSs and the chemical composition of their atmospheres. The latter problem is especially important, for instance, for the super-soft phases of nova explosions.

Here, we present a set of hot WD model spectra computed for three chemical compositions of the atmospheres: the solar abundance, typical for the Galaxy; the solar H/He mix with the heavy element abundances reduced by a factor of 2 (typical for the LMC, see, e.g., Rolleston et al. 2002); and by a factor of 10 (typical for the Small Magellanic Cloud (SMC), see, e.g., Carrera et al. 2008) in comparison with the solar abundance. We employed the approach previously used for computing the boundary layer spectrum in the dwarf nova SS Cyg (Suleimanov et al. 2014a). A preliminary version of this set of models has also already been used to fit a nova spectrum in fireball phase (König et al. 2022).

The remainder of this paper is organised as follows. In Sect. 2, we describe the method of computation of the atmospheric models, in particular, our new approach to calculate photoionisation opacities. In Sect. 3, we first present the characteristics of the resulting new set of model atmosphere spectra. Then we apply the obtained set to analyse X-ray spectra of the classical SSSs CAL 83 and RX J0513.9−6951. The results of this analysis are discussed in the context of WD evolution in Sect. 4. We summarize our results in Sect. 5.

2. Method

2.1. Basic assumptions

In this work, we use a standard method for computing hydrostatic plane-parallel model atmospheres (see, e.g., Mihalas 1978) and the code based on the popular Kurucz's code ATLAS (Kurucz 1970, 1993b), modified for high temperatures by Ibragimov et al. (2003); see also Suleimanov et al. (2013, 2014a). The general temperature correction scheme for model computation is the same as in ATLAS and the main changes concern the calculation of the opacities and number densities .

We took into account the 15 most abundant chemical elements and the number densities of all ionization and excitation states of all the ions were computed, using the Boltzmann and Saha equations, assuming LTE. We considered pressure ionization and level dissolution effects using the occupation probability formalism (Hummer & Mihalas 1988), as described by Hubeny et al. (1994). We used the spectral line list together with necessary physical parameters such as gf values and the energies of the low-energy levels presented in the CHIANTI database (Dere et al. 1997; Del Zanna et al. 2021). The shapes of line absorption opacity are considered as Voigt profiles. Classical damping broadening was used together with the Tübingen approximation for Stark broadening (Cowley 1971; Werner et al. 2003). The lines of hydrogen-like ions are considered using Griem's theory of linear Stark broadening (Griem 1960, 1967). The modified Kurucz's subroutine (Kurucz 1970) was used for this purpose. We note, however, that the Stark broadening for the lines of the highly charged hydrogen-like ions is small ($\sim Z^{-5}$) in comparison with the radiation damping. A low microturbulent velocity value of $2\,\mathrm{km\,s^{-1}}$ was added to the thermal velocity of ions to account for Doppler line broadening[1].

Formally, the radiation pressure force in spectral lines, $g_{\rm rad}$, exceeds the gravity, g, at the upper atmosphere layers and wind model atmospheres have to be used. However, we employed a simple trick, suggested by Ibragimov et al. (2003), to keep the atmosphere in hydrostatic equilibrium. It was assumed that the gas pressure equals 10% of the total pressure, $P_{\rm g} = 0.1\ P_{\rm tot} = 0.1\ gm$, at all depths where $g_{\rm rad} > g$. Here, m is a column density ($\mathrm{d}m = -\rho \mathrm{d}z$), the independent depth variable in our model, ρ is the plasma density, and z is the geometrical depth. This assumption, in fact, corresponds to a specific velocity law in the upper atmosphere layers, $v(z) \sim \rho(z)^{-1}$. This approach is the simplest way to avoid the hydrostatic equilibrium violation. All other reasonable methods significantly complicate the atmosphere modeling. For instance, this would require consideration of spherical moving atmospheres, including radiation transfer. That is why we limited ourselves to the proposed method.

To calculate the bound-free opacities from the atomic ground states of all ions, we utilized the procedure presented by Verner et al. (1996). The most significant changes for our present model calculations are associated with the photoionization opacities from the excited energy levels of heavy element ions. The method for estimating these opacities and the obtained results are presented in the next subsection.

The free-free opacities of all ions are calculated under the assumption that the ion's electric field is a Coulomb field of charge, Ze, corresponding to the ionic charge number, Z, with e being the elementary charge. The corresponding Gaunt factors are computed following Sutherland (1998).

2.2. Photoionization from excited energy levels

Two different approaches for the photoionization and free-free opacities from the excited levels can be used to consider excited levels of hydrogen-like and helium-like ions and of other ions separately. The approach suggested by Karzas & Latter (1961) and the corresponding Kurucz subroutine (Kurucz 1993a) was used for these ions. The same approach was applied to carbon model atmospheres of neutron stars (Suleimanov et al. 2014b). Photoionization cross-sections from excited levels were computed assuming a Coulomb field of a point-like charge. This approach provides excellent results for hydrogen-like ions, as

[1] A local subset with the microturbulent velocity equal to the local sound speed was computed for the CAL 83 spectrum fitting (see below). The fitting result changed insignificantly.

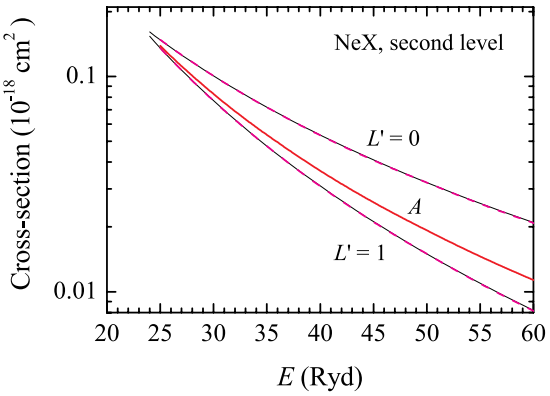

Fig. 1. Comparison of the photoionization cross-sections of the lowest excited levels of the hydrogen-like ion Ne X with the orbital quantum numbers $L' = 0$ and 1, computed by OP (thin black curves) and by the used approximation (dashed magenta curves). The g-factor weighted averaged over both sub-level cross-sections is shown by the red curve.

shown in Fig. 1. However, it is not strictly correct for helium-like ions, as the inner (non-excited) electron is included in the point-like effective charge. This leads to some deviations from the exact cross-sections (see Fig. 2). Nevertheless, the obtained accuracy is acceptable for our purposes. We included five excited levels for hydrogen-like ions and ten levels for helium-like ions.

Another approach is used for ions with more than two electrons. The absorption opacities from the excited levels of these ions were computed by the Opacity Project (OP, Seaton et al. 1994) and are available as numerical tables in the TOPBase database[2]. We used these tables for creating simplified analytical fits and implemented these fits in our code. Only a few levels with the lowest excitation energies were considered, typically not exceeding a quarter of the ionization energy. Although it should be noted that the choice of the levels under consideration was quite arbitrary.

The cross-section for each considered level was fitted using the expression suggested by Kurucz (1970):

$$\sigma(E) = \sigma_{\rm th}\left(A\bar{E}^{p/2} + (1-A)\bar{E}^{1+p/2}\right), \quad (1)$$

where $\bar{E} = E_{\rm th}/E$, E is the photon energy, $E_{\rm th}$ is the threshold photoionization energy from the given level, and $\sigma_{\rm th}$ is the photoionization cross-section at the photoionization threshold. The cross-section is a fitting parameter as well as the parameters A and p. The values $E_{\rm th}$ and the obtained fitting parameters $\sigma_{\rm th}$, A and p together with the level statistical weight g for the approximation (1) for lower excited levels of C, N, O, Ne, Na, Mg, Al, Si, S, Ar, Ca, and Fe ions are publicly available[3]. Some examples of the fitting are shown in Figs. 3 and 4. We note that our smooth fits ignore the auto-ionization resonances (see Fig. 3) and OP cross-sections significantly differ from the old ones used in ATLAS9. Simpler ions with one electron in the outer shell have smooth cross-section dependencies, approximated with a high level of accuracy (Fig. 4).

The excited levels of the helium-like iron ion have more complicated cross-section dependencies on the photon energy, consisting of two parts. The low-energy one just above the photoionization threshold is well fitted with the approach used for other helium-like ions. However, at some energy, approximately ten times larger than the photoionization threshold energy, the cross-section sharply increases. We considered this second part as an additional photoionization edge and approximated it using Eq. (1). The comparison of these double fitting with the computed cross-section for one of the excited levels of Fe XXV is shown in Fig. 5.

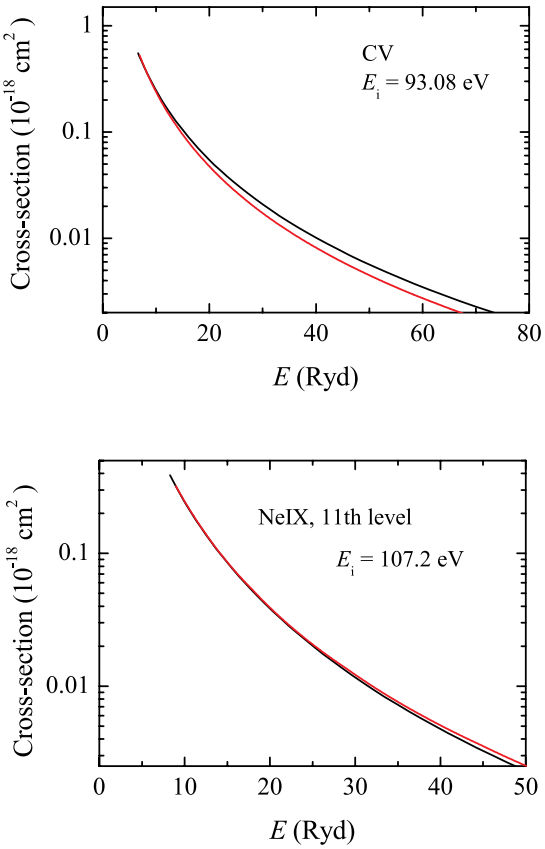

Fig. 2. Comparison of the photoionization cross-sections from the first excited level of the helium-like ion C V (top panel) and 11th excited level of helium-like ion Ne IX (bottom panel), computed by OP (solid black curves) and by the used approximation (red curves). The excitation energies of the levels are also shown.

3. Results

3.1. Model atmospheres

We computed three sets of two-parameter plane-parallel hot WD model atmospheres with different chemical compositions. All the sets have the same solar hydrogen-helium mix and different abundances of heavy elements: the solar one ($A = 1$), half the solar abundance ($A = 0.5$), which corresponds to the LMC heavy element abundance, and ten times less than the solar one ($A = 0.1$), which is close to the heavy element abundance in the SMC. The model parameters of each set are the effective temperature, $T_{\rm eff}$ (100 to 1000 kK in steps of 25 kK), and $\Delta \log g = \log g - \log g_{\rm Edd}$, which characterises the distance of the model from the Eddington limit:

$$\log g_{\rm Edd} = \log(\sigma_{\rm e}\sigma_{\rm SB}\, T_{\rm eff}^4\, c^{-1}) = 4.818 + 4\,\log(T_{\rm eff}/10^5\,{\rm K}), \quad (2)$$

where $\sigma_{\rm SB}$ is the Stefan-Boltzmann constant, c is the speed of light, and $\sigma_{\rm e} = 0.2(1+X) \approx 0.34\,{\rm cm^2\,g^{-1}}$. Here, $X \approx 0.7374$ is the hydrogen mass fraction. The parameter $\Delta \log g$ has eight values in the grid: 0.1, 0.2, 0.4, 0.6, 1.0, 1.4, 1.8, and 2.2. Altogether,

[2] https://cdsweb.u-strasbg.fr/topbase/topbase.html
[3] https://doi.org/10.5281/zenodo.10277303

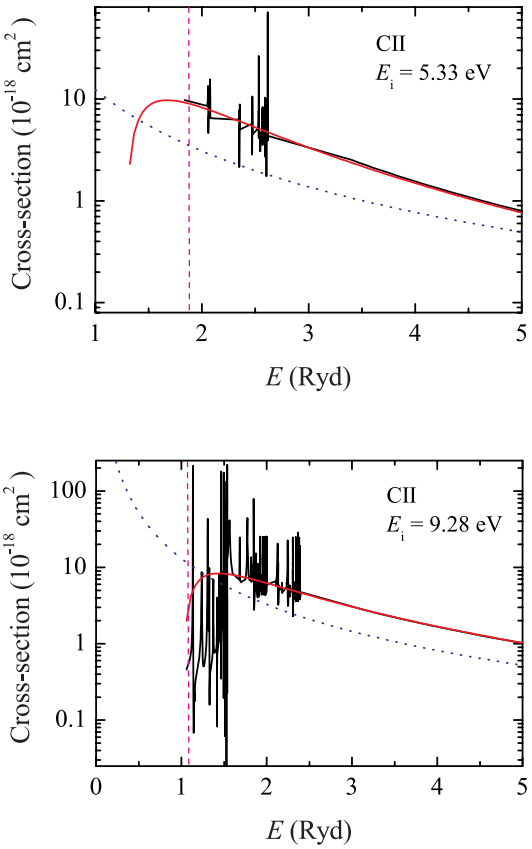

Fig. 3. Comparison of the photoionization cross-sections from two excited levels of C II. Cross-sections computed by OP (solid black curves), the approximation used in ATLAS9 (dashed blue curves), and our fits (red curves). Vertical dashed lines correspond to the ionization thresholds.

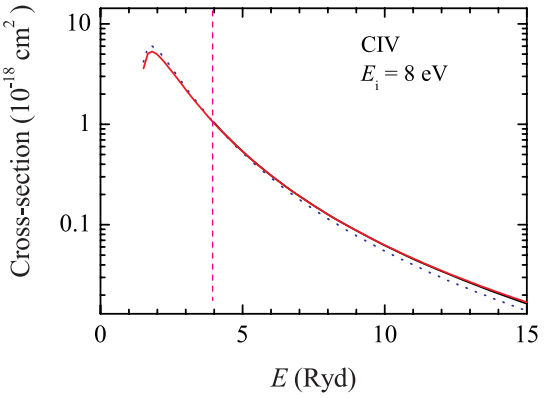

Fig. 4. Same as in Fig. 3 for the first excited level of C IV. Black and red curves overlap and are close also to ATLAS9 approximation (blue dashed curve) here.

296 spectra were computed in every set and implemented as table model[4] for XSPEC[5] (Arnaud 1996; Arnaud et al. 1999).

The properties of the model atmosphere spectra are illustrated in Figs. 6–10. A comparison of the model spectrum computed with the LTE code described above with the hottest non-LTE model atmosphere spectrum presented by Rauch (2003) is

[4] https://github.com/HEASARC/xspec_localmodels/tree/master/sss_atm
[5] https://heasarc.gsfc.nasa.gov/docs/xanadu/xspec/

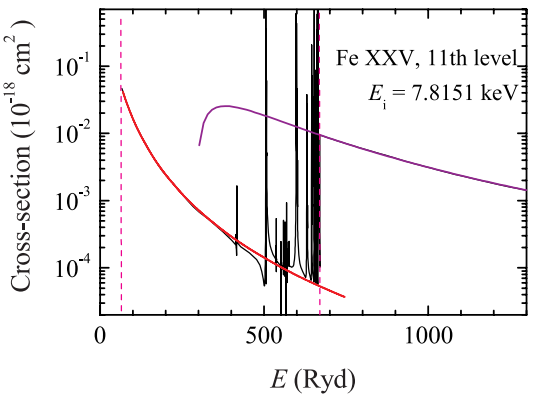

Fig. 5. Comparison of the photoionization cross-sections from the 11th excited level of the helium-like ion Fe XXV. Shown are cross-sections computed by OP (solid black curve) and the used approximation by two fitting functions (red curves). More details in the text. The fitting function thresholds are indicated by the vertical dashed magenta lines.

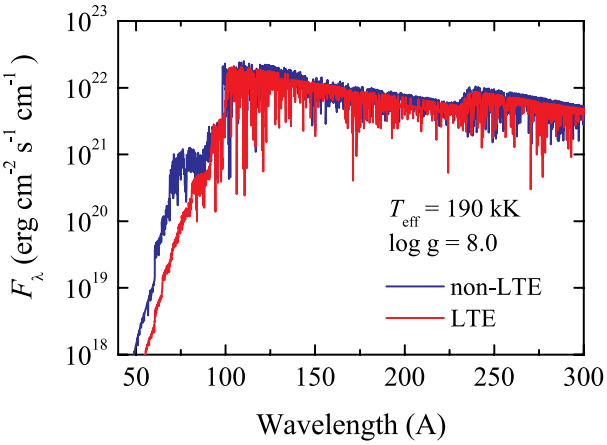

Fig. 6. Comparison of the emergent spectra of the model atmospheres computed by the code presented here (red curves), and the TMAP non-LTE code (Rauch 2003, blue curves). All models have solar chemical composition, $T_{\rm eff}$ = 190 kK, $\log g$ = 8.0.

shown in Fig. 6 (top panel). Both spectra were binned with a 0.1 Å wide step. The general shapes of the spectra are similar, and some differences appear at small wavelengths where the emergent flux is insignificant. It could be due to both non-LTE effects and the difference in the number of excited levels taken into consideration. The lists of the used spectral lines are also different, leading to diverse contributions of the lines to the spectra.

The model spectrum of the fiducial model atmosphere ($T_{\rm eff}$ = 500 kK, $\Delta \log g$ = 0.6, and A = 0.5) is shown in Fig. 7. The upper panel presents, in the observed soft X-ray wavelength range, the spectrum, the corresponding Planck function, and the spectrum convolved with a Gaussian kernel (the kernel resolution R = 300 corresponds the *Chandra* grating resolution). The convolved spectrum demonstrates emission line-like structures, which are, in fact, parts of the spectrum with a small number of spectral lines. A detail of the spectrum near the C V ground state photoionization edge is shown in the bottom panel. The most prominent absorption lines are identified. It is clearly seen that along with the Lyman-like line series of the hydrogen-like C V

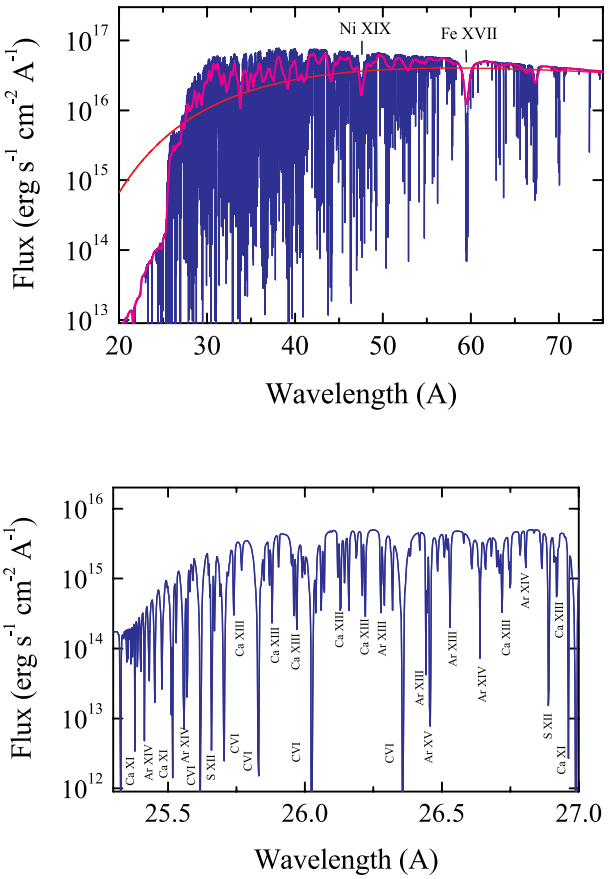

Fig. 7. Spectrum of the model atmosphere with $T_{\rm eff}$ = 500 kK, $\Delta \log g$ = 0.6 and A = 0.5 (top). The Planck function with the same temperature is also shown by the red curve. The spectrum convolved with a Gaussian kernel with the *Chandra* resolution, R = 300, is shown in magenta. Detail of the upper spectrum near the C V ground state edge with spectral line identifications (bottom).

ion, there are numerous absorption lines of ions of heavier elements with about 10 electrons in their shells. We note that the absorption lines of these ions dominate in the overall spectrum.

There is an important note about our assumption that $P_{\rm g} = 0.1 g\, m$ at the upper atmospheric layers where the radiation force due to numerous spectral lines is greater than the WD gravity ($g_{\rm rad} > g$). In fact, most of the escaping radiation aside from the strong line cores, forms in the hydrostatic layers, at least for models with $\Delta \log g \geq 0.4$, see Fig. 8. The depths where the escaping radiation forms, namely $m(\tau_\lambda = 1)$, are shown there. Here, τ_λ is the optical depth at a wavelength λ. The boundaries between the hydrostatic and the wind-dominated layers ($g_{\rm rad} = g$) are also shown. In the model with $\Delta \log g = 0.2$, a significant part of the lines forms in the wind layers and it is even more prominent in the models with less $\Delta \log g$. Therefore, we conclude that the used assumption is acceptable for models with $\Delta \log g \geq 0.4$. The models with smaller $\Delta \log g$ should be used with caution.

The dependence of the emergent spectrum on the effective temperature with fixed $\Delta \log g$ = 0.6 and A = 0.5 is shown in Fig. 9 (here and in the next figure, the convolved spectra are shown). As expected, with increasing $T_{\rm eff}$ the spectrum becomes harder. Decreasing the surface gravity also makes the emergent spectrum harder if other parameters are not changed (Fig. 10, top panel). The influence of the chemical composition is not significant, although the emergent spectrum becomes slightly harder at lower A (Fig. 10, bottom panel).

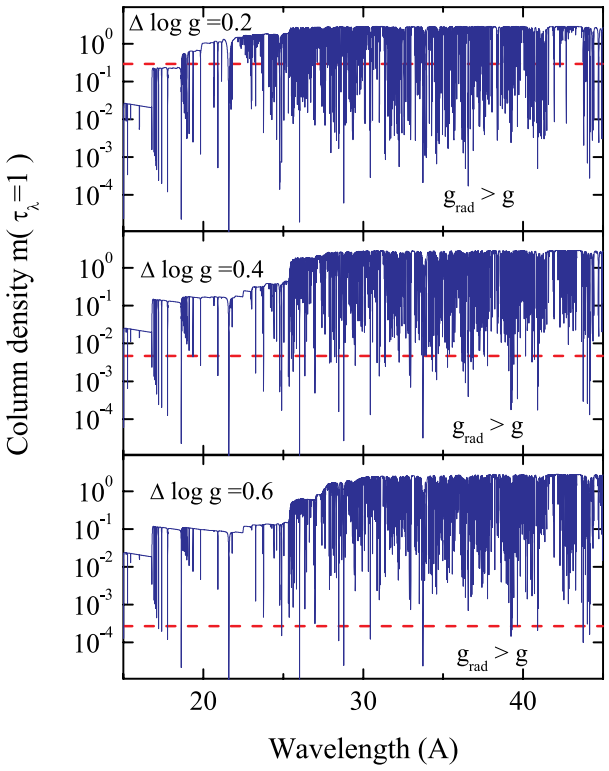

Fig. 8. Comparison of the emergent spectra formation depth ($m(\tau_\lambda = 1)$) with the wind dominating boundary (dashed red lines) for the model atmospheres with $T_{\rm eff}$ = 500 kK, A = 0.5, and three different $\Delta \log g$ = 0.2 (top), 0.4 (middle) and 0.6 (bottom panel). Atmospheric layers below the dashed red lines are dominated by the wind.

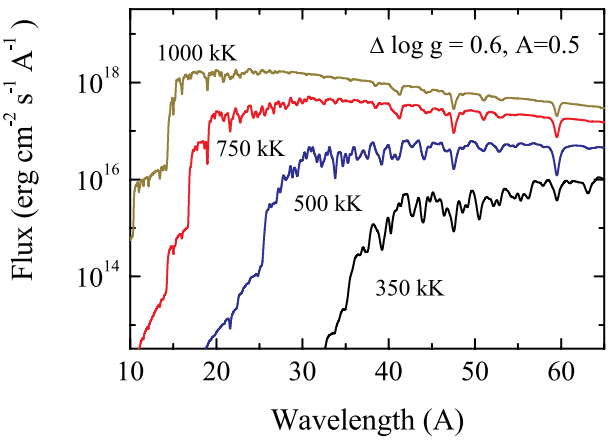

Fig. 9. Model spectra with various $T_{\rm eff}$ values, fixed $\Delta \log g$ = 0.6, and A = 0.5.

3.2. Application of the model to supersoft sources

The resulting model atmosphere grids cover large surface gravity and temperature ranges and can be used to estimate physical parameters of hot WDs, including supersoft X-ray sources. Before doing so it is important, however, to compare results obtained with our model grids with results that employed state-of-the-art models for some well-studied objects and to verify that our simplifying assumptions (i.e., LTE and hydrostatic approximation) are justified and that the deduced WD parameters are reasonable. To do that, we converted our model grids to XSPEC table model format and applied them to fit the spectra of two classical SSSs, namely, CAL 83 and RX J0513.9−6951.

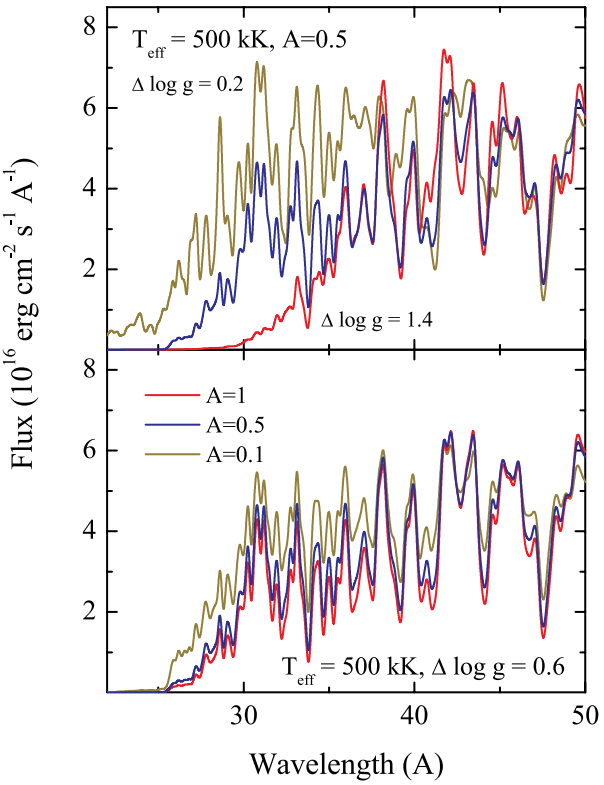

Fig. 10. Comparison of the fiducial model spectra ($T_{\rm eff}$ = 500 kK, $\Delta \log g$ = 0.6, A = 0.5) with the spectra computed for different $\Delta \log g$ (top) and A (bottom panel).

The spectra were obtained by the *Chandra* X-ray observatory using the High Resolution Camera (HRC-S) and the Low Energy Transmission Grating (LETG). They are publicly available in the Chandra Grating-Data Archive and Catalog[6] (TGCat, Huenemoerder et al. 2011); see also Table 1 for the observation log. To increase the signal-to-noise ratio (S/N) the positive and negative first-order spectra were co-added using the `combine_grating_spectra` task of the Chandra Interactive Analysis of Observations (CIAO, Fruscione et al. 2006; CIAO Development Team 2013) package. We also rebinned the spectra to at least 30 counts per bin in the considered 19–60 Å wavelength range.

For the source CAL 83, we also used the spectrum obtained by the *XMM-Newton* Reflection Grating Spectrometer (RGS, den Herder et al. 2001) instrument. It is available in the *XMM-Newton* Science Archive[7] (only the first-order spectrum was used). Table 1 shows the observation log.

For both sources, due to degeneracy in the WD mass, M, the standard gradient descent method of searching the statistics-minimum and the confidence interval does not allow us to reliably estimate parameter errors. Therefore, the Bayesian Markov chain Monte Carlo (MCMC) approach was used. In particular, we relied on the Bayesian X-ray Analysis (BXA, Buchner et al. 2014; Buchner 2016a) package, which allows for the use of the the nested sampling package UltraNest[8] (Buchner et al. 2014; Buchner 2019, 2021, 2016b) within XSPEC and allows us to derive the Bayesian evidence and posterior probability distributions. For visualisation of the posterior distributions the `corner`[9] package (Foreman-Mackey 2016, 2017) was used. The results of the modeling for both objects are discussed in the following.

It should be noted that for low-count spectra the usage of C-statistics (Cash 1979) instead of χ^2 is recommended; therefore, we used its Xspec implementation (`cstat`) as likelihood function to determine the best-fit parameters. The parameter uncertainties are derived from the 0.16th and 0.84th quantiles of the posterior distribution. As there is no convenient criterion of estimating the goodness-of-fit (like χ^2_ν) for `cstat`, we will give below the statistics value and the number of degrees of freedom.

3.2.1. CAL 83

The prototypical SSS CAL 83 was discovered by the *Einstein* observatory in the LMC (Long et al. 1981) and has since been observed by many X-ray observatories, including ROSAT (Greiner et al. 1991), *Beppo*SAX (Parmar et al. 1998), *XMM-Newton* (Paerels et al. 2001), *Chandra* (Lanz et al. 2005), and NICER (Orio et al. 2022). The X-ray flux of the source is not stable and it sometimes switches to the off-state (Kahabka 1997); see also Greiner & Di Stefano (2002) and the references therein. The X-ray pulsations with a period close to 67 s were also discovered by Odendaal et al. (2014) and this period is probably connected with the spin period of the WD. Recently, the available *XMM-Newton* X-ray spectra of the source were analysed by Stecchini et al. (2023).

The optical counterpart of the source is also known as a blue variable star with $V \approx 17$ mag (Cowley et al. 1984) and its optical spectrum contains prominent Balmer and He II emission lines (Crampton et al. 1987). A short review of the optical and ultraviolet (UV) observations of CAL 83 can be found in Skopal (2022). In particular, Gänsicke et al. (1998) determined the interstellar neutral hydrogen column density $N_{\rm H} = 6.5 \times 10^{20}$ cm^{-2}.

Model atmospheres of hot WDs were used to fit the soft X-ray spectra of CAL 83 observed by various X-ray observatories. Spectra of LTE model atmospheres computed by Heise et al. (1994) at a fixed $\log g = 9$ gave the effective temperature of the hot WD as 510.5^{+73}_{-7} kK using *Beppo*SAX observations (Parmar et al. 1998). To reproduce the ROSAT observations, the LTE models were computed by Ibragimov et al. (2003) for several $\log g$ values. However, the poor energy resolution of ROSAT observations did not provide the possibility to limit the surface gravity. The obtained $T_{\rm eff}$ varies from 504 ± 17 kK at $\log g = 8.0$ to 620 ± 25 kK at $\log g = 9.5$, assuming the interstellar column density is fixed at $N_{\rm H} = 6.33 \times 10^{20}$ cm^{-2}.

Non-LTE model atmospheres, computed using the publicly available code TLUSTY (Hubeny 1988) were used to fit the grating spectra obtained by *XMM-Newton* (Paerels et al. 2001) and *Chandra* (Lanz et al. 2005). In the first case, the obtained parameters were very approximate, $T_{\rm eff} \sim 520$ kK and $\log g \sim 8.5$. However, in the second paper, the model atmospheres were computed specifically for CAL 83 case and more reliable results were obtained (see Table 2).

Using our grid with the chemical composition typical for the LMC (A = 0.5), we fitted simultaneously *Chandra* and XMM spectra of CAL 83. A uniform prior distribution was set for the hydrogen column density, $N_{\rm H}$ (in the range (1–10) $\times 10^{20}$ cm^{-2}), effective temperature, $T_{\rm eff}$ (in the range 100–1000 kK), white dwarf mass, M (in range 0.3–1.4 $M_\odot$), and radius, R (in range (2–20) $\times 10^8$ cm) was used. We note that we set the strict upper limit for the WD mass. Another theoretical limitation is based on the fact that the WD radius must be greater than the cold WD radius at such a mass (see, e.g.,

[6] http://tgcat.mit.edu
[7] http://nxsa.esac.esa.int/nxsa-web
[8] https://johannesbuchner.github.io/UltraNest/
[9] https://corner.readthedocs.io/en/latest

Table 1. *Chandra* and *XMM-Newton* observations of selected sources.

Name	Instrument	ObsID	Exp. time[(a)]	Start time (UT)	End time (UT)	MJD (days)[(b)]
CAL 83	RGS	0123510101	45.1	2000 Apr. 23 07:34	2000 Apr. 23 20:09	51657.32
CAL 83	HRC-S/LETG	1900	34.2	2001 Aug. 15 16:03	2001 Aug. 16 02:10	52136.67
RX J0513.9−6951	HRC-S/LETG	5442	25.5	2005 Mar. 05 05:40	2005 Mar. 05 13:18	53493.24

Notes. [(a)]Exposure time in ks; [(b)]MJD of the start time.

Table 2. Parameters of the investigated SSSs.

Parameter	CAL 83 [(a)]	CAL 83 [(a)]	CAL 83 [(a)]	CAL 83 [(b)]	CAL 83 [(a)](bb)	RX J0513 [(a)]	RX J0513 [(c)]	RX J0513 [(a)](bb)
$N_{\rm H}$, 10^{20} cm^{-2}	6.5[(d)]	5.5[(d)]	$5.13\pm^{0.11}_{0.12}$	6.5 ± 1.0	5.13[(d)]	$5.40\pm^{0.09}_{0.10}$	$5.94\pm^{0.47}_{0.4}$	5.4[(d)]
$T_{\rm eff}$, kK	533 ± 2	556 ± 1	560 ± 2	550 ± 25	$540\pm^{3}_{2}$	$629\pm^{6}_{4}$	$594\pm^{10}_{7}$	684 ± 4
$M/M_\odot$	1.39 ± 0.01	$1.39\pm^{0.01}_{0.02}$	$1.29\pm^{0.06}_{0.07}$	1.3 ± 0.3		$1.33\pm^{0.05}_{0.07}$	1.0 ± 0.2	
R [(e)], 10^8 cm	7.8 ± 0.1	6.3 ± 0.1	6.0 ± 0.1	7.0 ± 0.7	8.6 ± 0.2	7.0 ± 0.2	10 ± 2	6.5 ± 0.1
L [(e)], 10^{37} erg s^{-1}	3.5 ± 0.1	2.7 ± 0.1	2.5 ± 0.1	3.5 ± 1.2	4.4 ± 0.2	5.4 ± 0.4	7.5 ± 2	6.5 ± 0.3
$\log g$	8.48 ± 0.02	8.66 ± 0.01	8.67 ± 0.03	8.5 ± 0.1		$8.56\pm^{0.03}_{0.04}$	$8.4\pm^{0.04}_{0.15}$	
$\Delta \log g$	0.75 ± 0.02	0.86 ± 0.01	0.86 ± 0.03	≈0.7		$0.55\pm^{0.03}_{0.04}$	$0.49\pm^{0.04}_{0.15}$	
cstat (d.o.f.)[(f)]	7005.47 (3807)	6823.29 (3807)	6811.52 (3806)		6438.81 (3808)	2114.14 (575)		2175.42 (577)

Notes. [(a)]Parameters obtained in this work; [(b)]parameters obtained by Lanz et al. (2005), [(c)]parameters obtained by Ibragimov et al. (2003); Suleimanov & Ibragimov (2003); [(d)]hydrogen column density $N_{\rm H}$ is fixed; [(e)]the distance to the LMC is assumed to be 50 kpc (Pietrzyński et al. 2019); [(f)]C-statistics and the number of degrees of freedom for the best fit found using Bayesian analysis.

Nauenberg 1972). Therefore, we further used the $M - R$ relation for cold WDs as an additional lower limit for a radius at the given WD mass.

The obtained posterior distribution of fit parameters is presented in Fig. 11 and Table 2. The determined absorption column density, $N_{\rm H} \sim 5.13 \times 10^{20}$ cm^{-2}, is slightly lower than the fiducial value $(6.5 \pm 1) \times 10^{20}$ cm^{-2} found previously by Gänsicke et al. (1998), who analyzed the UV spectra of CAL 83 and RX J0513.9−6951. Therefore, we performed the additional modelling assuming fixed $N_{\rm H} = 6.5 \times 10^{20}$ cm^{-2} and 5.5×10^{20} cm^{-2} (average column density in the direction of the LMC). These results are also presented in Table 2. It is clearly seen from the statistics value that the quality of these fits are worse, with the WD mass approaching the hard upper limit.

The comparison of the observed and model *Chandra* spectrum, corresponding to a model with $N_{\rm H}$ as a free parameter, is shown in Fig. 12, left panel. Despite using the LTE model atmospheres, the parameters found are very close to those found by Lanz et al. (2005; see Table 2). Our LTE atmosphere models thus yield the same SSS parameters with a similar accuracy as the non-LTE model spectra. However, our grid covers a much larger parameter space, which also means it may be applied to other sources.

The spectrum of CAL 83 observed by *Beppo*SAX was fitted with a blackbody model by Parmar et al. (1998) and the quality of the fit was even better compared to the non-LTE model atmospheres fits. Here, we also fitted the XMM and *Chandra* spectra with the blackbody model. Fitting with the free $N_{\rm H}$ yields larger values of $N_{\rm H}$ (≈13.3×10^{20} cm^{-2}) and a highly non-physically large WD radius (≈13.4×10^9 cm), but a lower $T_{\rm eff}$ (≈358 kK). In this case the

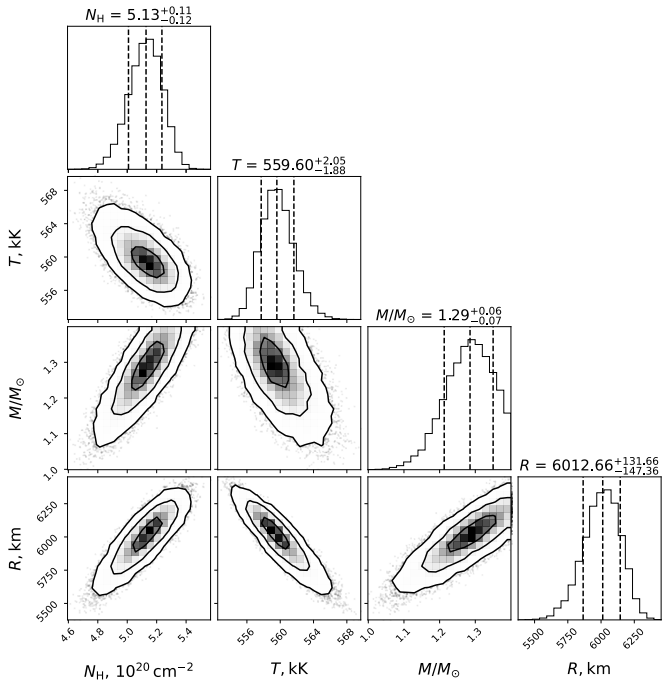

Fig. 11. Corner plot of the posterior distribution for parameters of CAL 83. The 2D contours correspond to 39.3%, 86.5%, and 98.9% confidence levels. The histograms show the normalized 1D distributions for a given parameter derived from the posterior samples. The best-fit parameter values are presented in Table 2. A Gaussian prior for the hydrogen column density N_H was used, with $\mu = 6.5 \times 10^{20}$ cm^{-2} and $\sigma = 1.0 \times 10^{20}$ cm^{-2}.

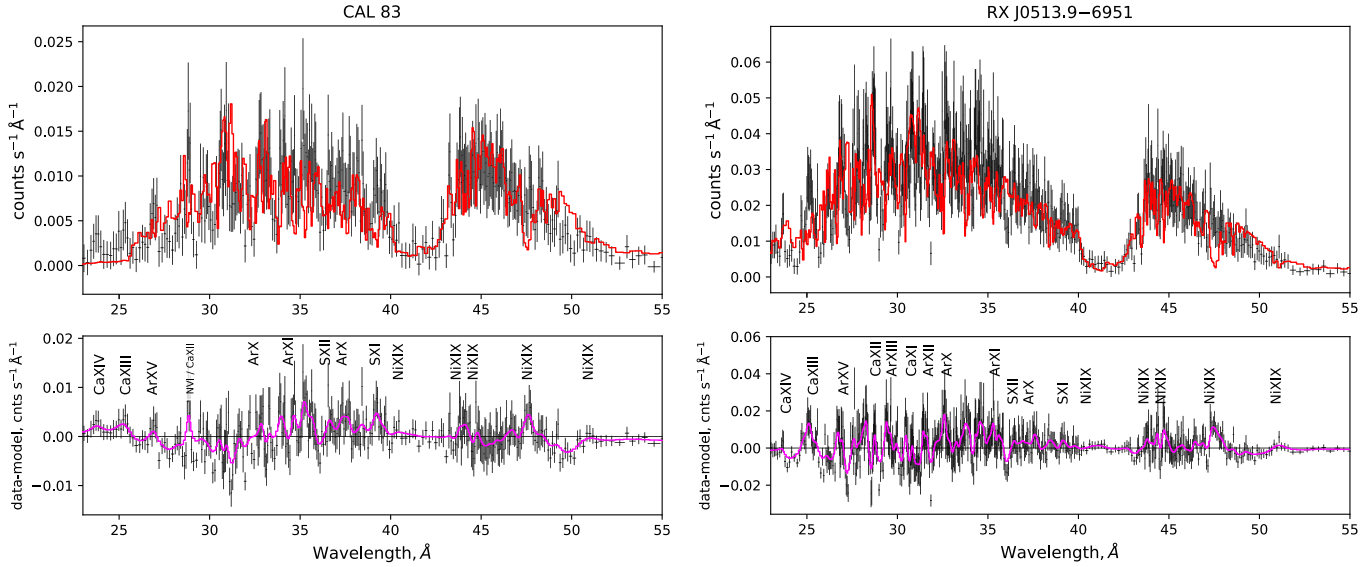

Fig. 12. Best fits of CAL 83 (left) and RX J0513.9−6951 (right) spectra (top). The observed spectra (*Chandra*, black curves) and the model fits (red curves) are shown. Residuals and the smoothed residuals (magenta curves) of the fits (bottom). Any possible identifications of the most prominent residual features as resonance lines of highly charged ions of some heavy elements are indicated. The best-fit parameters are presented in Table 2.

Table 3. Parameters of CAL 83 after fitting by the models with various chemical compositions.

Parameter	$A = 0.1$	$A = 1$	$A = 1$
$N_{\rm H}$, 10^{20} cm^{-2}	5.46 ± 0.08	3.0 ± 0.1	$5.1^{(a)}$
$T_{\rm eff}$, kK	508 ± 2	716 ± 6	586 ± 2
$M/M_\odot$	1.39 ± 0.01	1.35 ± 0.01	1.04 ± 0.01
$R^{(b)}$, 10^8 cm	8.01 ± 0.14	2.3 ± 0.07	5.17 ± 0.05
$L^{(b)}$, 10^{37} erg s^{-1}	3.04 ± 0.1	1.0 ± 0.1	2.25 ± 0.1
$\log g$	8.46 ± 0.02	9.53 ± 0.03	8.72 ± 0.02
$\Delta \log g$	0.82 ± 0.02	1.29 ± 0.03	0.83 ± 0.02
`cstat` (d.o.f.)$^{(c)}$	6820.23 (3806)	6172.02 (3806)	6995.9 (3807)

Notes. $^{(a)}$Hydrogen column density N_H is fixed; $^{(b)}$distance to the LMC is assumed to be 50 kpc (Pietrzyński et al. 2019); $^{(c)}C$-statistics and the degrees of freedom for the best fit found with Bayesian analysis.

derived bolometric luminosity exceeds the Eddington luminosity for a solar mass object, $\approx 2 \times 10^{39}$ erg s^{-1}. However, if we fix the interstellar absorption at a value found by the model atmosphere fitting, the best blackbody fit yields results that do not differ significantly from those of the best-fit model atmosphere (see Table 2). We note that formal fit quality is actually slightly better for the blackbody model, however, we emphasize that both models are statistically acceptable; moreover, the model atmosphere fits yield satisfactory results without the need to fix the hydrogen column density, unlike the blackbody fitting.

We also performed a fitting of the joint *Chandra* and *XMM-Newton* grating spectra using models with the solar ($A = 1$) chemical composition and models with heavy elements reduced by a factor of ten ($A = 0.1$). The results are presented in Table 3. The main conclusion is that there are remarkable differences between the best fits for the models with different chemical composition. The models with ten times reduced heavy element abundances ($A = 0.1$) produce the fit with a slightly decreased effective temperature, slightly increased photospheric radius and increased interstellar absorption. It was expected because the model spectra with $A = 0.1$ are slightly harder than those with $A = 0.5$ (see Fig. 10, bottom panel). Therefore, a model with a reduced temperature is needed to reproduce the observed spectrum. On the other hand, fitting using the models with solar heavy element abundances ($A = 1$) demonstrates more significant differences compared to the model spectra with $A = 0.5$ (see Table 3). Formally, the fit quality is better with $N_{\rm H}$ as a free parameter. However, the obtained $N_{\rm H}$ is too small, the temperature is too high and the radius is too small as well. In fact, the radius approached the low limit boundary for cold WD radius. Therefore, we fixed the interstellar absorption at the value obtained for $A = 0.5$. The resulting fit is much closer to the fit obtained for $A = 0.5$ (see Table 3) and it demonstrates a slightly increased temperature and a slightly decreased photospheric radius. All the fits ($A = 0.5$, free $N_{\rm H}$; $A = 0.1$, free $N_{\rm H}$; and $A = 1$, fixed $N_{\rm H}$) are not distinguishable from the statistical point of view.

3.2.2. RX J0513.9–6951

This recurrent SSS was discovered in ROSAT data by Schaeidt et al. (1993), and the corresponding optical counterpart was almost immediately identified by Pakull et al. (1993). The most interesting property of the source is its X-ray off-states, accompanied by optical brightening during these intervals (Southwell et al. 1996). It is most likely (see the cited work) that the source's luminosity during X-ray off-states is so high that it leads to a significant expansion of the envelope radius and the effective temperature drops, making the emergent radiation too soft to be observed in X-rays.

The X-ray spectra of RX J0513.9−6951 have been described by model atmosphere spectra only a couple of times. A low-resolution ROSAT spectrum was fitted with simple LTE model atmospheres (Ibragimov et al. 2003). Fitting a grating *Chandra*

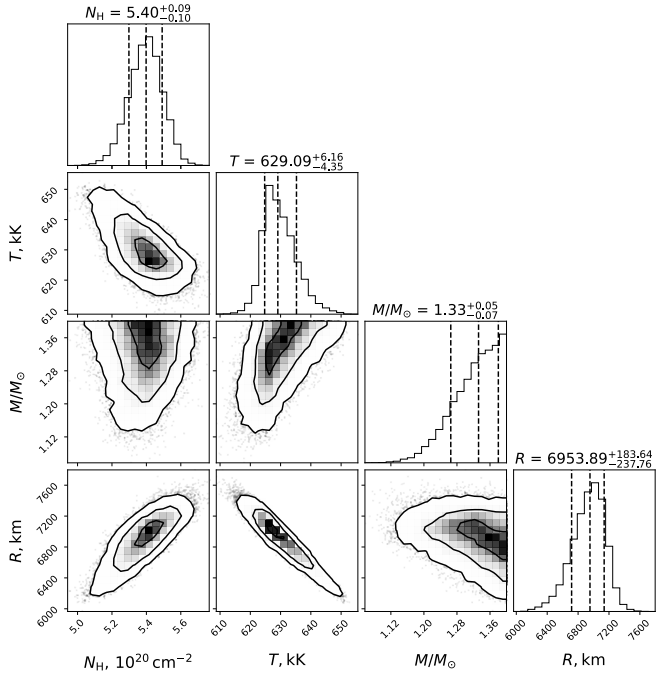

Fig. 13. Corner plot of the posterior distribution for parameters of RX J0513.9−6951. The 2D contours correspond to 39.3%, 86.5%, and 98.9% confidence levels. The histograms show the normalized 1D distributions for a given parameter derived from the posterior samples. The best-fit parameter values are presented in Table 2.

spectrum with the same models was less successful, and a two-component model was used to enhance the fit quality (Burwitz et al. 2007). Numerous *XMM-Newton* spectra obtained by the Resolution Grating Spectrometer (RGS) (McGowan et al. 2005) were not fitted with the model atmosphere spectra.

The results of fitting the *Chandra* spectrum with the new models described above are presented in Table 2 and the spectrum is shown in Fig. 12 (right panels). The corresponding posterior distribution of fit parameters is shown in Fig. 13. Similarly to CAL 83, we assumed uniform prior distributions for the hydrogen column density, N_H (range (1–10) $\times 10^{20}$ cm^{-2}); effective temperature, T_{eff} (range 100–1000 kK); the white dwarf mass, M (range 0.3–1.4 $M_\odot$); and radius R (range (2–20) $\times 10^8$ cm). It should be noted that the obtained hydrogen column density, N_H, posterior value is consistent with the result from Gänsicke et al. (1998); namely, (5.5 ± 1.0) $\times 10^{20}$ cm^{-2}. Also, the found values of T_{eff} and $\log g$ are close to those obtained from the ROSAT spectrum (Ibragimov et al. 2003), shown in Table 2.

We also fitted the spectrum of RX J0513.9−6951 with a blackbody model. The fit with a free N_H has the same features like the CAL 83 fit: N_H value and WD radius are significantly larger than in the model atmosphere fit, and the blackbody temperature is much lower. The fit with the fixed N_H also yields results that are relatively close to those of the model atmosphere fit (see Table 2). However, comparing the blackbody fit with the fixed N_H and the model atmosphere fit with the free N_H using the Bayes factor showed that the spectrum is slightly better described by the model atmosphere spectra than by the blackbody.

3.2.3. Emission component importance

It is widely known that the spectra of highly inclined SSSs are dominated by emission lines (see, e.g., Ness et al. 2013). Possibly, the same or similar emission lines have to exist in the spectra of CAL 83 and RX J0513.9−6951. For example, three emission features between 24 and 28 Å are seen in the observed spectra of both sources. Most probably they are resonance lines of Ca XIV (~24 Å), Ca XIII (~25.2 Å), and Ar XV (~26.8 Å). Observed flux excesses, visible at longer wavelengths, may also represent emission lines of highly charged ions of the same or similar elements. We assume that these emission line components are thermal emission of the line-driven winds from the hot WD surface. The presence of the emission component affects the accuracy of spectrum fitting and it has to be included in further modeling.

The lower panels in Fig. 12 show the residuals between the observed spectra and the hot WD model atmosphere spectra, with the parameters listed in Table 2. The most prominent emission features can be identified with the resonance lines of highly charged ions of heavy elements. The list of identified lines is presented in Table 4. The line identification was made using CHIANTI line database (Dere et al. 1997).

We note, however, that the significance of the interpreted emission lines is not high enough. Formally, we can improve the quality of the fits by including a few (5–6) emission lines. This procedure formally reduces the reduced χ^2 (by ~0.2), but does not significantly change the WD atmosphere parameters.

4. Discussion

Our spectral fitting showed that the WD masses in the investigated sources are high (>1.2 $M_\odot$) and tend to the maximum possible values for WDs. However, the derived radii are significantly larger than radii of cold WDs with these masses. It is, in fact, expected because radii of single WDs with hydrogen or helium envelopes and finite temperatures are larger than cold WD radii (see, e.g., Fontaine et al. 2001). On the other hand, the difference in the radius between the cold WDs and the WDs with the hot envelopes is minimal for high-mass WDs.

The envelope temperatures with thermonuclear burning on the WD surface in SSSs are, however, significantly higher than those of thick envelopes of isolated WDs. Therefore, we expect that the photospheric radius of a hot WD in SSSs could be significantly larger than the radius of a cold WD with the same mass, and comparison with the computed models is potentially important. Models of WD envelopes with hydrogen thermonuclear burning have been computed by several groups (see, e.g., Nomoto et al. 2007; Wolf et al. 2013). The numerical dependencies of the WD radii on the surface effective temperatures for a few WD masses are presented by Nomoto et al. (2007). We plotted these dependencies in the T_{eff}–$\log g$ plane (see Fig. 14) together with the positions of CAL 83 and RX J0513.9−6951. We took the fits obtained for free N_H. It is clearly seen that the WD masses in the SSSs derived from the model dependences are less than we obtained from the spectral fitting, and correspond to about 1.1–1.15 $M_\odot$ for both sources.

Another theoretical constraint can be obtained from the cooling tracks in the $\log T_{eff}$–$\log L/L_\odot$ plane, where L is a luminosity. Such tracks computed (among others) by Iben (1982) are presented in Fig. 15 (top panel; also see Fig. 2 in the cited paper), with the added positions of CAL 83 and RX J0513.9−6951.

The positions of the SSSs correspond to almost the same WD masses, 1.15–1.2 $M_\odot$. We also compared the sources' positions on this plane with the model predictions by Wolf et al. (2013; Fig. 15, bottom panel). In this case, the positions correspond to the cooling tracks with a slightly lower mass, namely, 1.05–1.1 $M_\odot$.

Table 4. Lines likely corresponding to observed emission features.

Ion	λ (Å)	gf	$E_{\rm low}$ (eV)
Ca XIV	24.09	2.39	0.00
	24.13	3.58	0.00
Ca XIII	25.53	2.35	0.00
Ar XV	26.62	2.91	0.00
	26.66	2.24	0.00
	26.71	3.93	0.00
Ca XII	28.48	1.39	0.00
N VI	28.79	0.66	0.00
Ca XII	28.86	0.76	3.73
Ar XIII	29.32	1.12	2.72
	29.32	0.91	0.00
	29.35	2.04	1.22
	29.37	3.81	2.72
Ca XI	30.45	2.34	0.00
	30.45	2.68	0.00
Ar XII	31.35	2.32	0.00
	31.39	3.47	0.00
Ar X	32.45	0.14	0.00
	32.61	0.44	0.00
Ar XI	34.10	0.81	0.00
	34.24	1.80	0.00
	34.52	1.12	1.79
Ar XI	35.37	1.08	0.00
S XII	36.56	4.10	1.63
Ar X	37.43	2.61	0.00
	37.48	1.89	0.00
	38.23	1.46	0.00
S XI	39.24	2.73	1.54
	39.24	2.00	0.00
	39.30	4.10	0.65
	39.32	3.59	1.54
C V	40.27	0.65	0.00
Ni XIX	40.60	3.08	0.00
Ni XIX	43.79	1.75	0.00
	44.73	3.83	0.00
S IX	47.43	1.89	0.00
Ni XIX	47.43	8.38	0.00
	47.52	8.99	0.00
	47.55	3.83	0.00
	47.65	5.91	0.00
	47.73	5.97	0.00
Ni XIX	51.09	5.01	0.00

Notes. Lines probably corresponding to one feature are separated by horizontal lines. The wavelengths, gf-factors, and the excitation energy of the lower levels $E_{\rm low}$ are also presented. Some close lines of the same ion and the low energy level have been merged.

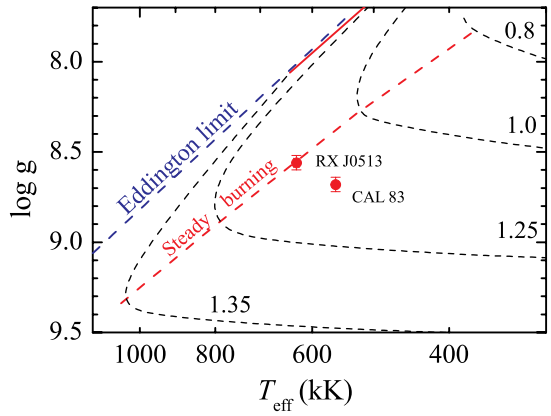

Fig. 14. Positions of the investigated SSSs in the $T_{\rm eff}$–log g plane. Model dependencies for various WD masses (Nomoto et al. 2007) are shown by black dashed curves with indicated WD masses (in solar masses). The boundaries of the stable thermonuclear burning band are shown by the solid (upper boundary) and the dashed (lower boundary) red lines. The Eddington limit for solar H/He abundances is shown by the blue dashed line.

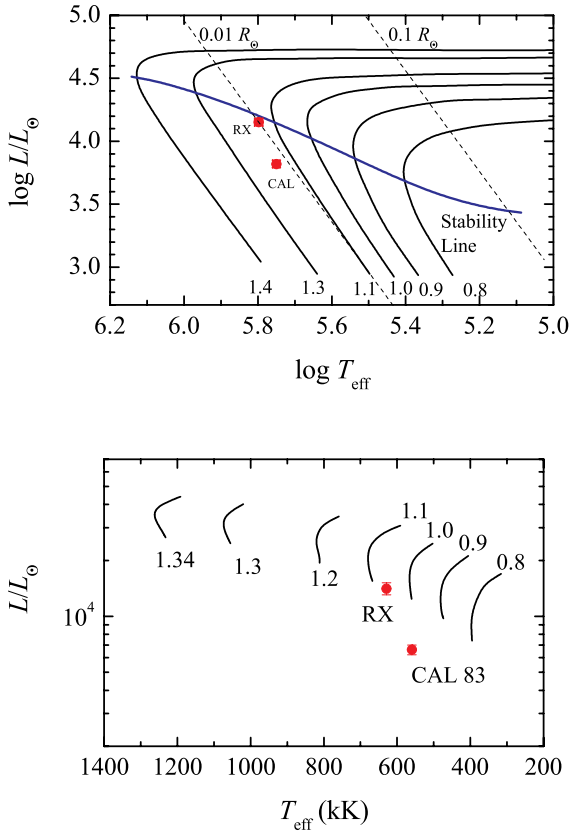

Fig. 15. Positions of the investigated SSSs in the $T_{\rm eff}$–$L/L_\odot$ planes. Top panel: Model dependencies for various WD masses were taken from Iben (1982). Steady-state thermonuclear burning on WD surfaces is possible above the stability line only. Bottom panel: Model dependencies were taken from Wolf et al. (2013). Only the model curves with steady-state thermonuclear burning are shown.

These results confirm a conclusion made previously (Suleimanov & Ibragimov 2003), which posits that RX J0513.9−6951 lies in the steady-state thermonuclear burning band, as also seen in Fig. 5 in Ibragimov et al. (2003). Therefore, the off-states of this SSS are most probably connected with the photospheric radius expansion during periods of increased mass-accretion rates. At the same time, the luminosity of the hot WD in CAL 83 is significantly lower than the predicted one for the steady state burning band. It means that this source lies below the stable thermonuclear burning band, as found earlier (Suleimanov & Ibragimov 2003). Therefore, thermonuclear burning most likely arises episodically and the X-ray

off-states are connected with the cessation of thermonuclear burning (Kahabka 1995, 1998). In the cited work, there is a statement that a relatively short off-states duration in CAL 83 (<100 days) can exist if the WD is quite massive, $M > 1.2\,M_\odot$. Our estimation of the WD mass in CAL 83 derived from the spectral fit is in agreement with this condition.

5. Summary

In this paper, we present a new extended set of hot WD model spectra. The corresponding model atmospheres were computed under LTE and hydrostatic equilibrium assumptions. The list of spectral lines presented by CHIANTI collaboration was used. The novel thing in contrast with our previous computations is taking into account the photoionization from the excited atomic levels. The set was computed for three chemical compositions. The solar hydrogen-helium mix was used for all models, but the heavy element abundances were taken to be equal to the solar one ($A = 1$), half of the solar ($A = 0.5$), and one-tenth of the solar ($A = 0.1$). These abundances correspond to the Milky Way disc, the LMC, and the SMC. The grid covers $T_{\rm eff}$ = 100–1000 kK in steps of 25 kK, and eight values of surface gravity, measured from the limited possible surface gravity $g_{\rm Edd}$, $\Delta \log g = \log g – \log g_{\rm Edd} = 0.1, 0.2, 0.4, 0.6, 1.0, 1.4, 1.8$, and 2.2. This model spectra set is designed to fit the observed soft X-ray spectra of SSSs and it was implemented into XSPEC[10].

We used the calculated model grid to interpret the grating spectra of two bright SSSs in the LMC, CAL 83 (*Chandra*/LETGS and *XMM-Newton*/RGS spectra), and RX J0513.9−6951 (one *Chandra*/LETGS spectrum). We found that best-fit WD effective temperature values are in agreement with the values obtained in previous investigations. The values of $T_{\rm eff}$ and $\log g$ obtained for CAL 83 using detailed non-LTE model atmospheres are also in good agreement with our results. Therefore, we conclude that our simplified LTE model atmospheres can be used for the analysis of the X-ray spectra of SSSs with good results despite their limitations. In fact, there are no publicly available sets of non-hydrostatic model atmospheres and non-LTE atmosphere models were computed only in a narrow range of input parameters, so the presented model set is actually the first of its kind to be released to general community.

The WD parameters found for the investigated SSSs confirm that RX J0513.9−6951 lies in the stable nuclear burning strip, while CAL 83 lies below this strip, and thermonuclear burning on the WD surface is episodic. Theoretically, a relatively short observed duration between burning episodes is possible if the WD is massive enough, $M > 1.2\,M_\odot$. Using published model $T_{\rm eff}$–$\log g$ and $\log T_{\rm eff}$–$\log L/L_\odot$ dependencies, we estimated the WD mass in CAL 83 to be confined within 1.05–1.2 $M_\odot$, which is in marginal agreement with this theoretical prediction. The WD mass estimation for RX J0513.9−6951 gives a more narrow range, 1.1–1.2 $M_\odot$.

A notable contradiction between the WD masses formally obtained from the spectral fits and from the sources' positions on the theoretical $T_{\rm eff}$–$\log g$ and $T_{\rm eff}$–$\log L/L_\odot$ dependencies can be pointed out. The masses from the spectral fits are high ($\approx$1.29 $M_\odot$ for CAL 83) and poorly constrained, and tend to the maximum possible WD mass 1.4 $M_\odot$ for RX J0513.9−6951. On the contrary, the masses from the model tracks lie within 1.05–1.2 $M_\odot$.

Although we could also suggest that the model tracks need to be revised, the simplest solution is that the spectral fits provide poor accuracy in determining WD masses. The main reason is that we can observe only a relatively narrow soft X-ray part of the general spectral energy distribution of SSSs. Moreover, the soft X-ray part of the spectra is heavily influenced by interstellar absorption. It means that we had to introduce limitation on the $N_{\rm H}$ value from optical and UV observations, and set the limit of the WD radius, which cannot be smaller than the radius of a cold WD with a given mass. Perhaps, the development of the observations and the models will allow us to obtain basic SSS parameters, including the chemical composition, only from soft X-ray observations without any additional conditions. However, this is a matter that will be tackled in the distant future. Finally, we conclude that the presented model spectra set could be useful for interpreting both the existing grating spectra of SSS, obtained by *Chandra* and *XMM-Newton*, and new observations of SSSs by eROSITA.

Acknowledgements. We express our deep gratitude to the referee for their comments, which significantly improved this article. VFS and AST thank the Deutsche Forschungsgemeinschaft (DFG) for financial support (grants WE 1312/59-1 and WE 1312/56-1, respectively).

[10] https://github.com/HEASARC/xspec_localmodels/tree/master/sss_atm

References

Arnaud, K. A. 1996, in Astronomical Society of the Pacific Conference Series, 101, Astronomical Data Analysis Software and Systems V, eds. G. H. Jacoby, & J. Barnes, 17
Arnaud, K., Dorman, B., & Gordon, C. 1999, XSPEC: An X-ray spectral fitting package, Astrophysics Source Code Library [record ascl:9910.005]
Buchner, J. 2016a, BXA: Bayesian X-ray Analysis, Astrophysics Source Code Library [record ascl:1610.011]
Buchner, J. 2016b, UltraNest: Pythonic Nested Sampling Development Framework and UltraNest, Astrophysics Source Code Library [record ascl:1611.001]
Buchner, J. 2019, PASP, 131, 108005
Buchner, J. 2021, J. Open Source Softw., 6, 3001
Buchner, J., Georgakakis, A., Nandra, K., et al. 2014, A&A, 564, A125
Burwitz, V., Reinsch, K., Greiner, J., et al. 2007, Adv. Space Res., 40, 1294
Carrera, R., Gallart, C., Aparicio, A., et al. 2008, AJ, 136, 1039
Cash, W. 1979, ApJ, 228, 939
CIAO Development Team 2013, CIAO: Chandra Interactive Analysis of Observations, Astrophysics Source Code Library [record ascl:1311.006]
Cowley, C. R. 1971, The Observatory, 91, 139
Cowley, A. P., Crampton, D., Hutchings, J. B., et al. 1984, ApJ, 286, 196
Crampton, D., Cowley, A. P., Hutchings, J. B., et al. 1987, ApJ, 321, 745
Del Zanna, G., Dere, K. P., Young, P. R., & Landi, E. 2021, ApJ, 909, 38
den Herder, J. W., Brinkman, A. C., Kahn, S. M., et al. 2001, A&A, 365, L7
Dere, K. P., Landi, E., Mason, H. E., Monsignori Fossi, B. C., & Young, P. R. 1997, A&AS, 125, 149
Fontaine, G., Brassard, P., & Bergeron, P. 2001, PASP, 113, 409
Foreman-Mackey, D. 2016, J. Open Source Softw., 1, 24
Foreman-Mackey, D. 2017, corner.py: Corner plots, Astrophysics Source Code Library [record ascl:1702.002]
Fruscione, A., McDowell, J. C., Allen, G. E., et al. 2006, SPIE Conf. Ser., 6270, 62701V
Gänsicke, B. T., van Teeseling, A., Beuermann, K., & de Martino, D. 1998, A&A, 333, 163
Greiner, J., & Di Stefano, R. 2002, A&A, 387, 944
Greiner, J., Hasinger, G., & Kahabka, P. 1991, A&A, 246, L17
Griem, H. R. 1960, ApJ, 132, 883
Griem, H. R. 1967, ApJ, 148, 547
Hartmann, H. W., & Heise, J. 1997, A&A, 322, 591
Hartmann, H. W., Heise, J., Kahabka, P., Motch, C., & Parmar, A. N. 1999, A&A, 346, 125
Hauschildt, P. H., Baron, E., & Allard, F. 1997, ApJ, 483, 390
Heise, J., van Teeseling, A., & Kahabka, P. 1994, A&A, 288, L45
Hubeny, I. 1988, Comp. Phys. Commun., 52, 103
Hubeny, I., Hummer, D. G., & Lanz, T. 1994, A&A, 282, 151
Huenemoerder, D. P., Mitschang, A., Dewey, D., et al. 2011, AJ, 141, 129
Hummer, D. G., & Mihalas, D. 1988, ApJ, 331, 794

Iben, I., J. 1982, ApJ, 259, 244
Ibragimov, A. A., Suleimanov, V. F., Vikhlinin, A., & Sakhibullin, N. A. 2003, Astron. Rep., 47, 186
Kahabka, P. 1995, A&A, 304, 227
Kahabka, P. 1997, in Astronomical Society of the Pacific Conference Series, 121, IAU Colloq. 163: Accretion Phenomena and Related Outflows, eds. D. T. Wickramasinghe, G. V. Bicknell, & L. Ferrario, 730
Kahabka, P. 1998, A&A, 331, 328
Kahabka, P., & van den Heuvel, E. P. J. 1997, ARA&A, 35, 69
Kahabka, P., Hartmann, H. W., Parmar, A. N., & Negueruela, I. 1999, A&A, 347, L43
Karzas, W. J., & Latter, R. 1961, ApJS, 6, 167
König, O., Wilms, J., Arcodia, R., et al. 2022, Nature, 605, 248
Kurucz, R. L. 1970, SAO Spec. Rep., 309
Kurucz, R. 1993a, ATLAS9 Stellar Atmosphere Programs and 2 km/s Grid, Kurucz CD-ROM No. 13, Cambridge, 13
Kurucz, R. L. 1993b, VizieR Online Data Catalog: VI/39
Lanz, T., Telis, G. A., Audard, M., et al. 2005, ApJ, 619, 517
Long, K. S., Helfand, D. J., & Grabelsky, D. A. 1981, ApJ, 248, 925
McGowan, K. E., Charles, P. A., Blustin, A. J., et al. 2005, MNRAS, 364, 462
Mihalas, D. 1978, Stellar Atmospheres (San Francisco: W.H. Freeman)
Nauenberg, M. 1972, ApJ, 175, 417
Ness, J. U. 2010, Astron. Nachr., 331, 179
Ness, J.-U. 2020, Adv. Space Res., 66, 1202
Ness, J. U., Starrfield, S., Burwitz, V., et al. 2003, ApJ, 594, L127
Ness, J. U., Osborne, J. P., Henze, M., et al. 2013, A&A, 559, A50
Nomoto, K., Saio, H., Kato, M., & Hachisu, I. 2007, ApJ, 663, 1269
Odendaal, A., Meintjes, P. J., Charles, P. A., & Rajoelimanana, A. F. 2014, MNRAS, 437, 2948
Orio, M., Covington, J., & Ögelman, H. 2001, A&A, 373, 542
Orio, M., Gendreau, K., Giese, M., et al. 2022, ApJ, 932, 45
Paerels, F., Rasmussen, A. P., Hartmann, H. W., et al. 2001, A&A, 365, L308
Pakull, M. W., Motch, C., Bianchi, L., et al. 1993, A&A, 278, L39
Parmar, A. N., Kahabka, P., Hartmann, H. W., Heise, J., & Taylor, B. G. 1998, A&A, 332, 199
Pietrzyński, G., Graczyk, D., Gallenne, A., et al. 2019, Nature, 567, 200
Rauch, T. 2003, A&A, 403, 709
Rauch, T., & Werner, K. 2010, Astron. Nachr., 331, 146
Rauch, T., Orio, M., Gonzales-Riestra, R., et al. 2010, ApJ, 717, 363
Rolleston, W. R. J., Trundle, C., & Dufton, P. L. 2002, A&A, 396, 53
Schaeidt, S., Hasinger, G., & Truemper, J. 1993, A&A, 270, L9
Schwarz, G. J., Ness, J.-U., Osborne, J. P., et al. 2011, ApJS, 197, 31
Seaton, M. J., Yan, Y., Mihalas, D., & Pradhan, A. K. 1994, MNRAS, 266, 805
Skopal, A. 2022, AJ, 164, 145
Southwell, K. A., Livio, M., Charles, P. A., O'Donoghue, D., & Sutherland, W. J. 1996, ApJ, 470, 1065
Stecchini, P. E., Perez Diaz, M., D'Amico, F., & Jablonski, F. 2023, MNRAS, 522, 3472
Suleimanov, V. F., & Ibragimov, A. A. 2003, Astron. Rep., 47, 197
Suleimanov, V. F., Mauche, C. W., Zhuchkov, R. Y., & Werner, K. 2013, in Astronomical Society of the Pacific Conference Series, 469, 18th European White Dwarf Workshop., eds. J. Krzesiński, G. Stachowski, P. Moskalik, & K. Bajan, 349
Suleimanov, V., Hertfelder, M., Werner, K., & Kley, W. 2014a, A&A, 571, A55
Suleimanov, V. F., Klochkov, D., Pavlov, G. G., & Werner, K. 2014b, ApJS, 210, 13
Sutherland, R. S. 1998, MNRAS, 300, 321
Swartz, D. A., Ghosh, K. K., Suleimanov, V., Tennant, A. F., & Wu, K. 2002, ApJ, 574, 382
Trümper, J., Hasinger, G., Aschenbach, B., et al. 1991, Nature, 349, 579
van den Heuvel, E. P. J., Bhattacharya, D., Nomoto, K., & Rappaport, S. A. 1992, A&A, 262, 97
van Rossum, D. R. 2012, ApJ, 756, 43
van Rossum, D. R., & Ness, J. U. 2010, Astron. Nachr., 331, 175
Verner, D. A., Ferland, G. J., Korista, K. T., & Yakovlev, D. G. 1996, ApJ, 465, 487
Werner, K., Deetjen, J. L., Dreizler, S., et al. 2003, in Astronomical Society of the Pacific Conference Series, 288, Stellar Atmosphere Modeling, eds. I. Hubeny, D. Mihalas, & K. Werner, 31
Wolf, W. M., Bildsten, L., Brooks, J., & Paxton, B. 2013, ApJ, 777, 136

Paper II

II

A. Tavleev, L. Ducci, V. Suleimanov, C. Maitra, K. Werner, A. Santangelo, V. Doroshenko

"Soft X-ray emission from the classical nova AT 2018bej"

Astronomy & Astrophysics, 2024, 689, A335

A&A, 689, A335 (2024)
https://doi.org/10.1051/0004-6361/202451195

Astronomy & Astrophysics

Soft X-ray emission from the classical nova AT 2018bej

A. Tavleev[1,⋆], L. Ducci[1,2], V. F. Suleimanov[1], C. Maitra[3], K. Werner[1], A. Santangelo[1], and V. Doroshenko[1]

[1] Institut für Astronomie und Astrophysik, Kepler Center for Astro and Particle Physics, Universität Tübingen, Sand 1, 72076 Tübingen, Germany
[2] ISDC Data Center for Astrophysics, Université de Genève, 16 chemin d'Écogia, 1290 Versoix, Switzerland
[3] Max-Planck-Institut für extraterrestrische Physik, Gießenbachstraße 1, 85748 Garching, Germany

Received 20 June 2024 / Accepted 19 August 2024

ABSTRACT

Context. Classical novae are known to demonstrate a supersoft X-ray source (SSS) state following outbursts. This state is associated with residual thermonuclear burning on the white dwarf (WD) surface. During its all-sky survey (eRASS1), the eROSITA telescope on board the Spectrum-Roentgen-Gamma observatory discovered a bright new SSS, whose position is consistent with the known classical nova AT 2018bej in the Large Magellanic Cloud. There were two eROSITA spectra obtained during the eRASS1 and eRASS2 monitoring epochs and one *XMM-Newton* grating spectrum close to the eRASS1 epoch.
Aims. We aim to describe the eROSITA and follow-up *XMM-Newton* spectra of AT 2018bej with our local thermodynamic equilibrium (LTE) atmosphere models. We focussed on the evolution of the hot WD properties between the eRASS1 and eRASS2 epochs, especially with respect to the change in carbon abundance.
Methods. A grid of LTE model atmosphere spectra was calculated for different values of the effective temperature (from $T_{\rm eff}$ = 525 to 700 kK in steps of 25 kK), surface gravity (six values), and chemical composition, assuming approximately equal hydrogen and helium number fractions, and five different values of carbon and nitrogen abundances.
Results. Both eRASS1 and XMM 0.3−0.6 keV spectral analyses yield a temperature of the WD of $T_{\rm eff}\sim$ 600 kK and a WD radius of 8000−8700 km. A simultaneous fitting of the eROSITA spectra for two epochs (eRASS1 and eRASS2) with a common WD mass parameter demonstrates a decrease in $T_{\rm eff}$, accompanied by an increase in the WD radius and a decrease in the carbon abundance. However, these changes are marginal and remain within the errors. The derived WD mass is estimated to be 1.05−1.15 $M_{\odot}$.
Conclusions. We traced a minor evolution of the source on a half-year timescale accompanied by a decrease in the carbon abundance and concluded that LTE model atmospheres can be used to analyse the available X-ray spectra of classical novae during their SSS state.

Key words. novae, cataclysmic variables – white dwarfs – X-rays: individuals: AT 2018bej

1. Introduction

A new X-ray source was discovered by eROSITA during the first part of its all-sky survey, whose position is consistent with the known classical nova (CN) AT 2018bej in the Large Magellanic Cloud (LMC, Ducci et al. 2020; Chomiuk et al. 2018). The X-ray spectrum was thermal with low temperature of ∼30 eV and high luminosity $>10^{37}$ erg s^{-1}. These properties led to conclusion that the super-soft source (SSS) phase of CNe was observed for this nova (Ducci et al. 2020).

A CN may undergo the SSS phase during outbursts (Hachisu & Kato 2006). The ejected envelope becomes transparent some time after the outburst maximum and the hot nuclear burning shell, producing the soft X-ray emission, can be observed (Bode & Evans 2008). This picture is confirmed both by calculations (Starrfield et al. 2004; Soraisam et al. 2016) and observations (see e.g. Kahabka et al. 1999; Orio et al. 2001; Ness et al. 2003; Henze et al. 2014).

The SSS phase was named after the classical supersoft sources, which are a sub-class of cataclysmic variable (CV) stars with high mass-accretion rate of $\sim10^{-7}\,M_{\odot}$ yr^{-1} and (quasi-)steady state thermonuclear burning on the white dwarf (WD) surface (van den Heuvel et al. 1992; Rappaport et al. 1994). Furthermore, CVs are close binaries, consisting of a WD as a primary star and a main sequence or red giant companion that fills its Roche lobe. As a result, the matter flows from the companion to the WD (with the possible formation of an accretion disc) and CNe originate from thermonuclear explosions on WD surfaces in such objects (Starrfield et al. 2016). Namely, the thermonuclear explosion takes place in the accumulated hydrogen-rich material on the surface of the WD, which leads to the expansion of the envelope and to subsequent rise in the brightness of the system, as well as to mass ejection from the binary (see Bode & Evans 2008, for a review).

The first SSSs were discovered in the Magellanic Clouds by the *Einstein* observatory (Long et al. 1981; Seward & Mitchell 1981) and then were treated as a new class of X-ray objects during the ROSAT observations (Trümper et al. 1991). They are characterised by very soft thermal X-ray spectra with blackbody temperatures of about 15−80 eV (150−900 kK) and high luminosities $\sim10^{36}-10^{38}$ erg/s, comparable with the Eddington luminosity of a solar mass object (Kahabka & van den Heuvel 1997; Greiner 2000). Currently, more than 100 SSSs are known in ∼20 external galaxies, the Magellanic Clouds, and our Galaxy (Greiner 2000; Kahabka 2006; Maitra & Haberl 2022).

The interpretation of SSS spectra is challenging. Low-resolution spectra can be often reproduced by a blackbody fit, but this model is not physically accurate. In general, blackbody fitting overestimates the interstellar neutral hydrogen column density, $N_{\rm H}$, and underestimates temperature, resulting in an

⋆ Corresponding author; tavleev@astro.uni-tuebingen.de

overestimated luminosity (see e.g. Greiner et al. 1991; Heise et al. 1994). High-resolution spectra of SSSs are much more complex, with plenty of emission and absorption lines (with the clear role of orientation effects, see Ness et al. 2013).

Physically motivated models, which potentially can describe the observed SSS spectra are the theoretical spectra of hot WD atmospheres. Heise et al. (1994) constructed the first model atmospheres of hot WDs for explaining the SSS X-ray spectra. These models were computed under the assumption of local thermodynamic equilibrium (LTE). However, deviations from this assumption potentially can be significant at high temperature. Therefore, various authors tried to use the model spectra of hot WD atmospheres computed without LTE assumption (non-LTE, NLTE model atmospheres). In particular, the TLUSTY (Hubeny & Lanz 1995, 2011) code was used to model hot WD atmospheres and corresponding model spectra were used for fitting the BeppoSAX and ROSAT spectra of various SSSs (e.g. Hartmann & Heise 1996, 1997; Hartmann et al. 1999; Parmar et al. 1997, 1998). Lanz et al. (2005) performed a detailed NLTE model atmosphere analysis of *Chandra* and *XMM-Newton* spectroscopy of the SSS CAL 83 in the LMC.

The multi-purpose model-atmosphere NLTE code PHOENIX (Hauschildt & Baron 1999; Baron et al. 2010), modified to calculate model atmospheres for the late X-ray phase of CNe, was used to fit the *Chandra* observations of nova V4743 Sgr (Petz et al. 2005). The WD atmosphere was 1D spherical and was approximated by an expanding, but stationary in time, structure. The composition was assumed to be solar, leading to some uncertainties in the fit. Due to the strong evidence for expansion in the SSS spectra of novae (Ness 2010), a new version of PHOENIX was developed to account for this wind-type ejecta expansion (van Rossum & Ness 2010; van Rossum 2012). Also, a four-dimensional (4D) grid of wind-type model spectra was introduced for $T_{\rm eff}$ = 450−750 kK, seven values of $\log g$, four values of the wind asymptotic velocity, v_∞, and three values of mass-loss rate, $\dot{M}$, while the chemical composition was set to solar (van Rossum 2012).

The Tübingen NLTE Model-Atmosphere Package (TMAP, Rauch 2003; Werner et al. 2003, 2012) model atmospheres were successfully used for spectral analysis of hot, compact stars (see Rauch & Werner 2010, for a brief summary). Using this code, Rauch et al. (2010) performed a NLTE spectral analysis of the nova V4743 Sgr in SSS phase. While the model was plane-parallel and static (in contrast with Petz et al. 2005), the chemical composition was more realistic. Additionally, the grid of models was calculated for H-Ni with solar abundance ratios within $T_{\rm eff}$ = 450−1050 kK and a fixed surface gravity of $\log g = 9$ (see refs. in Rauch et al. 2010).

The challenging factor in describing spectra of SSSs is the unknown composition of the WD atmosphere, which should reflect both the composition of the accreted material and the nucleosynthesis products. Therefore, a mixture of stellar and CNO-cycle processed material is expected. The resulting deficiency of hydrogen and enhancement of helium abundances, as well as the deficiency of carbon and the enhancement of nitrogen and oxygen abundances, have an impact on the strength of absorption lines and the general continuum shape (e.g. Rauch 2003; Rauch et al. 2010).

Nevertheless, LTE model atmospheres were used by Ibragimov et al. (2003) and Suleimanov & Ibragimov (2003) for the analysis of ROSAT spectra of 11 SSSs. They used a modified version of Kurucz's ATLAS code. This models were also used to fit spectra of other SSSs (Burwitz et al. 2007; Swartz et al. 2002).

Recently Suleimanov et al. (2024) further refined the LTE approach, including a more extensive set of spectral lines and photoionisation opacities from the excited levels of heavy element ions. They successfully applied a computed set of model atmosphere spectra to the interpretation of grating *Chandra* spectra of two classical SSS sources, CAL 83 and RX J0513.9 − 6951. It was shown that the new LTE model atmospheres enable us to represent the grating *Chandra* spectrum of CAL 83 with the same accuracy as the non-LTE atmospheres computed by Lanz et al. (2005) and provide similar results. However, the LTE approach has several advantages over NLTE, with the main advantage being faster computational speed, allowing us to compute much more models with various parameters. Additionally, it is easier to take into account a large number of ions and their excited levels as well as a larger number of spectral lines compared to the NLTE case.

In this article, we present a new grid of high-gravity hot LTE model atmospheres with various chemical compositions, computed using the code developed by Suleimanov et al. (2024). This grid has been used to fit eROSITA and *XMM-Newton* spectral observations of the supersoft phase of the CN AT 2018bej and we present the obtained results here.

The X-ray observations we used are described in Sect. 2. The model atmospheres and the corresponding grid of emergent spectra computed for fitting the observed spectra are presented in Sect. 3. The results of spectral fitting are presented in Sect. 4 and in Sect. 5 we discuss them in the context of modern models of thermonuclear-burned envelopes of WDs. We summarise our obtained results in Sect. 6.

2. Observations

2.1. eROSITA

As part of the eRASS1 all-sky survey, eROSITA onboard the Spectrum-Roentgen-Gamma (SRG) observatory (Predehl et al. 2021) started scanning over the position of AT 2018bej on February 12, 2020, with visits every 4 hours of 50 seconds in duration. A new X-ray source was found at RA(J2000) = $06^{\rm h}26^{\rm m}21\overset{\rm s}{.}58$ Dec(J2000) = $-69°45'49\overset{''}{.}5$, with an estimated uncertainty of 10″ radius (including systematics). This position is consistent with the known CV AT 2018bej/ASAS-SN 18jj (Ducci et al. 2020; Chomiuk et al. 2018). Later, this region was scanned during eRASS2–eRASS4 surveys in 2020 and 2021 (see the observation log in Table 1).

The data were reduced with the task `srctool` from the eROSITA Standard Analysis Software System (`eSASS`, Brunner et al. 2022) version 211214, pipeline configuration `c020` (Merloni et al. 2024, see Table E.1). We defined an annulus region with 20″ and 100″ inner and outer radius, respectively, to extract the source from eRASS1–eRASS2 observations and an inner circle with 31″ radius in the case of eRASS3, but the source was barely visible during the eRASS3 survey and it was not visible in eRASS4, so the eRASS4 observation is not shown in Table 1. For background extraction we used a 130″ circle from a nearby source-free region.

We combined the data from the five cameras with an on-chip filter: TM1–TM4 and TM6. We did not use data from TM5 and TM7 as they have calibration problems due to a light leak (Predehl et al. 2021). A cut in the fractional exposure of 0.15 (`FRACEXP` > 0.15) was applied to light curves to exclude data from the edge of the detectors. The obtained light curves are shown in Fig. 1, while the spectrum (eRASS1 epoch) is shown in Fig. 2. The eRASS1 light curve is constant on long timescales,

Table 1. X-ray observation log of AT 2018bej.

Telescope	ObsID	Date (UT)	Date (MJD)	Exp. time[(b)]	Count rate[(c)]
eROSITA/eRASS1		12–29 Feb. 2020	58 900.12[(a)]	3.96	16.4
eROSITA/eRASS2		16 Aug. – 2 Sep. 2020	59 085.75[(a)]	4.04	12.6
eROSITA/eRASS3		31 Jan. – 12 Feb. 2021	59 251.60[(a)]	3.17	0.52
XMM/RGS	0854591001	14 Mar. 2020	58 922.02	84.8/83.6[(d)]	0.44/0.48[(d)]

Notes. [(a)]MJD of the midpoint of the observation. [(b)]The corrected net exposure time in ks. [(c)]Mean count rate in counts per sec. [(d)]Exposure time and count rate of RGS1 and RGS2 instrument, respectively.

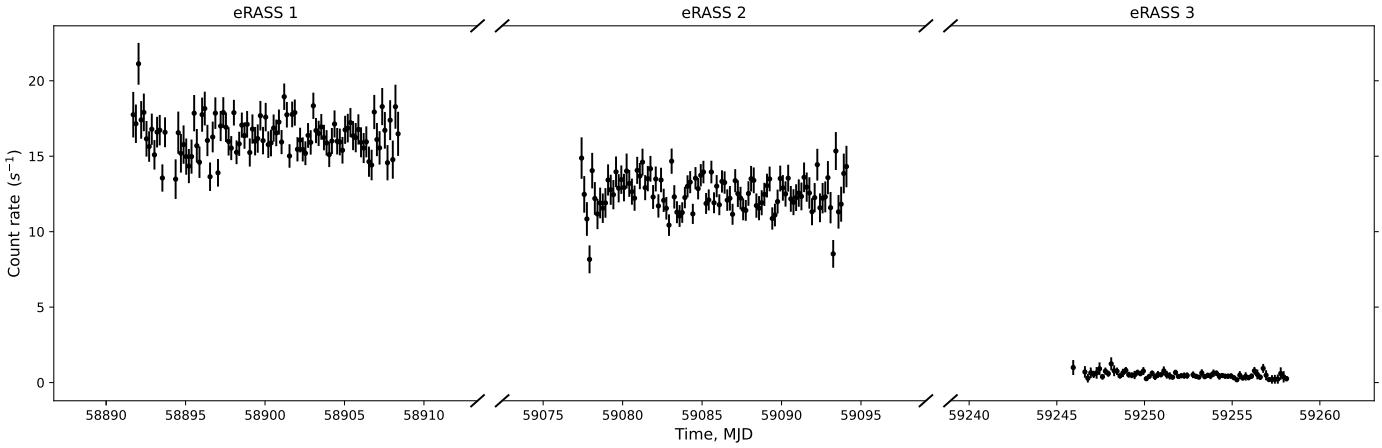

Fig. 1. eROSITA light curve of AT 2018bej in the energy band 0.2–2 keV, combining data from TM1–TM4, and TM6. eROSITA scanned the source position during four epochs eRASS1–4 until the middle of 2021. The source was barely visible during eRASS3 (right panel) and was not detected during eRASS4. The *XMM-Newton* observation started ~10 days after the end of eRASS1 scanning. The Gehrels (1986) approximation is used for bins with unknown count rate errors.

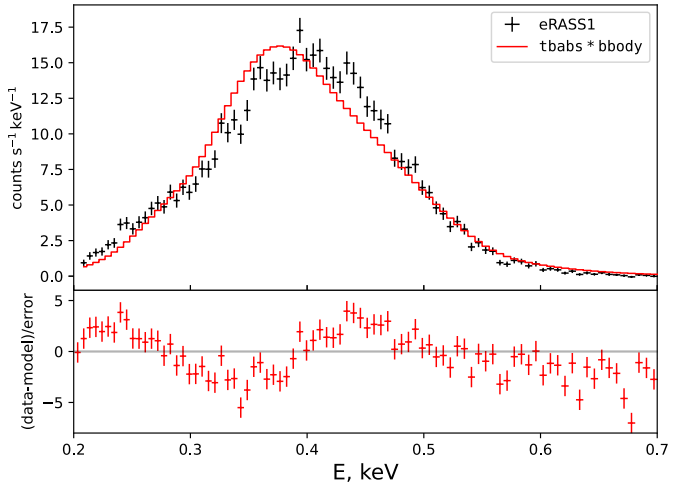

Fig. 2. eROSITA eRASS1 spectrum, combining data from TM1–TM4, and TM6. The absorbed blackbody model is also shown. The obtained blackbody parameters are presented in Table 2.

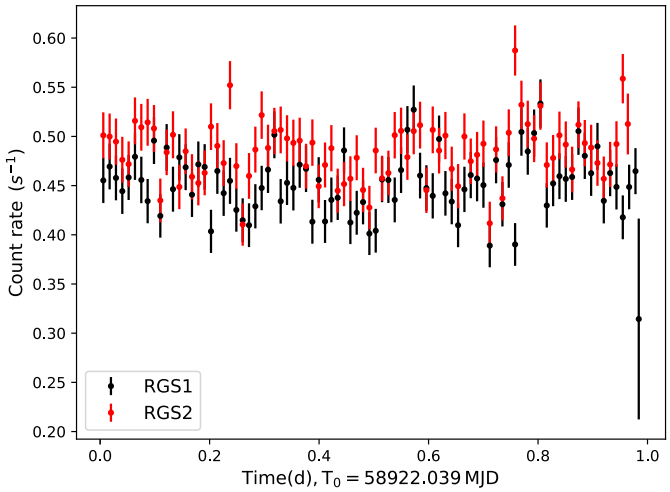

Fig. 3. *XMM-Newton* light curve of AT 2018bej in the energy band 0.3–3 keV from both RGS1 and RGS2 instruments.

indicating that the supersoft state started prior to the beginning of the eROSITA observations.

2.2. XMM-Newton

Following the eROSITA discovery, a proposal for high-resolution spectral observations was made at the *XMM-Newton* telescope. The source was observed by *XMM-Newton* Reflection Grating Spectrometer (RGS, den Herder et al. 2001) instrument on 2020 March 14, 10 days after the last eRASS1 observation (for the observation log, see Table 1). The data were processed by the *XMM-Newton* Science Analysis Software (`SAS 19.0.0`) package; the first-order spectra were used. The obtained light curve is shown in Fig. 3. It also does not show any obvious periodicity.

Table 2. Preliminary fit of AT 2018bej with blackbody model.

	eRASS1	XMM
$N_{\rm H}$, 10^{20} cm^{-2}	14.2 ± 0.5	23.3 ± 0.3
$T_{\rm eff}$, kK	423 ± 8	346 ± 2
$R^{(a)}$, 10^8cm	103^{15}_{13}	~ 600
L, 10^{37} erg s^{-1}	240^{70}_{60}	3700 ± 100
`cstat` (dof)	412.90 (128)	5481.75 (3325)

Notes. $^{(a)}$ – the distance to the LMC is assumed to be 50 kpc (Pietrzyński et al. 2019).

2.3. Preliminary analysis

The Bayesian approach was used for analysing the X-ray spectra. We applied the analysis software Bayesian X-ray Analysis (BXA, Buchner et al. 2014; Buchner 2016a), which connects the nested sampling package UltraNest[1] (Buchner 2021, 2016b) with XSPEC [2](Arnaud 1996; Arnaud et al. 1999). Posterior probability distributions and the Bayesian evidence were derived with the nested sampling Monte Carlo algorithm MLFriends (Buchner et al. 2014; Buchner 2019). To construct the corner plots, the `corner`[3] package was used (Foreman-Mackey 2016, 2017).

It is known that for low-count spectra the usage of C-statistics (Cash 1979) is preferable instead of the χ^2-statistics. We used its XSPEC implementation `cstat` as a likelihood in order to determine the best-fit parameters. The parameter uncertainties are derived from the 0.16 and 0.84 quantiles of the posterior distribution (which corresponds to 68% CL). As there is no convenient criterion of estimating the goodness of fit (as in the case of χ^2_ν) for `cstat`, we give the statistics value and the number of degrees of freedom below.

At first, the eROSITA and RGS spectra were fitted by the simple blackbody model, while for the absorption, we used the Tübingen-Boulder ISM absorption model `tbabs`. The eROSITA spectrum with the blackbody fit is shown in Fig. 2. However, these results are considered non-physical, because the emitting radii of $(1-6) \cdot 10^5$ km (assuming a LMC distance of 50 kpc, see Table 2) are inconsistent with a typical WD radius, and the resulting luminosity significantly exceeds the Eddington limit for typical WD masses. This is not surprising, as it is well known that blackbody fits tend to overestimate $N_{\rm H}$ and underestimate the temperature (see e.g. Greiner et al. 1991; Heise et al. 1994). Therefore, hot WD model atmosphere spectra are necessary to reproduce SSS spectra.

Alternatively, Suleimanov et al. (2024) computed a new set of LTE model-atmosphere spectra and showed that these models allow us to represent the spectra of two classical SSS sources, CAL 83 and RX J0513.9 − 6951. In the cited article, three model grids were also calculated for three chemical compositions: the H/He mix was solar, and the abundance of heavy elements was set to solar, 0.1∗solar, and 0.5∗solar. The latter abundances correspond to the SMC and LMC composition. A preliminary analysis of all spectra with these models gives $T_{\rm eff} \approx 570-600$ kK and $\log g \approx 8.25$, with the LMC composition preferred.

[1] https://johannesbuchner.github.io/UltraNest/
[2] https://heasarc.gsfc.nasa.gov/docs/xanadu/xspec/
[3] https://corner.readthedocs.io/en/latest

3. Model atmospheres

To describe the observed X-ray spectrum of the object, we computed our own model-grid spectra of hot WDs. We used our code, which is based on Kurucz's code ATLAS (Kurucz 1970), and modified it for high temperatures and high densities (Ibragimov et al. 2003; Suleimanov et al. 2006, 2015). The 15 most abundant chemical elements from H to Ni were taken into account, along with about 20 000 lines from CHIANTI, Version 3.0, atomic database (Dere et al. 1997). The main model parameters are the effective temperature, $T_{\rm eff}$, and the gravity, $\Delta \log g = \log g - \log g_{\rm Edd}$. The latter indicates the distance of model from the Eddington limit:

$$\log g_{\rm Edd} = \log(\sigma_{\rm e}\sigma_{\rm SB}T^4/c) = 4.818 + 4\log(T_{\rm eff}/10^5{\rm K}), \quad (1)$$

as detailed in Suleimanov et al. (2024).

The chemical composition of the WD atmosphere during the SSS phase after the nova explosion is significantly different from that of the accreted matter (see e.g. Rauch et al. 2010) due to thermonuclear fusion products being brought to the surface. Therefore, it is necessary to calculate the model atmospheres with chemical compositions close to the expected one.

It was assumed that the initial chemical composition was LMC-like (solar H/He mix and half-solar heavy elements abundance). Then, some part of the hydrogen was transformed into helium via the CNO-cycle, resulting in an increase in the number fraction of CNO. We used the composition of Rauch's NLTE models as a starting point. The ratios of the number fractions of hydrogen and helium in these models are equal to each other, the carbon number fraction is less than solar, and the number fractions of nitrogen and oxygen increase in comparison with the solar values. In particular, in Rauch's model 006[4], which we considered a fiducial model, $A_{\rm H}/A_{\rm He} = 0.48/0.48$, and the number fraction of carbon is $A_{\rm C} = 0.39 *$ solar. We considered various ratios of $A_{\rm H}/A_{\rm He}$ and ultimately adopted 0.46/0.54. Technically, from a statistical point of view, a ratio of $A_{\rm H}/A_{\rm He} = 0.0/1.0$ is a bit more likely; however, we considered it less physical, as it is assumed that active hydrogen thermonuclear burning still occurs at the surface of the WD. The number fraction of carbon was considered as an additional free parameter of the model.

Thus, in addition to $T_{\rm eff}$ and $\Delta \log g$, a new parameter has been introduced – the number fraction of carbon '`chem`' in solar units. The number fraction of nitrogen is varied from 1.89 to 0.5 in solar units depending on '`chem`' in assumption that (0.5 − `chem`) of carbon is transformed into nitrogen. Thus, the resulting abundance of carbon '`chem`' changes from 0 (all C→N) to 0.5 (LMC composition). The abundance of other elements is assumed to be 0.5 ∗ solar (we use solar abundances from Asplund et al. 2009).

Based on the preliminary fit analysis, altogether 288 models were calculated for $T_{\rm eff}$ from 525 to 700 kK in steps of 25 kK, $\Delta \log g = 0.1, 0.2, 0.4, 0.6, 1.0, 1.4$, and `chem` = 0.0, 0.1, 0.2, 0.3, 0.4, 0.5. We refer to this model as the `chem`-model hereafter. All the spectra were implemented as a tabular XSPEC-format model.

Examples of emergent spectra of the models are shown in Figs. 4 and 5 for different values of $T_{\rm eff}$ and $\Delta \log g$, while `chem` = 0.3 is fixed. The absorption edges corresponding to photoionisation from the ground level of C VI (0.49 keV), N VI (0.55 keV), and N VII (0.66 keV) ions are clearly seen. These edges lead to significant deviation of the model atmosphere

[4] http://astro.uni-tuebingen.de/~rauch/TMAF/flux_HHeCNONeMgSiS_gen.html

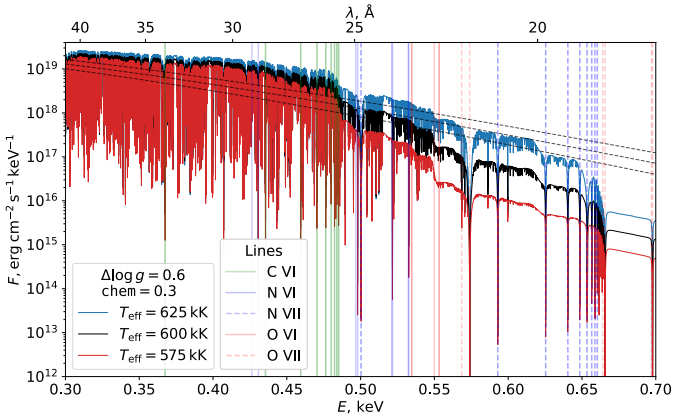

Fig. 4. Emergent spectra of model atmospheres with different $T_{\rm eff}$ values. The spectral series for some CNO ions are also indicated. The grey dashed lines represent the corresponding blackbody spectra.

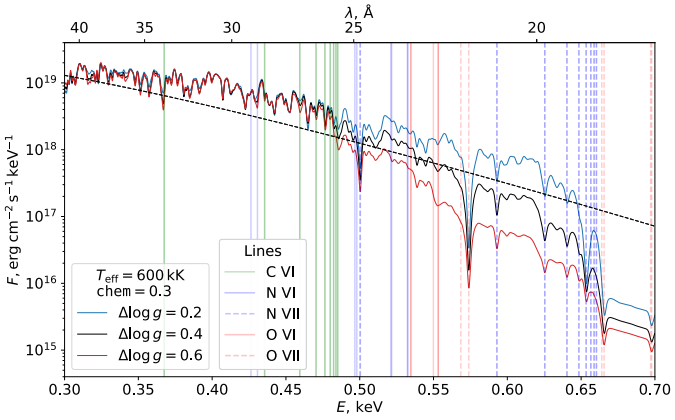

Fig. 5. Emergent model spectra with various surface gravity (three values of gravity $\Delta \log g$). The spectra are smoothed using a Gaussian kernel with resolution $R \approx 650$. Notations are the same as in Fig. 4.

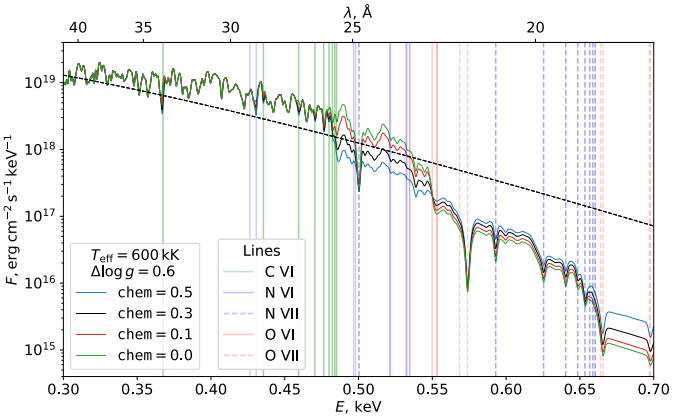

Fig. 6. Emergent model spectra with different values of the chem parameter. The spectra are also smoothed (see Fig. 5). Notations are the same as in Fig. 4.

spectra from the corresponding blackbody flux (indicated by dashed-grey lines). The spectra are dominated by a forest of absorption lines (spectral series of some CNO ions are shown), but the main influence on the common shape of the spectra comes from the effective temperature. The spectra in Fig. 5 are convolved for clarity with a Gaussian kernel with *XMM-Newton* RGS resolution of $R \approx 650$ in the observed soft X-ray energy

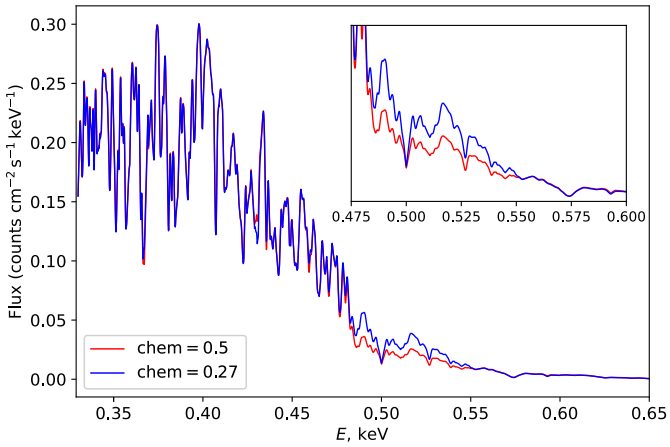

Fig. 7. Comparison of the convolved spectra for different chemical compositions with the same values: $T_{\rm eff} = 604$ kK, $\Delta \log g = 0.51$, $N_{\rm H} = 5.88 \times 10^{20}$ cm^{-2}. These are the cases for chem = 0.0 (i.e. $A_{\rm H}/A_{\rm He} = 0.46/0.54$, $A_{\rm rest} = 0.5 *$ solar, indicated in blue) and chem = 0.27 (the best-fit value of carbon abundance, in red). The 0.47−0.6 keV region is also shown in detail.

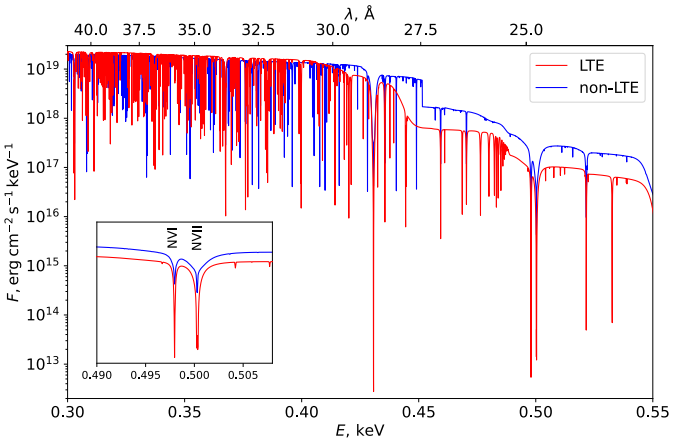

Fig. 8. Comparison of the model atmospheres spectra computed by our code (in red) and the TMAP non-LTE code (Rauch et al. 2010, in blue). Both models have $T_{\rm eff} = 600$ kK, $\log g = 9$. The chemical composition corresponds to model 006 from Rauch's grid. The lower left panel shows in detail the comparison of absorption line profiles.

range. The gravity mainly affects the 0.48−0.65 keV energy range, which is covered by RGS.

Figure 6 shows some examples of models for different values of the chem-parameter. The spectra were also convolved with a Gaussian kernel with *XMM-Newton* RGS resolution $R \approx 650$ in the observed soft X-ray energy range. The chemical composition mainly affects the 0.48–0.65 keV energy range, which is covered by RGS. Although the changes resulting from the chemical composition are smaller, the spectral resolution of *XMM-Newton* allows for accurate determinations to be obtained (see the convolved spectrum in Fig. 6). In addition, the overall spectrum level in this region is clearly distinguishable in the eROSITA spectrum. Also, Fig. 7 shows the comparison between spectra convolved with the XMM response for chem = 0.27 and 0.5 (LMC composition), while temperature and gravity are fixed at $T_{\rm eff} = 605$ kK, $\Delta \log g = 0.52$. The notable deviation in the 0.48−0.55 keV region is clearly visible.

We also compared our LTE models with NLTE models computed by Rauch et al. (2010). Figure 8 shows the comparison

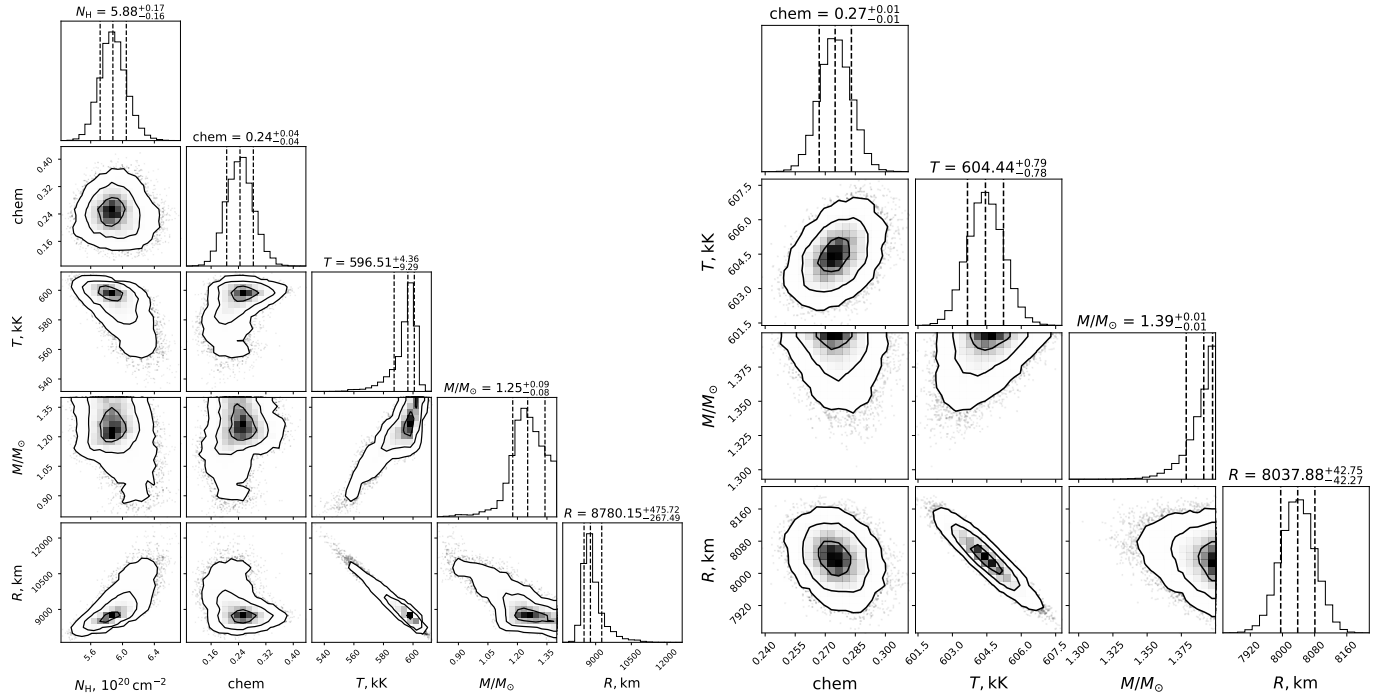

Fig. 9. Corner plot of the parameters' posterior distribution for the eRASS1 spectrum (left panel) and for the *XMM-Newton* RGS spectrum (right panel) of AT 2018bej. The WD mass, M, and radius, R, are considered as free parameters. The 2D contours correspond to 39.3, 86.5, and 98.9% confidence levels. The histograms show the normalised 1D distributions for a given parameter derived from the posterior samples. The hydrogen column density is fixed at $N_H = 5.88 \times 10^{20}$ cm^{-2} for the RGS spectrum.The best-fit parameter values are presented in Table 3.

between the emergent spectrum of Rauch's NLTE model 006 and our LTE spectrum with the same chemical composition. Both spectra were binned to a 0.002 Å interval within the 10−60 Å wavelength range. The general shapes of the spectra are similar, however, there are some differences seen in the absorption-edge regions. Due to an over-ionisation of the ions (relative to the LTE case), the absorption jumps in the NLTE spectrum appear shallower. Additionally, a sharp jump occurs in the NLTE spectrum at 0.45 keV, associated with ionisation from an excited level of Si XI. This feature is much smoother in our spectrum. Our list of lines is also different, resulting in variations in the line distribution in the spectra. The line broadening of H-like ions seems to differ, as seen in the lower left panel in Fig. 8, where the N VI and N VII lines are depicted. The broadening of the resonance lines is primarily determined by radiative damping in addition to Doppler broadening. In contrast, the wide wings of the resonance line N VII in the NLTE spectrum are also affected by the Stark effect. Additionally, the level populations differ between LTE and NLTE models, causing the lines in the LTE spectrum to appear deeper. Namely, the upper layers of LTE models are obviously cooler than those of NLTE models and the corresponding ions are more populated. This indicates that a decreased abundance of some elements is needed compared to NLTE models to describe the same observed spectral line absorption.

We investigated the uncertainty that may arise from using LTE models instead of NLTE models. It is possible to demonstrate that a NLTE model spectrum with $T_{\rm eff} = 550$ kK reproduces almost the same general spectrum shape with the same absorption jump strengths as the LTE model spectrum with $T_{\rm eff} = 600$ kK, while the gravity $\log g$ is fixed, see Fig. A.1. Reducing $\log g$ while fixing the temperature leads to the same effect. Thus, using LTE atmospheres may lead to an overestimation of temperature by ∼10% and/or to an underestimation of $\log g$ by ∼0.5 dex (see Fig. A.2). We note that both of these effects occur simultaneously and we can only conclude that LTE model atmospheres slightly overestimate the effective temperature and slightly underestimate the surface gravity of a hot WD as a result of fitting its soft X-ray spectrum.

This occurs because the elements under NLTE conditions are over-ionised compared to the LTE case. Consequently, higher temperatures and/or lower plasma densities are needed in LTE atmospheres to compensate for this effect.

4. Analysis of the spectra

All the observed spectra, eRASS1, eRASS2, and *XMM-Newton* (see Table 1), were fitted with the `chem`-model described above. Using temperature, $T_{\rm eff}$, and gravity, $\Delta \log g$, as free parameters leads to a degeneracy in the gravity distribution and to a nonphysical estimation of the WD mass. Therefore, we fit the spectra using WD mass M and radius R as free parameters and set a strict upper limit of $M = 1.4\,M_\odot$. For both eROSITA and XMM spectra a uniform prior distribution was set for $N_{\rm H}$ (in the range: $(1-10) \times 10^{20}$ cm^{-2}), '`chem`' parameter, effective temperature, $T_{\rm eff}$, WD mass, M (in the range: 0.3−1.4 $M_\odot$) and radius R (in the range: $(2-20) \times 10^3$ km). Also, the additional lower limit was set for the radius to obtain a physically adequate result; thus R should be greater than the radius of cold WD $R_{\rm cold}$ (Nauenberg 1972) with the same mass.

The example of the resulting corner plot for the eRASS1 spectrum is shown in the left panel of Fig. 9, while the obtained parameters for all the fits are presented in Table 3. Figure 10 shows the comparison between the observed and model eROSITA spectrum. The parameters' posterior distributions for all spectra are narrow enough and have only one mode, resulting in smaller errors. However, the WD mass tends to its upper limit, especially for the XMM case.

Table 3. Spectral parameters of the LTE model fit for AT 2018bej.

	eRASS1	eRASS2	XMM	XMM [a]	eRASS1 [d]	eRASS2 [d]
$N_{\rm H}$, 10^{20} cm^{-2}	$5.88\pm^{0.17}_{0.16}$	5.69 ± 0.15	$3.06\pm^{0.12}_{0.13}$	5.88 [a]	$5.83\pm^{0.14}_{0.16}$	
$T_{\rm eff}$, kK	$597\pm^{4}_{9}$	$541\pm^{10}_{14}$	631 ± 1	604 ± 1	$578\pm^{14}_{11}$	$554\pm^{8}_{11}$
$M/M_\odot$	$1.25\pm^{0.09}_{0.08}$	$0.81\pm^{0.13}_{0.08}$	1.39 ± 0.01	1.39 ± 0.01	$1.07\pm^{0.08}_{0.11}$	
R [b], km	$8780\pm^{476}_{267}$	$11\,001\pm^{799}_{629}$	$5934\pm^{74}_{77}$	$8038\pm^{43}_{42}$	$9541\pm^{601}_{750}$	$10\,393\pm^{678}_{514}$
L, 10^{37} erg s^{-1}	$7.0\pm^{0.8}_{0.6}$	$7.4\pm^{1.2}_{1.1}$	4.0 ± 0.1	6.1 ± 0.1	$7.3\pm^{1.2}_{1.3}$	$7.3\pm^{1.0}_{0.9}$
$\log g$	$8.33\pm^{0.06}_{0.04}$	$7.95\pm^{0.09}_{0.07}$	8.72 ± 0.01	8.46 ± 0.01	$8.19\pm^{0.06}_{0.08}$	$8.12\pm^{0.07}_{0.06}$
$\Delta \log g$	$0.41\pm^{0.06}_{0.05}$	$0.20\pm^{0.10}_{0.08}$	0.70 ± 0.01	0.51 ± 0.01	$0.33\pm^{0.08}_{0.09}$	0.33 ± 0.07
$A_{\rm C}$, sol	0.24 ± 0.04	$0.20\pm^{0.05}_{0.04}$	0.22 ± 0.01	0.27 ± 0.01	0.21 ± 0.04	0.16 ± 0.04
$A_{\rm N}$, sol	1.14 ± 0.11	$1.33\pm^{0.11}_{0.14}$	1.28 ± 0.03	1.14 ± 0.03	1.30 ± 0.11	1.44 ± 0.11
`cstat` (dof) [c]	125.00 (125)	144.74 (125)	6548.12 (3323)	7019.75 (3324)	272.91 (252)	

Notes. [a]Hydrogen column density $N_{\rm H}$ is fixed. [b]Distance to the LMC assumed to be 50 kpc (Pietrzyński et al. 2019). [c]C-statistics and degrees of freedom of the best value found by the Bayesian analysis. [d]eRASS1 and eRASS2 spectra fit simultaneously with a common WD mass, M, parameter.

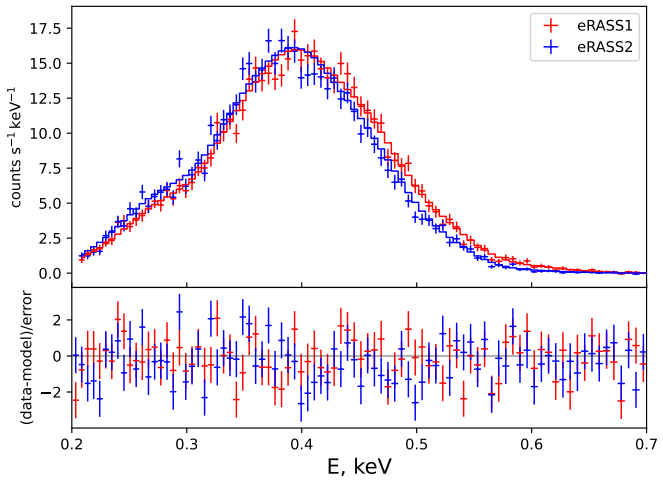

Fig. 10. Model atmosphere best-fit of the eROSITA eRASS1 (in red) and eRASS2 (in blue) spectra. The obtained parameters are presented in Table 3.

It is important to emphasise that the obtained hydrogen column density $N_{\rm H}$ is significantly different for the eROSITA and XMM spectra. Fitting the XMM spectrum provides the column density $N_{\rm H}$ is about half of that found from fitting the eROSITA spectrum; namely, the analysis of the eRASS1 spectrum yields $N_{\rm H} \approx 5.88 \times 10^{20}$ cm^{-2} (see Table 3 and Fig. 9, left panel). On the other side, the analysis of the XMM spectrum yields $N_{\rm H} \approx 3.06 \times 10^{20}$ cm^{-2}. The last value is too small compared to the Galactic absorption column in the direction of the source. The average Galactic absorption in this direction is $5.6^{+0.7}_{-0.8} \times 10^{20}$cm^{-2} based on the extinction and absorption maps presented in Doroshenko (2024)[5], who combined the results by Edenhofer et al. (2024); Yao et al. (2017) and Planck Collaboration XLVIII (2016). The H I survey (HI4PI Collaboration 2016) provides the close result $6.5^{+0.1}_{-0.1} \times 10^{20}$ cm^{-2}. Therefore, we consider the value of $N_{\rm H}$ obtained from fitting the eROSITA observation to be more reliable and this is the value we fix when describing the XMM spectrum. Specifically, we fixed $N_{\rm H} = 5.88 \times 10^{20}$ cm^{-2}. It should be also noted that we assume there is no extra $N_{\rm H}$ local to the source, so we determined only the foreground absorption component, while the Tübingen-Boulder ISM absorption model `tbabs` was used.

The corner plot and obtained parameters for the XMM observation with the fixed $N_{\rm H}$ are presented in Fig. 9 (right panel) and Table 3. The comparison between the observed and model RGS spectrum is shown in Fig. 11.

Interestingly, for both the XMM and eRASS1 spectra, regardless of the other parameters' values, the carbon abundance '`chem`' parameters are close to each other and coincide within the errors, namely, ≈0.27 and ≈0.24, respectively. They are derived quite accurately and the corresponding distributions are narrow and do not demonstrate multi-modal behaviour. Additionally, another spectrum from the next eROSITA survey, eRASS2, is available. Fitting this spectrum with the `chem`-model also yields quite a good fit with relatively small errors for '`chem`', indicating its reliable determination. This '`chem`' value is slightly lower, ≈ 0.20, than the value ≈0.27–0.24 obtained from eRASS1 and XMM spectra.

Given the availability of eROSITA spectra for two epochs, it is possible to trace the evolution of the system parameters, particularly the carbon abundance. To achieve this, a MCMC calculation was performed simultaneously for the eRASS1 and eRASS2 spectra using the `chem`-model, assuming that the WD mass is the same in both fits; therefore, it is a common free parameter for all spectra. The same uniform priors were set for the hydrogen column density, '`chem`'-parameter, effective temperature, WD mass, and radius. The corresponding posterior distribution is shown in Fig. 12 and the parameter values are presented in Table 3.

The posterior distributions of the two '`chem`'-parameters are quite narrow, and the corresponding errors are relatively small. We note that the hydrogen column density is a free parameter in this case and it converged to a plausible value of 5.83×10^{20} cm^{-2}. The inferred WD mass, $\approx 1.07\,M_\odot$, was also well determined.

We also compared our results with those obtained using non-LTE model spectra. A set of NLTE atmosphere models was calculated by Rauch et al. (2010) to describe the

[5] http://astro.uni-tuebingen.de/nh3d/nhtool

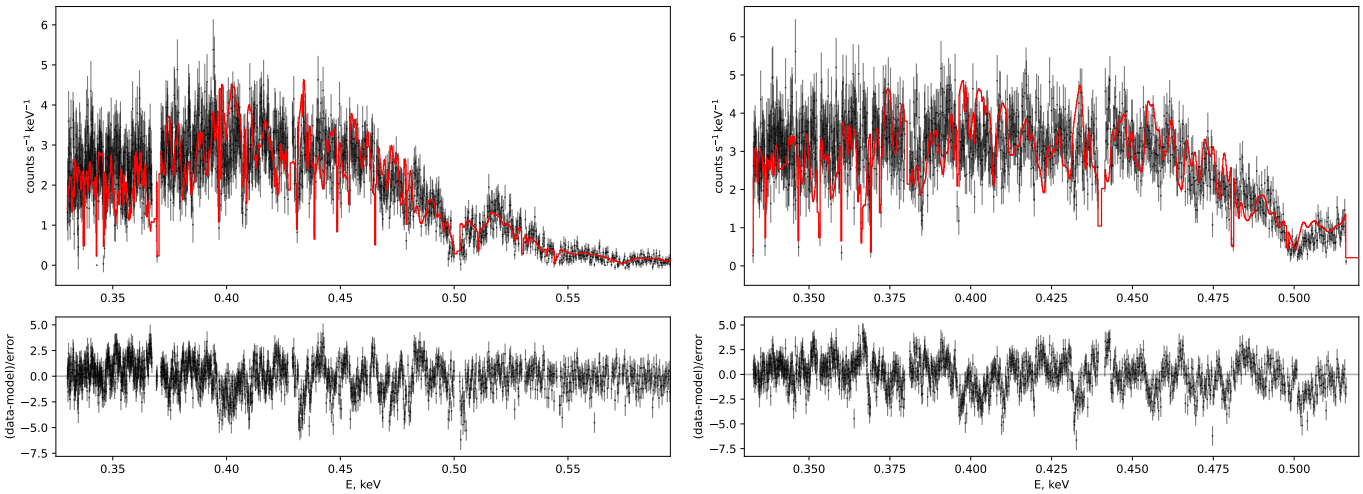

Fig. 11. *XMM-Newton* RGS spectrum obtained with the best-fit LTE model. The spectra of RGS 1 (left panel) and RGS 2 (right panel) instruments are shown. The best-fit parameters can be found in Table 3. The hydrogen column density is fixed at $N_{\rm H} = 5.88 \times 10^{20}$ cm^{-2}.

Table 4. Fit of AT 2018bej spectra with NLTE[(a)] model.

	eRASS1	XMM	XMM[(c)]
$N_{\rm H}$, 10^{20} cm^{-2}	4.8 ± 0.1	~ 8.54	4.8
$T_{\rm eff}$, kK	~ 690	~ 660	~ 630
$R^{(b)}$, km	3980 ± 20	3970 ± 20	~ 4000
$M/M_\odot$	1.19 ± 0.01	1.19 ± 0.01	1.19 ± 0.01
L, 10^{37} erg s^{-1}	~ 2.5	~ 2.2	~ 1.8
`cstat` (dof)	150.81 (128)	7440.30 (3325)	15886.52 (3326)

Notes. [(a)]TMAP NLTE model 006 by Rauch et al. (2010), $\log g = 9.0$. [(b)]Distance to the LMC assumed to be 50 kpc (Pietrzyński et al. 2019). [(c)]Hydrogen column density $N_{\rm H}$ is fixed.

spectrum of nova V4743 Sgr during its SSS phase. The chemical composition of these models has been adjusted specifically for that nova. To compare our results with NLTE models we fit our observed spectra with Rauch's model 006. The resulting WD radii $(2.2–3.7) \times 10^8$ cm and masses of $0.4–1\,M_\odot$ are significantly underestimated and the obtained radius is lower than the radius of cold WD with the similar mass. Therefore, we set a lower limit for the WD radius using Nauenberg's $M - R$ relation (see Nauenberg 1972) and the obtained results are presented in Table 4. The temperature goes down to ~660–690 kK, while the mass increases to $\sim 1.2\,M_\odot$. Again, we consider the $N_{\rm H}$ value found by the eRASS1 analysis to be more reliable and performed an additional fitting of the XMM spectrum with the fixed $N_{\rm H} = 4.8 \times 10^{20}$ cm^{-2}. The fit quality deteriorates significantly, and the mass tends to its lower limit based on the radius constraint. While the low-resolution eROSITA spectrum is (more or less) well described by the NLTE model, the quality of the XMM fit is significantly worse, compared to our LTE fit.

It should be noted that since the source luminosity is near the Eddington limit ($L \sim 0.12–0.49\,L_{\rm Edd}$ for different LTE/NLTE fits), NLTE effects are not negligible. However, the spectral resolution of eROSITA observations is insufficient to reveal these effects. While the XMM resolution, in principle, allows us to distinguish NLTE effects, they would only moderately affect the result (e.g. by ~10% in the temperature; see the end of Sect. 3). In addition, the available NLTE models were computed only with fixed $\log g = 9$. Possibly, NLTE models with smaller $\log g$ would be able to fit the observed spectra with better accuracy. Nevertheless, Suleimanov et al. (2024) compared the results of fitting the *Chandra* and XMM spectra of the classical SSS CAL 83 using LTE models and NLTE models by Lanz et al. (2005), finding that both approaches yield similar results. This supports the use of LTE models for analysing the spectra of SSSs.

5. Discussion

Our analysis of the joint eRASS1 and eRASS2 fit allows us to investigate the evolution of the source on a half-year scale. Although the effective temperature of the hot WD slightly decreases and the photospheric radius slightly increases, the changes in the parameter values are marginal and remain within the errors. Formally, the carbon abundance decreases from 0.21 to 0.16 of the solar value, but the error of '`chem`' determination is comparable with the difference between these two values, as seen in Fig. 13. In conclusion, even the low-resolution spectral analysis shows hints of the evolution of the source parameters, including the WD's chemical composition, but observations more separated in time are necessary for a more reliable study of evolution.

It should be noted that the mass obtained from fitting different spectra varies, with a tendency to approach its upper limit. Therefore, for a more reliable mass determination, we compare the obtained results with theoretical predictions. Models of WD envelopes with hydrogen thermonuclear burning have been computed by several groups (see e.g. Wolf et al. 2013; Nomoto et al. 2007). In particular, Nomoto et al. (2007) calculated the $R - T_{\rm eff}$ dependencies for different masses of WDs with hydrogen-rich envelope. We converted these dependencies into $T_{\rm eff} - \log g$ dependencies, and put all the obtained data on the corresponding plane (see Fig. 14). We included all our fits on the figure, including the different eRASS observations, the XMM observation with fixed $N_{\rm H}$, and the joint eROSITA fit with a common M parameter.

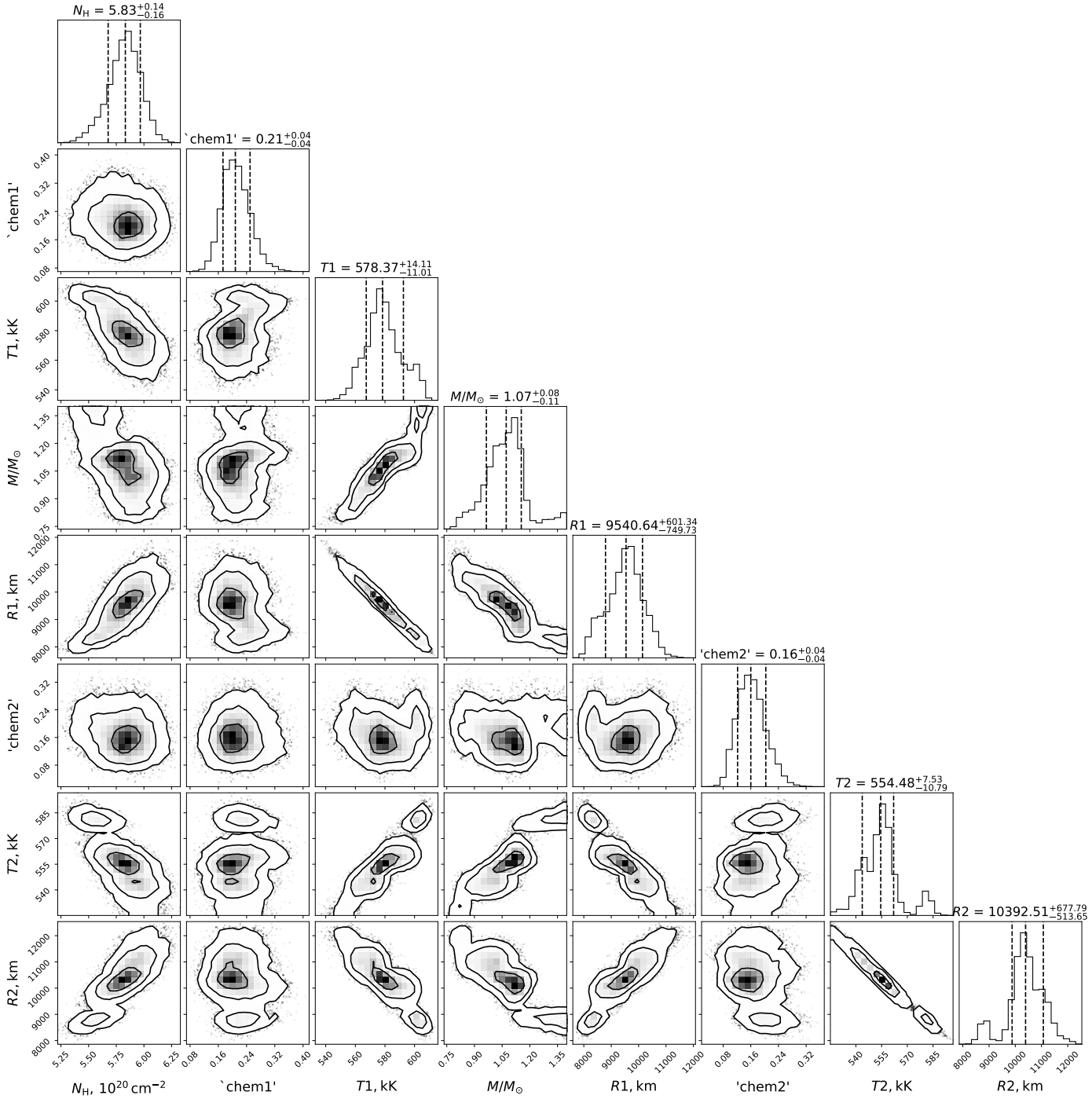

Fig. 12. Corner plot of the parameters' posterior distribution for eRASS1 and eRASS2 spectra fitted simultaneously with a common WD mass parameter. The 2D contours correspond to 39.3, 86.5, and 98.9% confidence levels. The histograms show the normalised 1D distributions for a given parameter derived from the posterior samples. The best-fit parameter values are presented in Table 3.

All the positions of the source on the plane $T_{\rm eff} - \log g$ lie at the model dependencies corresponding to 1.1−1.15 $M_\odot$, although it should be noted that the errors are large for the eRASS2 fit. This value of the WD mass is in a good agreement with the WD mass derived from the joint eRASS1 and eRASS2 fit. It means that the estimation of the WD mass M = 1.05−1.15 $M_\odot$ could be correct. We also emphasise that all fit positions found lie above the steady-burning limit for WDs (red dashed line in Fig. 14). This confirms our assumption that the source undergoes steady hydrogen burning on its surface. Moreover, the eRASS2 source position moves further away from the lower boundary of the stable burning strip, indicating an increase in the intensity of the thermonuclear burning from eRASS1 to eRASS2 observations. This fact is supported by the increased bolometric luminosity.

It should be noted that setting $N_{\rm H}$ as a free parameter for the XMM fit leads to a significant increase in gravity, causing the model mass to approach the limit mass of 1.4 $M_\odot$. As

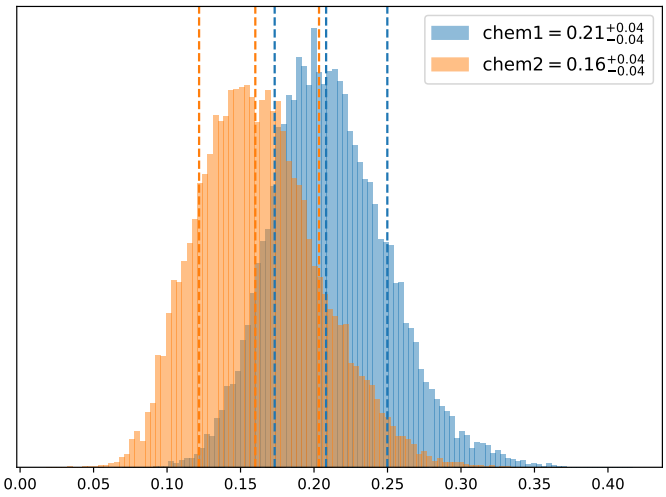

Fig. 13. 1D distribution for eRASS1 (in blue) and eRASS2 (in orange) 'chem'-parameter. The spectra were fitted simultaneously using the Bayesian approach, while the WD mass parameter was common for both spectra. Vertical lines show the 16th, 50th, and 84th percentiles for the 'chem' distribution.

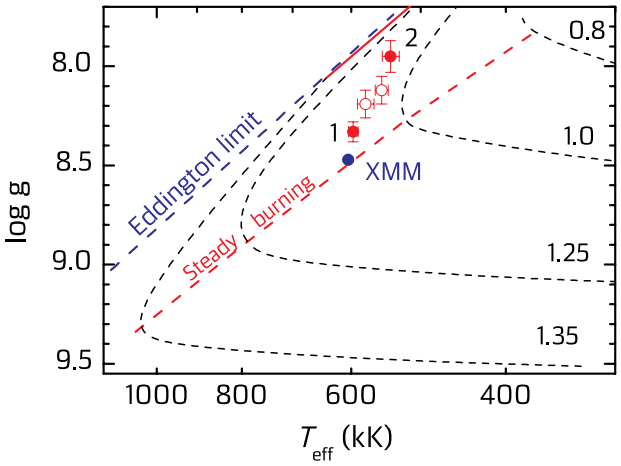

Fig. 14. Positions of the source in the $T_{\rm eff} - \log g$ plane according to different eRASS observations (red circles with the number 1 and 2), and according to joint fit (red empty circles), see Table 3. The XMM spectrum fit with fixed $N_{\rm H}$ is shown by blue circle. Model dependencies for various WD masses, taken from Nomoto et al. (2007), are shown by black dashed curves. The numbers at the curves indicate WD masses (in solar masses). The lower boundary of the stable thermonuclear burning band is shown by the dashed red line. The Eddington limit for solar H/He abundances is shown by the blue dashed line.

mentioned earlier in this paper, we do not consider such a fit to be satisfactory (and the corresponding point is not shown in Fig. 14).

6. Summary

We performed a spectral analysis of the supersoft X-ray phase of the classical nova AT 2018bej, which was observed for the first time in X-rays by the eROSITA and *XMM-Newton* telescopes. To describe the spectrum, we calculated high-gravity hot LTE model atmospheres with chemical compositions typical for nova SSS phases. In particular, we assumed that the number fractions of hydrogen and helium are almost equal, namely, $A_{\rm H}/A_{\rm He} = 0.46/0.54$. The heavy element abundances are taken equal to the half of the solar abundances for all the elements, excluding carbon and nitrogen. We considered five different values of $A_{\rm C}$ from 0.0 to 0.5 of the solar value. The nitrogen abundance is connected with $A_{\rm C}$ under the assumption that all the carbon deficiency transforms to the nitrogen excess above 0.5 of the solar value. The grid covers $T_{\rm eff}$ = 525−700 kK in steps of 25 kK, $\Delta \log g = \log g - \log g_{\rm Edd}$ = 0.1, 0.2, 0.4, 0.6, 1.0, 1.4, and five values of carbon abundance ('chem'-parameter). The code developed by Suleimanov et al. (2024) was used for this aim.

Separate fits of the individual eRASS1 and eRASS2 observations reveal remarkable changes in the physical properties of the source on a half-year timescale. The effective temperature decreased, while the photospheric radius increased. Although the observed soft X-ray flux decreased, the derived bolometric luminosity slightly increased. The most potentially interesting change is the marginal decrease in carbon abundance between these two observations, from ≈0.24 to ≈0.20 of the solar one. The fit of the XMM/RGS spectrum yields results close to those obtained from the eRASS1 spectrum analysis if we fix the interstellar absorption.

In addition to the individual fits, we performed a simultaneous fitting of the eROSITA spectra for two epochs (eRASS1 and eRASS2) with a common WD mass parameter. This assumption is strongly physically motivated and allows us to trace the evolution of the source more reliably. However, the analysis demonstrates only marginal evolution of parameters. Although the effective temperature slightly decreases, accompanied by a slight increase in the WD radius, the bolometric luminosity is constant. A slight carbon abundance decrease was also confirmed.

We compared the WD mass obtained from the joint eROSITA spectra fit of $1.07^{+0.08}_{-0.11}\,M_\odot$ with the theoretical predictions. The predictions were derived from the positions of the best-fit parameters of the spectra on the $T_{\rm eff} - \log g$ plane, where model curves for different WD masses are also displayed. The positions of the fits correspond to WD masses of 1.1−1.15 $M_\odot$. Thus, we concluded that the mass of the WD in the investigated nova falls within the range of 1.05−1.15 $M_\odot$.

To summarise, our simplified LTE approach provides a satisfactory description of the X-ray spectra of the supersoft X-ray stage of a classical nova. It may potentially help to explain the spectra of other similar objects.

Acknowledgements. This work was supported by the *Deutsche Forschungsgemeinschaft* under grants WE1312/56–1 (AT) and WE1312/59–1 (VFS). This work is partially supported by the *Bundesministerium für Wirtschaft und Energie* through the *Deutsches Zentrum für Luft- und Raumfahrt e.V. (DLR)* under the grant number FKZ 50 QR 2102 (LD). This work is based on data from eROSITA, the soft X-ray instrument aboard SRG, a joint Russian-German science mission supported by the Russian Space Agency (Roskosmos), in the interests of the Russian Academy of Sciences represented by its Space Research Institute (IKI), and the Deutsches Zentrum für Luft- und Raumfahrt (DLR). The SRG spacecraft was built by Lavochkin Association (NPOL) and its subcontractors, and is operated by NPOL with support from the Max Planck Institute for Extraterrestrial Physics (MPE). The development and construction of the eROSITA X-ray instrument was led by MPE, with contributions from the Dr. Karl Remeis Observatory Bamberg & ECAP (FAU Erlangen-Nuernberg), the University of Hamburg Observatory, the Leibniz Institute for Astrophysics Potsdam (AIP), and the Institute for Astronomy and Astrophysics of the University of Tübingen, with the support of DLR and the Max Planck Society. The Argelander Institute for Astronomy of the University of Bonn and the Ludwig Maximilians Universität Munich also participated in the science preparation for eROSITA. The eROSITA data shown here were processed using the eSASS software system developed by the German eROSITA consortium.

References

Arnaud, K. A. 1996, ASP Conf. Ser., 101, 17
Arnaud, K., Dorman, B., & Gordon, C. 1999, Astrophysics Source Code Library [record ascl:9910.005]
Asplund, M., Grevesse, N., Sauval, A. J., & Scott, P. 2009, ARA&A, 47, 481
Baron, E., Chen, B., & Hauschildt, P. H. 2010, Astrophysics Source Code Library [record ascl:1010.056]
Bode, M. F., & Evans, A. 2008, Classical Novae (Hoboken: Wiley), 43
Brunner, H., Liu, T., Lamer, G., et al. 2022, A&A, 661, A1
Buchner, J. 2016a, Astrophysics Source Code Library [record ascl:1610.011]
Buchner, J. 2016b, Astrophysics Source Code Library [record ascl:1611.001]
Buchner, J. 2019, PASP, 131, 108005
Buchner, J. 2021, J. Open Source Softw., 6, 3001
Buchner, J., Georgakakis, A., Nandra, K., et al. 2014, A&A, 564, A125
Burwitz, V., Reinsch, K., Greiner, J., et al. 2007, Adv. Space Res., 40, 1294
Cash, W. 1979, ApJ, 228, 939
Chomiuk, L., Strader, J., Shishkovsky, L., et al. 2018, ATel, 11610, 1
den Herder, J. W., Brinkman, A. C., Kahn, S. M., et al. 2001, A&A, 365, L7
Dere, K. P., Landi, E., Mason, H. E., Monsignori Fossi, B. C., & Young, P. R. 1997, A&AS, 125, 149
Doroshenko, V. 2024, A&A, submitted [arXiv:2403.03127]
Ducci, L., Ji, L., Haberl, F., et al. 2020, ATel, 13545, 1
Edenhofer, G., Zucker, C., Frank, P., et al. 2024, A&A, 685, A82
Foreman-Mackey, D. 2016, J. Open Source Softw., 1, 24
Foreman-Mackey, D. 2017, Astrophysics Source Code Library [record ascl:1702.002]
Gehrels, N. 1986, ApJ, 303, 336
Greiner, J. 2000, New A, 5, 137
Greiner, J., Hasinger, G., & Kahabka, P. 1991, A&A, 246, L17
Hachisu, I., & Kato, M. 2006, ApJS, 167, 59
Hartmann, H. W., & Heise, J. 1996, in Supersoft X-Ray Sources, eds. J. Greiner (Berlin: Springer), 472, 25
Hartmann, H. W., & Heise, J. 1997, A&A, 322, 591
Hartmann, H. W., Heise, J., Kahabka, P., Motch, C., & Parmar, A. N. 1999, A&A, 346, 125
Hauschildt, P. H., & Baron, E. 1999, J. Comput. Appl. Math., 109, 41
Heise, J., van Teeseling, A., & Kahabka, P. 1994, A&A, 288, L45
Henze, M., Pietsch, W., Haberl, F., et al. 2014, A&A, 563, A2
HI4PI Collaboration (Ben Bekhti, N., et al.) 2016, A&A, 594, A116
Hubeny, I., & Lanz, T. 1995, ApJ, 439, 875
Hubeny, I., & Lanz, T. 2011, Astrophysics Source Code Library [record ascl:1109.021]
Ibragimov, A. A., Suleimanov, V. F., Vikhlinin, A., & Sakhibullin, N. A. 2003, Astron. Rep., 47, 186
Kahabka, P. 2006, Adv. Space Res., 38, 2836
Kahabka, P., & van den Heuvel, E. P. J. 1997, ARA&A, 35, 69
Kahabka, P., Hartmann, H. W., Parmar, A. N., & Negueruela, I. 1999, A&A, 347, L43
Kurucz, R. L. 1970, SAO Special Report, 309
Lanz, T., Telis, G. A., Audard, M., et al. 2005, ApJ, 619, 517
Long, K. S., Helfand, D. J., & Grabelsky, D. A. 1981, ApJ, 248, 925
Maitra, C., & Haberl, F. 2022, A&A, 657, A26
Merloni, A., Lamer, G., Liu, T., et al. 2024, A&A, 682, A34
Nauenberg, M. 1972, ApJ, 175, 417
Ness, J. U. 2010, Astron. Nachr., 331, 179
Ness, J. U., Starrfield, S., Burwitz, V., et al. 2003, ApJ, 594, L127
Ness, J. U., Osborne, J. P., Henze, M., et al. 2013, A&A, 559, A50
Nomoto, K., Saio, H., Kato, M., & Hachisu, I. 2007, ApJ, 663, 1269
Orio, M., Covington, J., & Ögelman, H. 2001, A&A, 373, 542
Parmar, A. N., Kahabka, P., Hartmann, H. W., et al. 1997, A&A, 323, L33
Parmar, A. N., Kahabka, P., Hartmann, H. W., Heise, J., & Taylor, B. G. 1998, A&A, 332, 199
Petz, A., Hauschildt, P. H., Ness, J. U., & Starrfield, S. 2005, A&A, 431, 321
Pietrzyński, G., Graczyk, D., Gallenne, A., et al. 2019, Nature, 567, 200
Planck Collaboration XLVIII. 2016, A&A, 596, A109
Predehl, P., Andritschke, R., Arefiev, V., et al. 2021, A&A, 647, A1
Rappaport, S., Di Stefano, R., & Smith, J. D. 1994, ApJ, 426, 692
Rauch, T. 2003, A&A, 403, 709
Rauch, T., & Werner, K. 2010, Astron. Nachr., 331, 146
Rauch, T., Orio, M., Gonzales-Riestra, R., et al. 2010, ApJ, 717, 363
Seward, F. D., & Mitchell, M. 1981, ApJ, 243, 736
Soraisam, M. D., Gilfanov, M., Wolf, W. M., & Bildsten, L. 2016, MNRAS, 455, 668
Starrfield, S., Timmes, F. X., Hix, W. R., et al. 2004, ApJ, 612, L53
Starrfield, S., Iliadis, C., & Hix, W. R. 2016, PASP, 128, 051001
Suleimanov, V. F., & Ibragimov, A. A. 2003, Astron. Rep., 47, 197
Suleimanov, V., Madej, J., Drake, J. J., Rauch, T., & Werner, K. 2006, A&A, 455, 679
Suleimanov, V. F., Mauche, C. W., Zhuchkov, R. Y., & Werner, K. 2015, Acta Polytechnica CTU Proceedings, 2, 143
Suleimanov, V. F., Tavleev, A. S., Doroshenko, V., & Werner, K. 2024, A&A, 688, A39
Swartz, D. A., Ghosh, K. K., Suleimanov, V., Tennant, A. F., & Wu, K. 2002, ApJ, 574, 382
Trümper, J., Hasinger, G., Aschenbach, B., et al. 1991, Nature, 349, 579
van den Heuvel, E. P. J., Bhattacharya, D., Nomoto, K., & Rappaport, S. A. 1992, A&A, 262, 97
van Rossum, D. R. 2012, ApJ, 756, 43
van Rossum, D. R., & Ness, J. U. 2010, Astron. Nachr., 331, 175
Werner, K., Deetjen, J. L., Dreizler, S., et al. 2003, ASP Conf. Ser., 288, 31
Werner, K., Dreizler, S., & Rauch, T. 2012, Astrophysics Source Code Library [record ascl:1212.015]
Wolf, W. M., Bildsten, L., Brooks, J., & Paxton, B. 2013, ApJ, 777, 136
Yao, J. M., Manchester, R. N., & Wang, N. 2017, ApJ, 835, 29

Appendix A: Additional figures

Here, we present the results that have allowed us to estimate the uncertainties arising due to using LTE model atmospheres instead of NLTE models. The main NLTE effect important for us is over-ionisation, which leads to a decrease in the photoionisation jumps. To compensate for this effect under an LTE assumption, we have to increase the plasma temperature or decrease the plasma density. We demonstrate here that a NLTE model atmosphere with $T_{\rm eff}$ = 550 kK reproduces the general spectral shape of the LTE model atmosphere with $T_{\rm eff}$ = 600 kK at the same surface gravity $\log g$ = 9.0 (see Fig. A.1). Rauch's NLTE model 006 was used for comparison. The chemical composition of the LTE and NLTE models is identical. The spectra are binned to a 0.002Å interval within the 10 − 60 Å wavelength range, and the NLTE spectrum is scaled to align directly below the LTE one for the purpose of comparison. Is is clearly seen that the general spectrum shape, including the absorption jumps, is reproduced by the LTE model with a temperature that is ∼ 10% higher than the NLTE one. The same effect is seen when we decrease the gravity of the LTE model, as shown in Fig. A.2. Both spectra have the same $T_{\rm eff}$ = 600 kK but the LTE model has a lower surface gravity, $\log g$ = 8.5, instead of $\log g$ = 9 in the NLTE model.

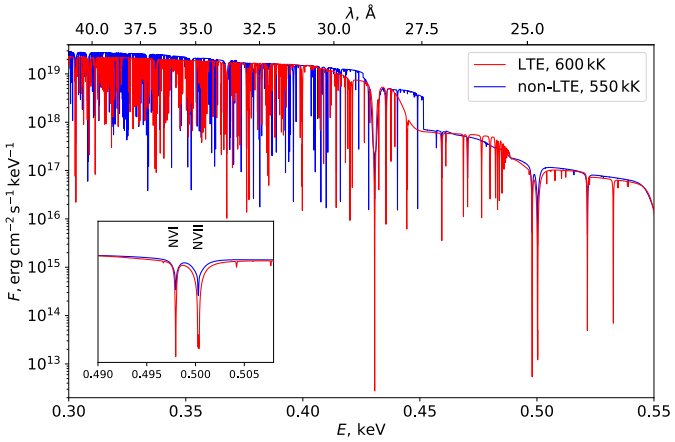

Fig. A.1. Comparison of the model atmospheres spectra computed by our code (in red) and the TMAP non-LTE code (Rauch et al. 2010, in blue). Shown are LTE model with $T_{\rm eff}$ = 600 kK and scaled NLTE model with $T_{\rm eff}$ = 550 kK. The gravity $\log g$ = 9 is fixed. The chemical composition corresponds to model 006 from Rauch's grid. The lower left panel shows in detail the comparison of absorption line profiles.

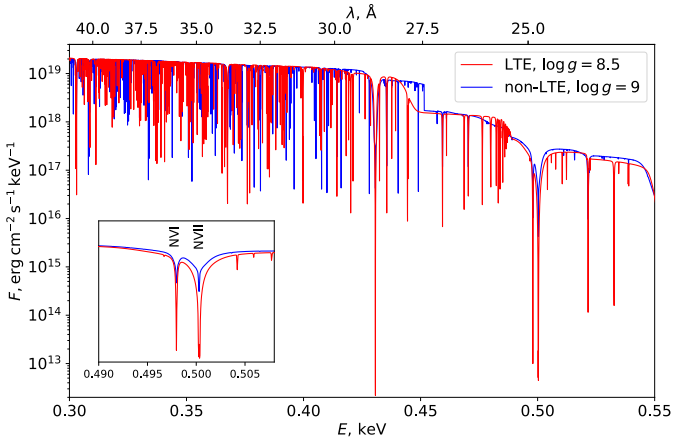

Fig. A.2. Same as in Fig. A.1, but with a fixed $T_{\rm eff}$ = 600 kK and different gravities: $\log g$ = 8.5 for LTE model and $\log g$ = 9 for the NLTE one.

Paper III

III

A. Tavleev, V. Suleimanov, K. Werner, A. Santangelo

"Examining the evolution of the supersoft X-ray source RX J0513.9 − 6951"

Astronomy & Astrophysics, 2025, 694, A73

A&A, 694, A73 (2025)
https://doi.org/10.1051/0004-6361/202453039

Astronomy & Astrophysics

Examining the evolution of the supersoft X-ray source RX J0513.9 – 6951

A. Tavleev*, V. F. Suleimanov, K. Werner, and A. Santangelo

Institut für Astronomie und Astrophysik, Kepler Center for Astro and Particle Physics, Universität Tübingen, Sand 1, 72076 Tübingen, Germany

Received 17 November 2024 / Accepted 1 January 2025

ABSTRACT

Context. Supersoft X-ray sources (SSSs) are thought to be accreting white dwarfs (WDs) in close binary systems, with thermonuclear burning on their surfaces. The SSS RX J0513.9 – 6951 in the Large Magellanic Cloud (LMC) exhibits cyclic variations between optical low and high states, which are anti-correlated with its X-ray flux. This behaviour is believed to be the result of the periodic expansion and contraction of the WD due to variations in the accretion rate in the system.

Aims. We analyse the eight high-resolution XMM and six grating *Chandra* spectra of RX J0513.9 – 6951 with our grid of model atmosphere spectra of hot WDs computed under the assumption of local thermodynamic equilibrium. Our aim is to test a contraction model of the source variability by tracking the evolution of the WD properties.

Methods. We use a recently computed grid of hot WD model atmospheres, spanning a wide range of effective temperatures ($T_{\rm eff}$ = 100−1000 kK in steps of 25 kK) and eight values of surface gravity. The LMC chemical composition of the atmospheres was assumed.

Results. The obtained fitting parameters (effective temperature $T_{\rm eff}$, surface gravity $\log g$, and bolometric luminosity L) evolve on the $T_{\rm eff} - \log g$ and $T_{\rm eff} - L$ planes. This evolution follows the model tracks of WDs with masses of 1.05−1.15 $M_\odot$ and thermonuclear burning on the surface. We show that, when the source has a relatively small photospheric radius and is optically bright, it lies below the stable-burning strip with a relatively low bolometric luminosity. Conversely, the fainter optical states correspond to higher bolometric luminosity and larger photospheric radii of the hot WD. RXJ0513 lies within the stable-burning strip during this state. This means that the optical brightness of the system is lower when the WD is larger, more luminous, and illuminates the accretion disc more effectively. These results contradict the contraction model, which predicts the opposite behaviour of the source. We use a model that assumes that the far UV/soft X-ray flux is reprocessed into the optical band due to multiple scattering in the cloud system above the accretion disc. More significant illumination can lead to rarefying of the cloud slab, thereby reducing the reprocessing efficiency and making the source fainter in the optical band.

Key words. novae, cataclysmic variables – white dwarfs – X-rays: individuals: RX J0513.9 – 6951

1. Introduction

Supersoft X-ray sources (SSSs) represent a sub-class of cataclysmic variable (CV) stars characterised by a high mass-accretion rate of $\sim 10^{-7}\,M_\odot\,{\rm yr}^{-1}$ and (quasi-)steady state thermonuclear burning on the white dwarf (WD) surface (van den Heuvel et al. 1992; Rappaport et al. 1994). CVs are close binary systems composed of a WD primary and a main-sequence or red (sub-)giant companion that fills its Roche lobe. Consequently, matter transfers from the companion to the WD, potentially forming an accretion disc.

The first SSSs were identified in the Magellanic Clouds by the *Einstein* observatory (Long et al. 1981; Seward & Mitchell 1981), and they were later classified as a new type of X-ray source during ROSAT observations (Trümper et al. 1991). These sources are defined by their extremely soft thermal X-ray spectra, with blackbody temperatures ranging from 15−80 eV (150−900 kK) and high luminosities of $\sim 10^{36}-10^{38}$ erg/s, which are comparable to the Eddington luminosity of a solar mass object (Kahabka & van den Heuvel 1997; Greiner 2000). To date, more than 100 SSSs have been identified in approximately 20 external galaxies, the Magellanic Clouds, and our Galaxy (Greiner 2000; Kahabka 2006; Maitra & Haberl 2022).

The luminous transient soft X-ray source RX J0513.9 – 6951 (hereafter RXJ0513) in the Large Magellanic Cloud (LMC) was discovered in the ROSAT All-Sky Survey (Schaeidt et al. 1993; Pakull et al. 1993; Cowley et al. 1993). Optical spectroscopic analysis revealed strong emission lines of H, He II and several higher ionisation emission features with broad wings, indicating the presence of an accretion disc, while the accretor is most likely a WD (Crampton et al. 1996; Southwell et al. 1996). Thanks to the Massive Compact Halo Objects project (MACHO) survey (Alcock et al. 1996), a 3.5 yr light curve of the $V \sim 17^m$ (absolute $M_V \sim -1.5$) optical counterpart of this source was obtained, which revealed recurrent low states (dropping by $\sim 1^m$), which last 20−40 days and repeat every 100−200 days. Moreover, these optical low states are accompanied by X-ray outbursts, so the optical and X-ray states are strictly anti-correlated (Southwell et al. 1996). Such variability is explained by the so-called contraction model (e.g. Reinsch et al. 1996, 2000; Southwell et al. 1996; Hachisu & Kato 2003a,b), which suggests that the observed changes occur due to a change in the mass accretion rate, and therefore, a change in the intensity of thermonuclear burning on the WD surface. High rate of thermonuclear energy release

* Corresponding author; tavleev@astro.uni-tuebingen.de

leads to a significant expansion of a WD photosphere, and the peak in emergent radiation lies outside the observed X-ray band, which makes the source faint in X-ray. At the same time the bolometric luminosity of the expanded WD is high, and it effectively illuminates the accretion disc, resulting in high optical flux due to the reprocessing of the WD radiation. This scenario corresponds to the optically bright and X-ray faint state. On the other hand, a low mass accretion rate causes the WD to shrink, and its outgoing radiation is observed in the soft X-ray band. However, a smaller photospheric radius and decreased WD luminosity make the accretion disc illumination less significant, resulting in faint optical brightness. The origin of the periodicity in the mass accretion rate changes is not completely clear.

Reinsch et al. (2000) proposed a limit-cycle model, where periodic changes in the accretion disc viscosity, driven by irradiation from the WD, could lead to variations in the accretion rate and subsequent changes of the WD photosphere size. In this model, the mass transfer from the companion star to the WD remains constant. Alternatively, Hachisu & Kato (2003a,b) suggested the 'accretion wind evolution' model, in which a self-sustained optically thick wind from the WD impacts the companion star, reducing the mass transfer rate. This diminishes the wind, causing the mass transfer rate to increase again. The behaviour of such a wind modulates the accretion rate onto the WD, resulting in the transitions between high and low optical states. Zhao et al. (2022) tested the contraction model by performing a MESA simulation of the WD accretion process and its subsequent evolution in a binary star with a periodic mass transfer in order to reproduce the observed optical variability of RXJ0513. A WD irradiation of the companion star was proposed to be an origin of the periodic mass transfer.

McGowan et al. (2005) confirmed the contraction model by observing RXJ0513 with the *XMM-Newton* telescope to obtain high-resolution spectra of the object and track the X-ray evolution of the WD. However, interpreting SSS spectra presents significant challenges. While low-resolution spectra can often be described by a blackbody model (as done by McGowan et al. 2005), this approach lacks physical accuracy. In general, blackbody fitting leads to an overestimation of the interstellar neutral hydrogen column density, $N_{\rm H}$, and underestimation of the temperature, resulting in an overestimated luminosity (see e.g. Greiner et al. 1991; Heise et al. 1994). High-resolution spectra of SSSs are considerably more complex, featuring numerous emission and absorption lines.

The spectra of SSSs can be more accurately described by theoretical spectra of hot WD atmospheres. This approach has been applied by numerous authors using both local thermodynamic equilibrium (LTE, e.g. Heise et al. 1994; Ibragimov et al. 2003; Suleimanov & Ibragimov 2003; Burwitz et al. 2007; Swartz et al. 2002), and non-LTE (e.g. Hartmann & Heise 1996; Lanz et al. 2005; Petz et al. 2005; van Rossum 2012; Rauch et al. 2010) assumptions. Non-LTE effects are non-negligible, and non-LTE models are more physically accurate, all else being equal. However, the physical conditions of the radiating regions in SSSs are not entirely clear and may differ significantly from the simplest plane-parallel hydrostatic atmosphere for which non-LTE effects are considered. The uncertainties associated with factors like radiation-driven winds, boundary layers, accretion disc irradiance are likely much more significant than non-LTE effects. Therefore, we believe that LTE models provide comparable accuracy (see Suleimanov et al. 2024; Tavleev et al. 2024) and can be used to analyse the soft X-ray spectra of SSSs. Moreover, LTE computations are much faster, allowing for the calculation of more extensive model grids and the inclusion of a larger number of ions, their excited levels, and a greater number of spectral lines compared to the non-LTE case.

Recently Suleimanov et al. (2024) further refined the LTE approach, including a more extensive set of spectral lines and photoionisation opacities from the excited levels of heavy element ions. They successfully apply a computed set of model atmosphere spectra to the interpretation of grating *Chandra* and *XMM-Newton* spectra of two SSS sources, CAL 83 and RXJ0513; for latter source only one *Chandra* observation was used. Tavleev et al. (2024) utilised the code by Suleimanov et al. (2024) to compute a specific grid of LTE models for analysing the eROSITA and *XMM-Newton* spectra of the nova AT 2018bej, focusing specifically on the chemical composition. It was concluded that LTE model atmospheres can be used to analyse the available X-ray spectra of classical novae during their SSS state.

In this work we analyse the high-resolution XMM and *Chandra* spectra of RXJ0513 using the LTE atmosphere grid calculated by Suleimanov et al. (2024). Our aim is to test the contraction model of the source's variability by tracking the evolution of the WD parameters and comparing them with the optical brightness of the source. The X-ray observations used are described in Sect. 2. We describe the used models atmospheres and the fitting technique in Sect. 3. The results of spectral fitting are presented in Sect. 4, while in Sect. 5 we discuss the possible nature of the obtained evolutionary trends. We conclude and summarise our findings in Sect. 6.

2. Observations

The source was observed by the *Chandra* X-ray observatory using the High Resolution Camera (HRC-S) and the Low Energy Transmission Grating (LETG). A total of six spectra are publicly available in the Chandra Grating-Data Archive and Catalog[1] (TGCat, Huenemoerder et al. 2011), the *Chandra* observation log is presented in Table 1. Below we refer to the observation with ObsID 3503 as the C0 spectrum, while the spectra with ObsIDs 5440 – 5444 are labelled C1 – C5. To increase the signal-to-noise ratio the positive and negative first-order spectra were co-added using the `combine_grating_spectra` task of the Chandra Interactive Analysis of Observations (CIAO, Fruscione et al. 2006; CIAO Development Team 2013) package. For the fitting purposes the spectra were rebinned to at least 30 counts per bin in the 0.21−0.65 keV energy range.

McGowan et al. (2005) published the analysis of *XMM-Newton* observations of the source. The high-resolution spectra, obtained using the Reflection Grating Spectrometer (RGS, den Herder et al. 2001) instrument, are available for eight observations (see Table 2). It should be noted that the observation with ObsID 0151410101 was affected by high solar flaring activity and contains no useful data. All spectra are available in the *XMM-Newton* Science Archive[2], only the first-order spectrum was used without any rebinning. We did not combine the data from RGS1 and RGS2 but fitted them simultaneously. Below we refer to these spectra as X1 – X8.

3. Method

A new grid of hot LTE model atmospheres, recently presented by Suleimanov et al. (2024), was used to analyse the observed spectra. These model spectra were successfully used for the analysis

[1] http://tgcat.mit.edu
[2] http://nxsa.esac.esa.int/nxsa-web

Table 1. *Chandra* HRC-S/LETG observation log of RXJ0513.

	ObsID	Date	MJD	Exp. time, ks
C0	3503	2003 December 24	52997.29	47.65
C1	5440	2005 April 20	53480.80	24.53
C2	5441	2005 April 27	53487.95	25.00
C3	5442	2005 May 03	53493.24	25.50
C4	5443	2005 May 13	53503.82	22.48
C5	5444	2005 May 19	53509.09	24.99

Table 2. *XMM-Newton* observation log of RXJ0513.

	ObsID	Date	MJD	Exp. time [a]
	0151410101	2004 April 28	53123.74	0.0 [b]
X1	0151412101	2004 May 02	53127.08	16.84/16.83
X2	0151412201	2004 May 05	53130.81	17.72/17.70
X3	0151412301	2004 May 09	53134.91	17.64/17.61
X4	0151412401	2004 May 12	53137.69	25.62/25.62
X5	0151412501	2004 May 16	53141.06	13.84/13.82
X6	0151412601	2004 May 18	53143.35	13.84/13.83
X7	0151412701	2004 May 26	53151.24	18.03/18.03
X8	0151412801	2004 May 28	53153.27	15.83/15.83

Notes. [a]Exposure time in ks for RGS1 and RGS2 instrument, respectively; [b]The first observation has very high background and does not contain useful data.

of the classical SSS CAL 83 and one of the *Chandra* spectra of RXJ0513 (spectrum C3).

The models were computed using a code based on Kurucz's ATLAS (Kurucz 1970), which was modified for high temperatures and high densities (Ibragimov et al. 2003; Suleimanov et al. 2006, 2015). The models account for the15 most abundant chemical elements from H to Ni and about 20,000 lines from CHIANTI, Version 3.0, atomic database (Dere et al. 1997). The main parameters of the model are the effective temperature $T_{\rm eff}$ and the gravity parameter $\Delta \log g = \log g - \log g_{\rm Edd}$, which indicates the distance of model from the Eddington limit (see details in Suleimanov et al. 2024):

$$\log g_{\rm Edd} = \log(\sigma_{\rm e}\sigma_{\rm SB}T_{\rm eff}^4/c) = 4.818 + 4\log(T_{\rm eff}/10^5\,{\rm K}), \quad (1)$$

were $\sigma_{\rm e}$, $\sigma_{\rm SB}$ and c are the Thomson cross-section for the electron, Stefan-Boltzmann constant, and the speed of light, respectively.

The grid was computed for $T_{\rm eff}$ in the range of 100−1000 kK in steps of 25 kK. The $\Delta \log g$ parameter has eight values: 0.1, 0.2, 0.4, 0.6, 1.0, 1.4, 1.8 and 2.2. The grid was calculated for three chemical compositions; we used the LMC composition, where the hydrogen-helium mix is set to solar, while the abundance of heavy elements is set to half-solar ($A = 0.5$). The model grid is available[3] as an XSPEC[4] (Arnaud 1996; Arnaud et al. 1999) table.

All the observed X-ray spectra were fitted using the models described above. We used the WD mass M and radius R as free parameters instead of $\Delta \log g$ and normalisation parameter. A uniform prior distribution was set for $T_{\rm eff}$, M (in range 0.3−1.4 $M_\odot$), and R (in range (2−20) × 10^8 cm). We note that the strict upper limit was set for the WD mass. Another limitation applied is based on the fact that the WD radius must be greater than the cold WD radius $R_{\rm cold}$ at such a mass (Nauenberg 1972). The Tübingen-Boulder ISM model `tbabs` (Wilms et al. 2000) was employed to account for absorption, with a uniform prior distribution set for the hydrogen column density $N_{\rm H}$ in the range of (1−10) × 10^{20} cm^{-2}.

To find the best-fitting parameters and estimate their uncertainties, we used the following technique. First, we employed the Bayesian approach. The analysis was conducted using the software Bayesian X-ray Analysis (BXA, Buchner et al. 2014; Buchner 2016a), which connects the nested sampling package UltraNest[5] (Buchner 2021, 2016b) with XSPEC[6] (Arnaud 1996; Arnaud et al. 1999). The nested sampling Monte Carlo algorithm MLFriends (Buchner et al. 2014; Buchner 2019) was used to obtain posterior probability distributions and the Bayesian evidence.

The usage of C-statistics (Cash 1979) is preferable instead of the χ^2-statistics for low-count spectra. We used its XSPEC implementation `cstat` as a likelihood in order to determine the best-fit parameters. The parameter uncertainties were derived from the 0.16 and 0.84 quantiles of the posterior distribution (which corresponds to 68% confidence level, CL).

However, we consider these statistical errors to be significantly underestimated. To obtain more realistic uncertainties, we added a systematic error to the spectra such that the reduced χ^2_ν approached unity, after which we re-estimated the parameter confidence intervals. We then combined the statistical confidence intervals (derived using `cstat`) with the systematic ones (calculated using χ^2). The final parameter value was taken as the mean of the combined confidence interval.

Due to such a technique of estimating the model parameters and its confidence intervals in the tables below we do not provide the statistics value or the goodness-of-fit estimating criterion (like χ^2_ν).

4. Results

4.1. Hydrogen column density

First, we fitted the observed spectra using the interstellar absorption column density $N_{\rm H}$ as a free parameter. It is found that the absorption parameter obtained differs significantly across the various spectra. For the *XMM-Newton* spectra, $N_{\rm H}$ is contained within the range (1−3.5) × 10^{20} cm^{-2}, while for the *Chandra* spectra $N_{\rm H}$ lies within (3.7−5.4) × 10^{20} cm^{-2}. All obtained values are lower than the average Galactic absorption column in the direction of the source, which is (6.3 ± 0.8) × 10^{20} cm^{-2} based on the extinction/absorption maps presented in Doroshenko (2024)[7].

The fitting parameters are crucially depended on the obtained absorption parameter $N_{\rm H}$ (see e.g. Suleimanov et al. 2024). Consequently, we adopted $N_{\rm H}$ = (5.5 ± 1) × 10^{20} cm^{-2}, as obtained by Gänsicke et al. (1998) from the analysis of the UV spectra of the source, and we use this value further. It should be noted that this issue also arises when fitting soft X-ray spectra of other SSSs with atmosphere models (see e.g. Rauch et al. 2010; Suleimanov et al. 2024; Tavleev et al. 2024).

[3] https://github.com/HEASARC/xspec_localmodels/tree/master/sss_atm
[4] https://heasarc.gsfc.nasa.gov/docs/xanadu/xspec/
[5] https://johannesbuchner.github.io/UltraNest/
[6] https://heasarc.gsfc.nasa.gov/docs/xanadu/xspec/
[7] http://astro.uni-tuebingen.de/nh3d/nhtool

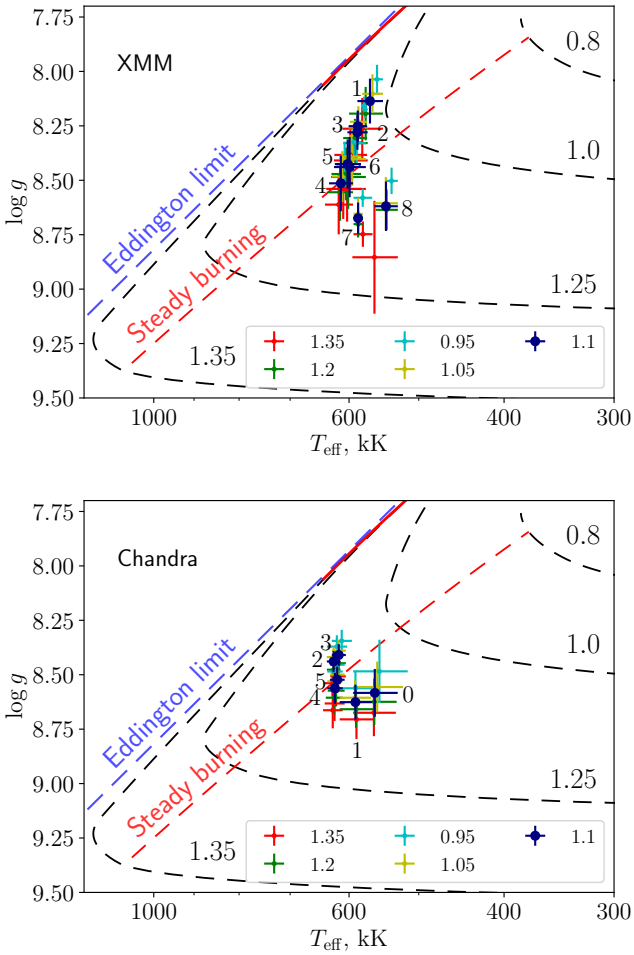

Fig. 1. Positions of the source in the $T_{\rm eff} - \log g$ plane according to different *XMM-Newton* (upper panel) and *Chandra* (lower panel) observations (see Tables 3 and 4). The WD mass was fixed, and different colours indicate different masses from 0.95 to 1.35 $M_\odot$. For clarity, only a portion of the mass range is shown. The fits with $M = 1.1\,M_\odot$ are additionally indicated by the increased marker size. Model dependencies for various WD masses, taken from Nomoto et al. (2007), are shown by black dashed curves. The numbers at the curves indicate WD masses (in solar masses). The lower boundary of the stable thermonuclear burning band is shown by the dashed red line. The Eddington limit for solar H/He abundances is shown by the blue dashed line. The numbers denote the spectrum number (see Sect. 2).

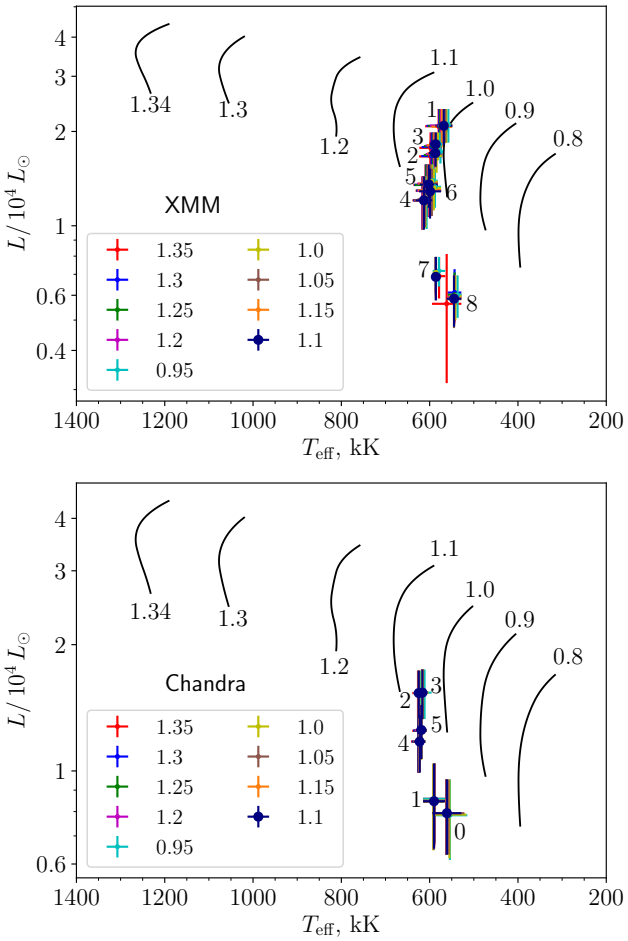

Fig. 2. Positions of the source in the $T_{\rm eff} - L$ plane according to different *XMM-Newton* (upper panel) and *Chandra* (lower panel) observations. The WD mass was fixed, and different colours indicate different masses from 0.95 to 1.35 $M_\odot$. The fits with $M = 1.1\,M_\odot$ are additionally indicated by the increased marker size. Model dependencies were taken from Wolf et al. (2013). Only the model curves with steady-state thermonuclear burning are shown. The numbers denote the spectrum number (see Sect. 2).

4.2. WD mass estimation

The obtained values of the WD mass vary significantly (from 0.8 to 1.38 $M_\odot$ for the different observations), if we consider the mass as a free parameter. Moreover, the fits with higher masses yield a WD radius close to the lower limit for WD radii. In fact, this lower limit is about 3000 km, which appears to be an incorrect radius for the WD in RXJ0513. This means that we cannot accurately determine the WD mass using spectral fitting alone. On the other hand, the obtained $\log g$ and $T_{\rm eff}$ values do not vary significantly. Therefore, we apply an alternative approach to estimate the WD mass, based on comparing the obtained $\log g$, $T_{\rm eff}$, and bolometric luminosity L for each observation with model predictions for WDs with thermonuclear burning on their surface. This approach has been successfully used previously (Suleimanov et al. 2024; Tavleev et al. 2024).

We fitted all the spectra using nine fixed WD mass values from 0.95 to 1.35 $M_\odot$ in steps of 0.05 $M_\odot$ and then compared the obtained results with theoretical predictions. Namely, we put the obtained fit values on the theoretical $T_{\rm eff} - \log g$ and $T_{\rm eff} - L$ dependencies, computed for different WD masses with hydrogen-rich envelopes with thermonuclear burning by Nomoto et al. (2007) and Wolf et al. (2013). The results obtained are shown in Figs. 1 and 2. All values obtained from the fits lie within the mass range of 1.0–1.15 $M_\odot$. Eventually, we consider $M = 1.1\,M_\odot$ as the correct WD mass (with uncertainty about 0.1 $M_\odot$), and the parameters corresponding to this WD mass are indicated in Figs. 1 and 2 by an increased marker size. It should be noted that in the previous paper (Suleimanov et al. 2024) we estimated the WD mass in the source as $>1.15\,M_\odot$, although only one *Chandra* observation (C3) was used.

4.3. Evolution of RXJ0513

Tables 3 and 4 present the final results of our analysis, while Figs. 3 and 4 show the comparison between the observed and model spectra. The temperatures $T_{\rm eff}$ derived from our LTE models are higher than those found by McGowan et al. (2005), who used a blackbody model to fit the EPIC-PN spectra of RXJ0513.

Table 3. Spectral parameters of the LTE and blackbody model fit for the *Chandra* spectra.

	$T_{\rm eff}$ kK	R [(a)] km	$\log g$	L 10^{37} erg s^{-1}	$T_{\rm eff}^{\rm bb}$ kK	$R_{\rm bb}$ [(a)] km	$L_{\rm bb}$ 10^{37} erg s^{-1}
C0	561 ± 33	6297 ± 660	8.58 ± 0.11	3.0 ± 0.6	559 ± 24	7776 ± 984	4.3 ± 1.2
C1	590 ± 25	5993 ± 550	8.63 ± 0.08	3.2 ± 0.7	589 ± 24	7159 ± 970	4.4 ± 1.4
C2	625 ± 11	7351 ± 401	8.44 ± 0.05	5.9 ± 0.8	706 ± 18	6121 ± 417	6.7 ± 1.1
C3	616 ± 11	7569 ± 432	8.41 ± 0.05	5.9 ± 0.8	702 ± 25	6191 ± 519	6.8 ± 1.2
C4	623 ± 13	6370 ± 544	8.56 ± 0.07	4.5 ± 0.7	662 ± 17	6322 ± 533	5.5 ± 1.1
C5	619 ± 12	6683 ± 512	8.52 ± 0.06	4.8 ± 0.7	675 ± 23	6114 ± 519	5.7 ± 1.1

Notes. [(a)]The distance to the LMC is assumed to be 50 kpc (Pietrzyński et al. 2019); $N_{\rm H} = 5.5 \times 10^{20}$ cm^{-2} and $M = 1.1\ M_{\odot}$ are fixed for all of the fits.

Table 4. Spectral parameters of the LTE and blackbody model fit for the *XMM-Newton* spectra.

	$T_{\rm eff}$ kK	R [(a)] km	$\log g$	L 10^{37} erg s^{-1}	$T_{\rm eff}^{\rm bb}$ kK	$R_{\rm bb}$ [(a)] km	$L_{\rm bb}$ 10^{37} erg s^{-1}
X1	568 ± 19	10 324 ± 1150	8.14 ± 0.10	8.0 ± 1.1	553 ± 16	17 765 ± 2227	21.3 ± 3.5
X2	587 ± 16	8775 ± 797	8.28 ± 0.08	6.5 ± 0.6	537 ± 16	18 575 ± 2615	20.7 ± 4.0
X3	586 ± 14	9065 ± 727	8.25 ± 0.07	7.0 ± 0.6	553 ± 16	16 961 ± 2178	19.4 ± 3.5
X4	613 ± 19	6748 ± 980	8.51 ± 0.13	4.6 ± 0.9	519 ± 8	17 984 ± 1512	17.0 ± 2.8
X5	602 ± 21	7417 ± 923	8.43 ± 0.11	5.2 ± 0.8	522 ± 18	18 680 ± 3012	18.7 ± 4.3
X6	599 ± 25	7348 ± 1135	8.44 ± 0.14	4.9 ± 0.9	502 ± 19	21 202 ± 3744	20.7 ± 5.2
X7	586 ± 7	5562 ± 441	8.67 ± 0.07	2.6 ± 0.4	439 ± 24	27 610 ± 8135	20.7 ± 9.0
X8	545 ± 17	6007 ± 685	8.62 ± 0.11	2.2 ± 0.4	413 ± 31	29 897 ± 9880	18.7 ± 8.5

Notes. [(a)]The distance to the LMC is assumed to be 50 kpc (Pietrzyński et al. 2019); $N_{\rm H} = 5.5 \times 10^{20}$ cm^{-2} and $M = 1.1\ M_{\odot}$ are fixed for all of the fits.

In contrast, the radii obtained are much smaller than the values determined by the blackbody fits. It should be noted that we fixed the hydrogen column density $N_{\rm H}$ at 5.5×10^{20}, whereas McGowan et al. (2005) used a value of 6.2×10^{20}.

We can now examine the X-ray evolution of RXJ0513 and compare the results with the optical brightness of the system. The optical light curve is presented in Fig. 5, while for the optical data description we refer to McGowan et al. (2005) and Burwitz et al. (2008). The observational dates of the investigated X-ray spectra are also marked in the figure. They cover three optical low states, corresponding to the C0, X1-8, and C1-5 observational sequences. Spectra X1-6 correspond to the optical low state of the source, while X7-8 depict an increase in optical flux, marking the transition to the optical high state. Similarly, during spectrum C1, the transition to the optical low state begins; the source remains optically faint during C2-3, and the transition to the optical high state occurs during C4-5.

The changes in the WD parameters, obtained from fitting the X-ray spectra, with time are shown in Fig. 6. For the *XMM-Newton* spectra, it is evident that initially the temperature increases, accompanied by a decrease in both the radius and luminosity. Later, the temperature starts to decrease, and during the transition from low to high optical state, temperature, radius, and luminosity all approach their minimum values. For the *Chandra* spectra, temperature, radius, and luminosity all increase over time during the transition from the high to low optical state. Later, during the transition from the low to high optical state, the temperature remains stable, while radius and luminosity decrease to values comparable the initial ones.

The results of the blackbody fitting are also shown in Fig. 6. The blackbody fit parameters for the *Chandra* observations roughly correspond to those from the model atmosphere fits with slightly overestimated bolometric luminosities, although the radii differ rather randomly. In contrast, the blackbody fit parameters from the *XMM-Newton* observations differ more significantly from the atmosphere model fits, yielding radii and luminosities that are several times larger. Overall, it can be stated that the blackbody fits are unsuitable for analysing the *XMM-Newton* spectra of SSSs.

Fig. 7 illustrates the relationships between the WD parameters, obtained using the model atmosphere spectra, and the optical brightness of RXJ0513. One can clearly see (especially for the *Chandra* spectra, where the Pearson correlation coefficient is close to unity) the correlation between radius (and bolometric luminosity) and the optical brightness of RXJ0513 – the larger the WD (and the bolometric luminosity) the lower the optical brightness.

By comparing the position of the source on the $T_{\rm eff} - \log g$ diagram, obtained during the different *XMM-Newton* observations, with theoretical tracks (see Fig. 1) we conclude that when RXJ0513 is optically bright (in observations X7-X8), it is situated below the steady-burning strip. This means that the nuclear burning on the WD's surface stops, and the WD begins to cool, when its optical brightness is high. And vice versa, the source undergoes steady burning when it is faint in the optical band.

The same conclusion is correct for *Chandra* observations. The source is located in the stable-burning strip when it is optically bright (observations C2, C3 and C0). During the other observations, RXJ513 is optically fainter and it is situated above or at the boundary of the steady-burning strip (see Fig. 1).

As shown in Fig. 1, the higher the fixed WD mass, the higher the surface gravity and the effective temperature of the WD. This means that the positions of more massive WDs move towards

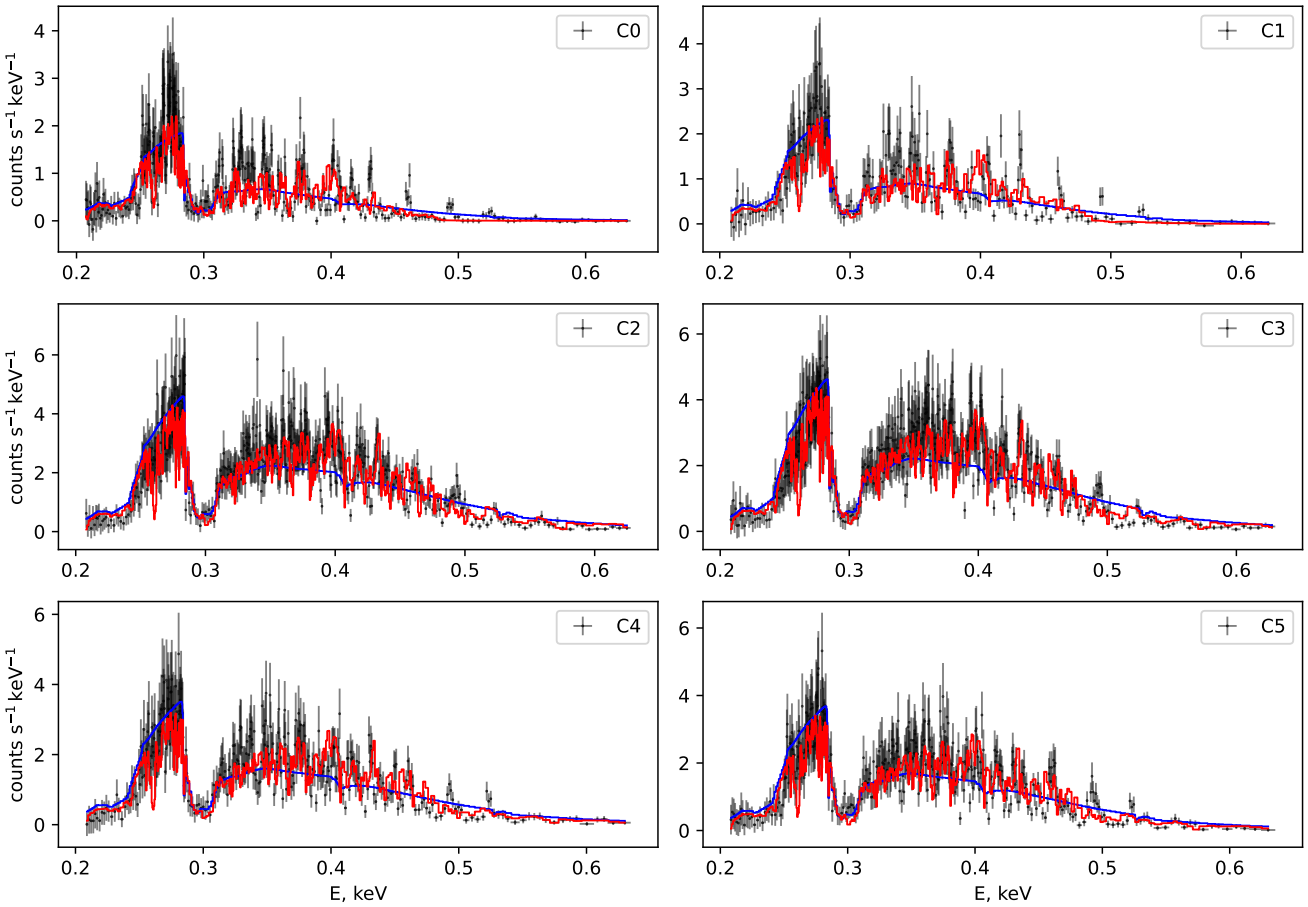

Fig. 3. *Chandra* spectra of RXJ0513 with the best-fit LTE models (in red). The absorbed blackbody models are also shown (in blue). The obtained model parameters are listed in Table 3. The hydrogen column density is fixed at $N_{\rm H} = 5.5 \times 10^{20}$ cm^{-2}, and the mass is set at $M = 1.1\,M_{\odot}$.

below the steady-burning region in the $T_{\rm eff} - \log g$ plane. While for the *XMM-Newton* spectra our conclusions about steadiness of the source on this plane hold for the entire mass range considered, all the positions obtained using the *Chandra* observations lie below the steady-burning limit when $M \geq 1.3\,M_{\odot}$.

Modelling the *XMM-Newton* spectra with blackbody and fixed $N_{\rm H}$ shows a clear decrease in $T_{\rm eff}$ and increase in radius, as shown in Fig. 6 (left panels, in orange) and Table 4. McGowan et al. (2005) obtained the similar result for the EPIC-PN spectra of *XMM-Newton*. This behaviour of the source does not correspond to the results obtained using the model atmosphere spectra. Moreover, the obtained radii and luminosities are significantly larger even at a fixed $N_{\rm H}$. The blackbody fit for the *Chandra* observations aligns more closely with the model atmosphere results. Fixing the column density at $N_{\rm H} = 6.2 \times 10^{20}$, the value found by McGowan et al. (2005), does not change the result significantly. From a statistical point of view, this $N_{\rm H}$ value is less likely. The theoretical tracks of WD for all spectra shift slightly towards lower temperatures and gravities (upwards and to the right in Fig. 1), but the overall stability characteristics remain almost unchanged, as does the evolution over time.

5. Discussion

The observed anti-correlation between optical and soft X-ray fluxes in RXJ0513 is usually explained by the so-called contraction model (e.g. Reinsch et al. 1996, 2000; Southwell et al. 1996; Hachisu & Kato 2003a,b). According to this model, the mass accretion rate $\dot{M}$ is relatively low during the X-ray bright state, and the nuclear burning rate in the envelope is close to the steady-burning boundary. This state of the source corresponds to an almost minimal radius of the WD photosphere, with the highest effective temperature and a relatively low bolometric luminosity. When $\dot{M}$ increases, the WD inflates and the bolometric luminosity slightly increases, while the effective temperature drops. The decrease in effective temperature suggests that the peak of the spectral energy distribution shifts towards lower photon energies, and a smaller fraction of the emitted spectrum falls within the observed soft X-ray band. Therefore, the increase in the WD photosphere radius at an almost constant bolometric luminosity leads to a decrease in the observed soft X-ray flux. Thus, within the framework of the contraction model, the low X-ray flux corresponds to a high mass accretion rate, a large WD radius and a high bolometric luminosity. Conversely, the bright X-ray state is associated with a hotter WD with a relatively small photospheric radius and a lower bolometric luminosity.

In the considered model the optical flux is produced by accretion disc illumination and reprocessing of hard radiation into the optical band. A colder WD with an expanded photosphere illuminates the accretion disc more significantly, meaning that the faint X-ray state should correspond to a high optical state. Conversely, a hotter WD with a deflated photosphere illuminates the accretion disc less effectively, so the low optical state corresponds to the bright X-ray state, leading to the observed anti-correlation between optical and soft X-ray fluxes from the source. However, our results contradict this model. We

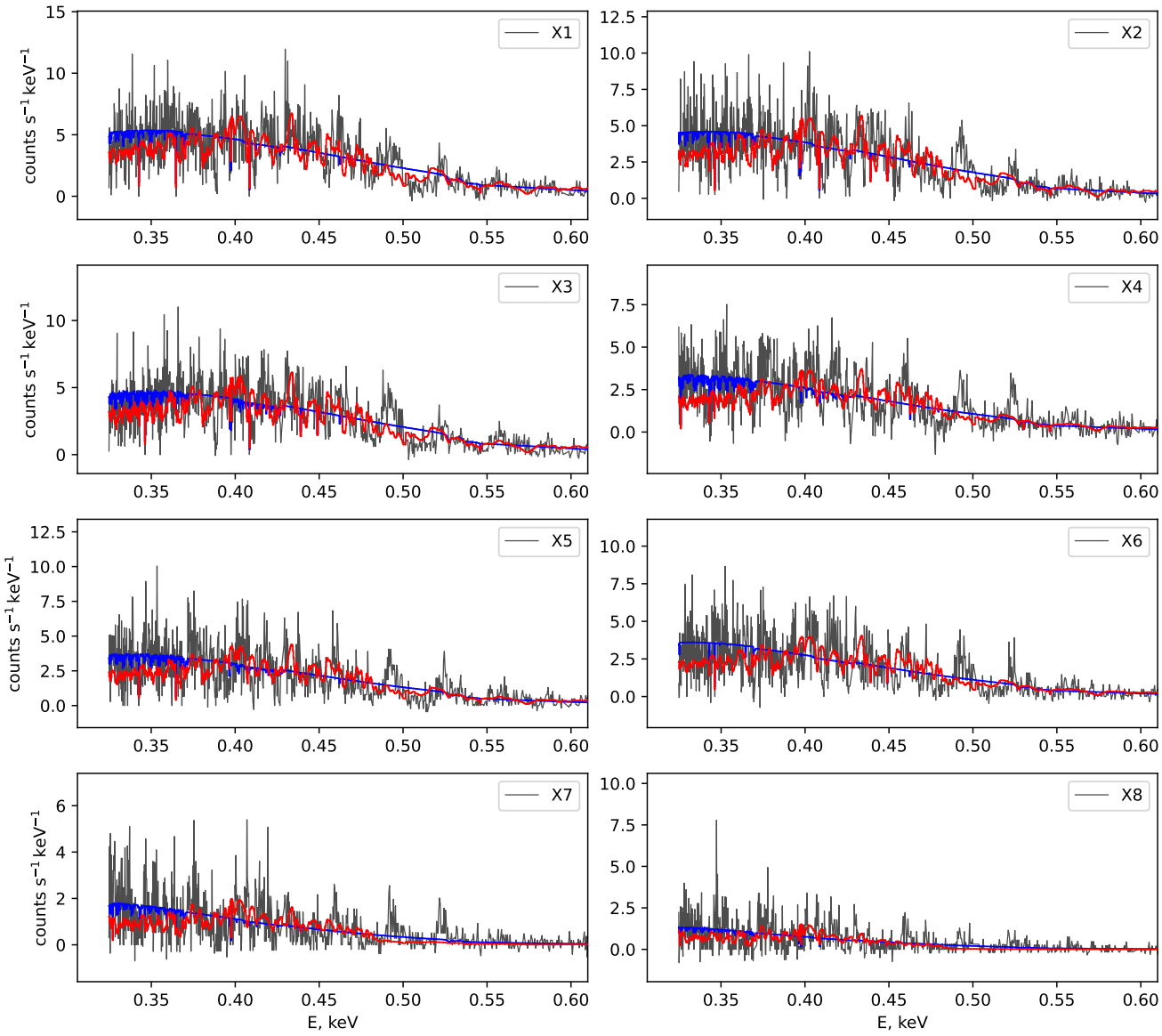

Fig. 4. Same as in Fig. 3, but for *XMM-Newton* observations, RGS1 instrument. Only every second count in the observational spectra is shown for clarity.

show in Fig. 7 that the bright optical state of RXJ0513 corresponds to a low X-ray luminosity, during which the source lies below the stable-burning strip on the $T_{\rm eff} - \log g$ plane (see Fig. 1).

The found contradiction could be explained if we take into account the effects of thermalisation of hard radiation and its re-emission in the optical part of the spectrum. The disc photosphere itself transforms the external soft X-ray radiation into the optical band very inefficiently. The reprocessing efficiency for soft X-rays and far UV radiation in irradiated accretion disc photospheres in SSSs is low ($\eta \sim 0.05{-}0.1$, $F_{\rm opt} = \eta F_{\rm soft\,X-ray}$, see e.g. Suleimanov et al. 1999). The opacity of the upper atmospheric layers in soft X-ray is so high that the irradiated flux is absorbed before reaching the optical flux formation depth. The absorbed flux is then re-radiated mainly in far UV spectral lines.

Reprocessing efficiency can increase to acceptable values of $\eta \sim 0.3{-}0.5$ if we assume a system of optically thick (in soft X-ray) clouds above the disc. In this case, the total reprocessing efficiency rises due to multiple scattering of soft X-ray and far UV radiation between clouds (Suleimanov et al. 2003). Figure 8 presents a qualitative illustration of the proposed model. The value of η depends on the effective optical depth of the cloud slab (Suleimanov et al. 2003),

$$\tau_{\rm eff} \approx \pi R_{\rm cl}^2 N_{\rm cl} L, \qquad (2)$$

where $R_{\rm cl}$ is the cloud size, $N_{\rm cl}$ is the cloud number density, and L is the geometrical thickness of the cloud slab. The reprocessing efficiency reaches the maximum at $\tau_{\rm eff} \approx 1{-}10$.

The nature of these hypothetical clouds is not known. Schandl et al. (1997) proposed that the clouds or blobs could be a 'spray' resulting from the interaction between the accreting gas stream and the outer boundary of the accretion disc. However, clouds formed due to the thermal instability of the matter illuminated by photoionising radiation are more likely (see e.g. Jimenez-Garate et al. 2002). Thus, the changes in the optical flux of RXJ0513 could be explained by assuming that thermal instability conditions depend on the state of the WD photo-

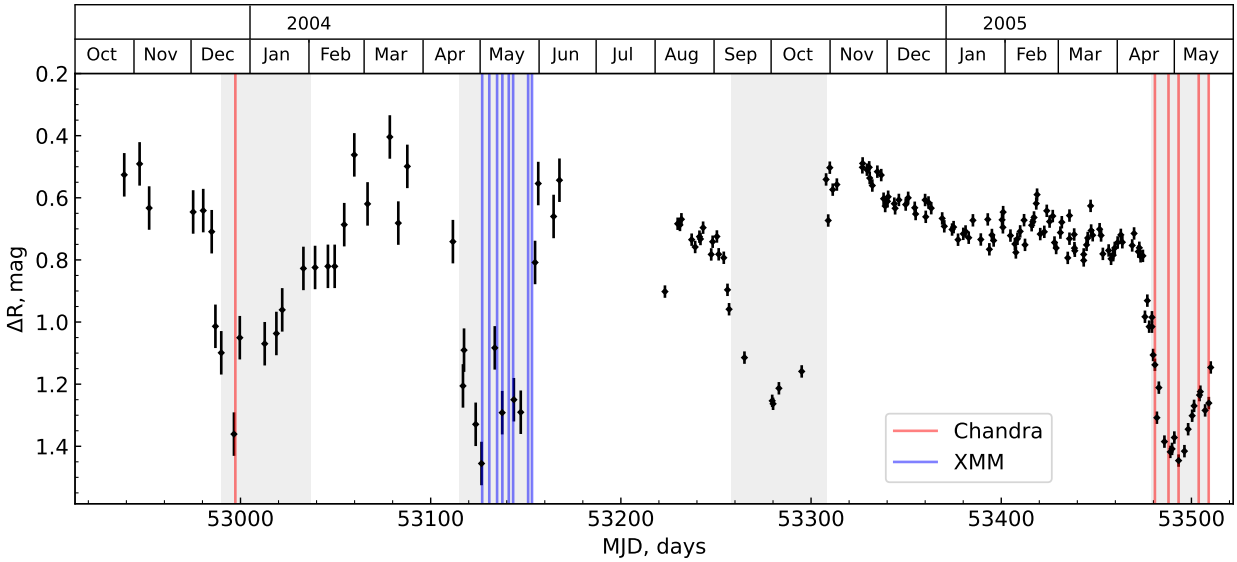

Fig. 5. Optical monitoring of RX J0513.9 − 6951, differential magnitudes in the R-filter, obtained by McGowan et al. (2005) and Burwitz et al. (2008). The times of the observed optical low states are shaded in grey. The dates of X-ray *Chandra* and *XMM-Newton* observations are shown in red and blue.

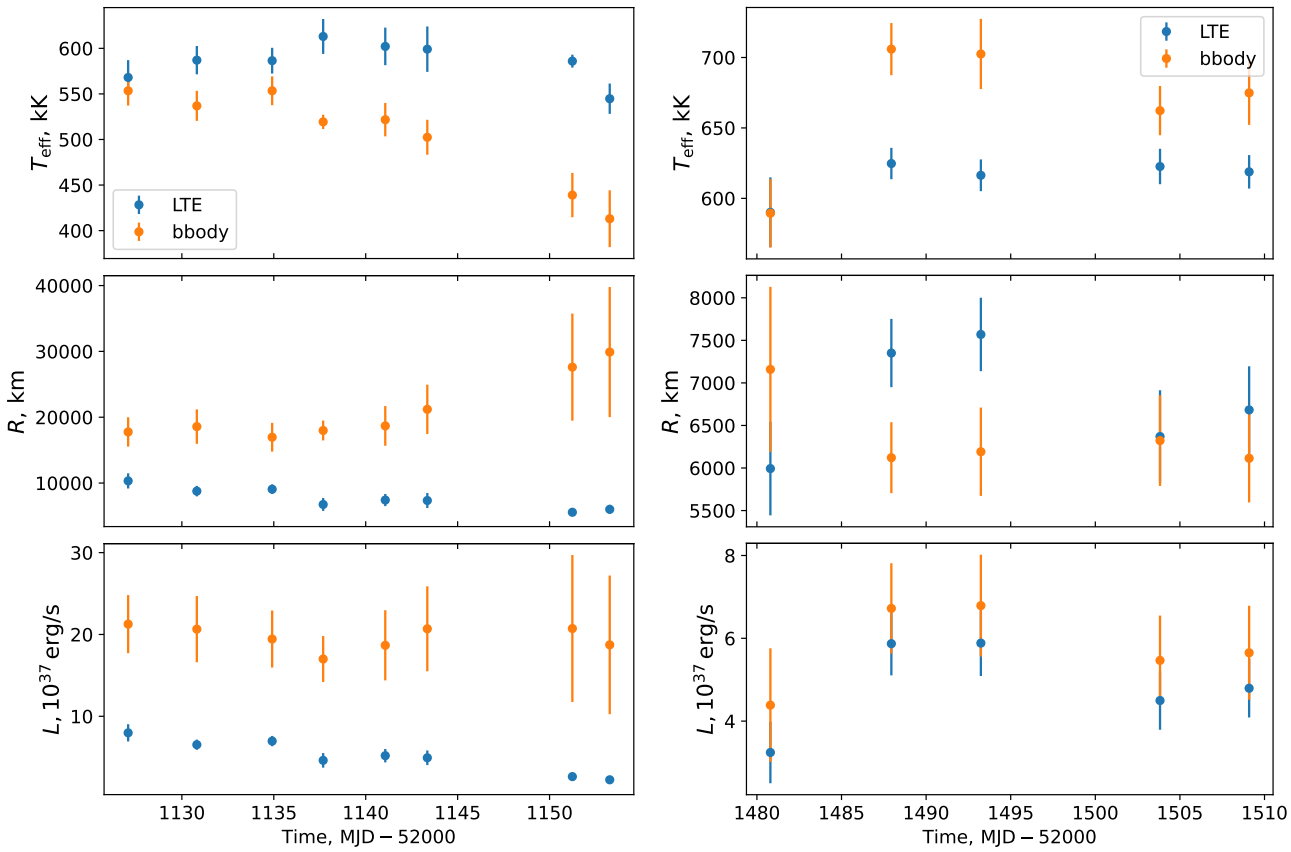

Fig. 6. Evolution of temperature, radius, and luminosity of the WD in RXJ0513 over time during the *XMM-Newton* (left panels) and *Chandra* (right panels) observations. Results are shown for both the model atmosphere fit and the blackbody fit. The WD mass is fixed, $M = 1.1\,M_{\odot}$.

sphere. Namely, a relatively small and low luminous WD photosphere provides better conditions for cloud formation. Consequently, the effective optical thickness of the cloud slab increases and we observe the bright optical state of the source, accompanied by the faint X-ray flux. Moreover, the cloud slab might even become so geometrically thick that it obscures the entire X-ray source. And vice versa, a luminous WD with an expanded photosphere evaporates the clouds, reducing $\tau_{\rm eff}$, and thereby decreasing reprocessing efficiency. Both hypothetical states are illustrated in Fig. 8.

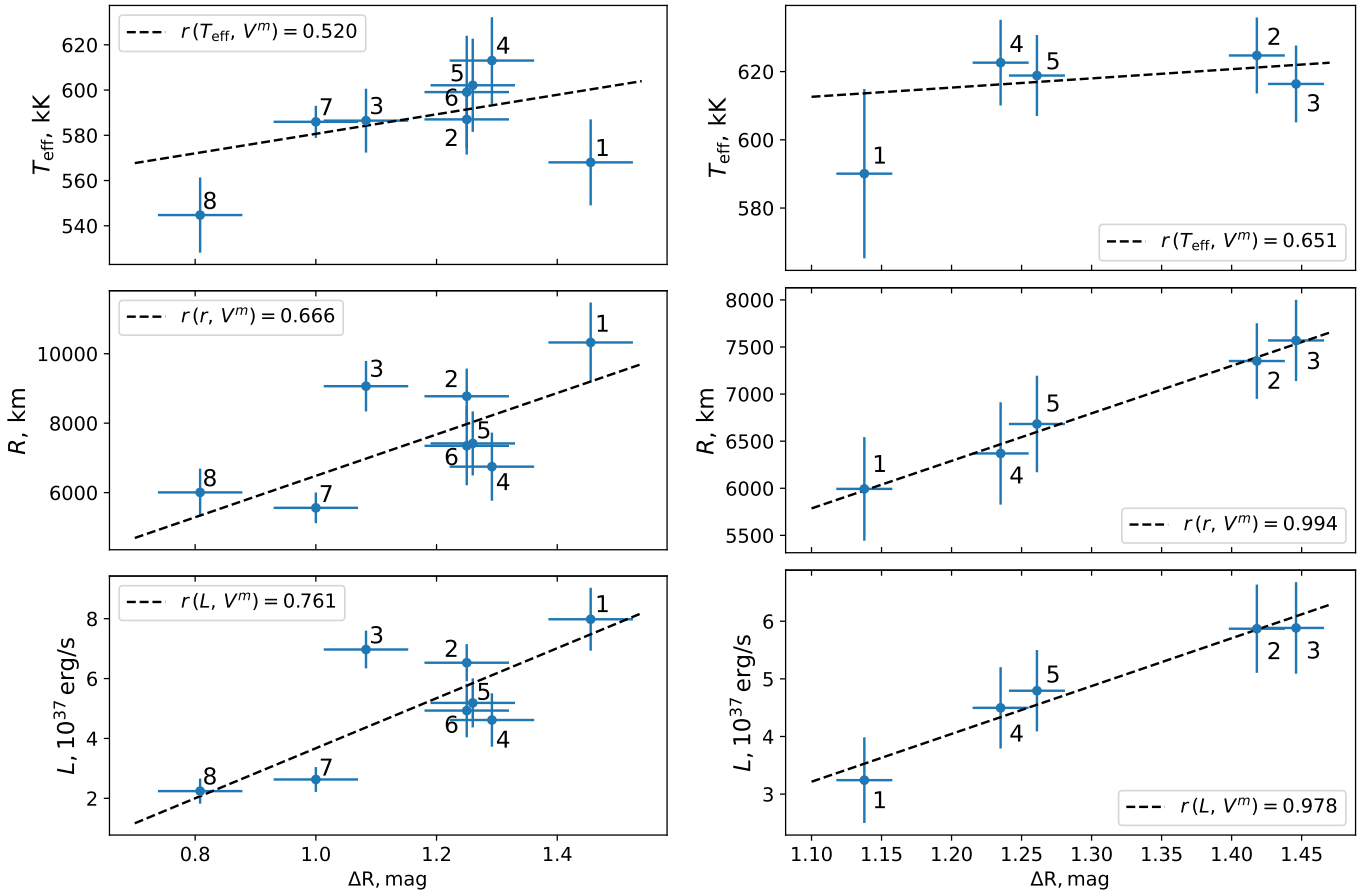

Fig. 7. Temperature, radius, and bolometric luminosity of the WD in RXJ0513 versus the optical brightness of the source for the *XMM-Newton* (left panels) and *Chandra* (right panels) spectra. The numbers denote the spectrum number (see Sect. 2). The linear approximation as well as the Pearson correlation coefficients between the optical flux and WD parameters are also shown.

6. Conclusions

In this work, we performed a spectral analysis of the supersoft X-ray source RX J0513.9 − 6951, which was observed in X-rays by the *Chandra* and *XMM-Newton* telescopes during its optically low states, when the source exhibits maximum X-ray brightness. To describe the spectra we used a grid of the high-gravity hot LTE model atmospheres, calculated by Suleimanov et al. (2024). The grid was computed for $T_{\rm eff}$ in the range of 100 − 1000 kK in steps of 25 kK. The $\Delta \log g = \log g - \log g_{\rm Edd}$ parameter has eight values: 0.1, 0.2, 0.4, 0.6, 1.0, 1.4, 1.8 and 2.2. We adopted the LMC composition, with the hydrogen-helium mix set to solar and the abundance of heavy elements set to half-solar ($A = 0.5$).

We performed two joint fits of the *XMM-Newton* and *Chandra* spectra with different values of a common WD mass parameter and then compared the results with theoretical $T_{\rm eff} - \log g$ and $T_{\rm eff} - L$ model curves. The fit positions correspond to $M = 1.1 \pm 0.1\, M_\odot$, which we adopt as the obtained WD mass.

Our analysis reveal the evolution of the WD in RXJ0513: the photospheric radius of the WD and its bolometric luminosity increase as the optical flux decreases, and vice versa. This conclusion is based on studying the source's position on the $T_{\rm eff} - \log g$ plane, where the source lies below the stable-burning strip when it is optically bright. As its optical brightness decreases, RXJ0513 shifts towards the stable-burning strip. We also find the correlation between the photospheric WD radius and the source magnitude in *R*-band, as well as between the bolometric luminosity and *R*-band magnitude. These results contradict the predictions of the contraction model, which is commonly used to explain the observed anti-correlation between soft X-ray and optical fluxes (see e.g. Reinsch et al. 1996, 2000; Southwell et al. 1996). This model predicts the opposite correlation between the WD photospheric radius and its optical brightness.

We propose an alternative model of RXJ0513 periodicity based on the reprocessing model suggested by Suleimanov et al. (2003). In this model, efficient reprocessing of soft X-ray flux illuminating the accretion disc is achieved through multiple scattering of hard radiation in a system of optically thick (in the soft X-ray band) gaseous blobs/clouds above the accretion disc, embedded in a disc wind or corona. These clouds may arise due to thermal instability in the matter above the disc, irradiated by far UV/soft X-ray flux.

We suggest that the cloud system becomes highly saturated when the WD has relatively low luminosity and a small radius, comparable to that of a cold WD. In this case, a cloud slab provides reprocessing efficiency high enough to transform the soft X-ray/far UV flux into the optical band. This picture is proposed to represent the RXJ0513 state with low X-ray flux and high optical brightness. Alternatively, a luminous WD with an expanded photosphere is likely less favourable for clouds formation. The cloud slab becomes rarefied, and the reprocessing efficiency decreases. This picture corresponds to the source's low optical state, accompanied by high X-ray flux.

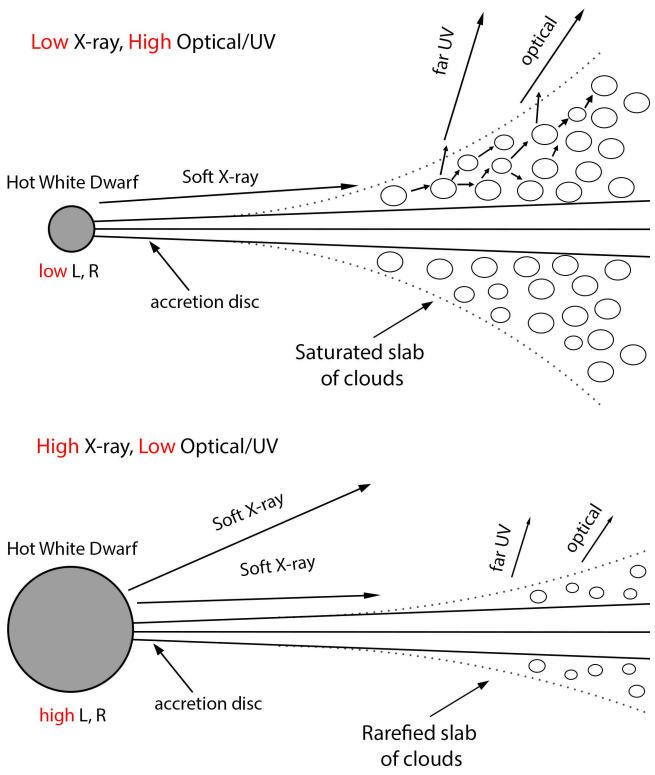

Fig. 8. Qualitative picture of the proposed high and low optical states. Shown are the WD, the accretion disc, and blobs or clouds above the disc. Upper panel – high optical state; the low luminous WD is compact, and its X-ray emission is effectively reprocessed into optical light due to multiple scattering between clouds. Lower panel – low optical state; the luminous WD with an expanded photosphere evaporates most of clouds decreasing the reprocessing efficiency and reducing the optical flux.

This suggested toy model qualitatively explains the observed properties of RXJ0513 and may open a window for observational investigations of thermal instability in plasma irradiated by hard UV/soft X-ray flux.

Acknowledgements. This work was supported by the *Deutsche Forschungsgemeinschaft* under grants WE1312/56–1 (AT) and WE1312/59–1 (VFS).

References

Alcock, C., Allsman, R. A., Alves, D., et al. 1996, MNRAS, 280, L49
Arnaud, K. A. 1996, in Astronomical Data Analysis Software and Systems V, eds. G. H. Jacoby, & J. Barnes, ASP Conf. Ser., 101, 17
Arnaud, K., Dorman, B., & Gordon, C. 1999, XSPEC: An X-ray spectral fitting package, Astrophysics Source Code Library [record ascl:9910.005]
Buchner, J. 2016a, BXA: Bayesian X-ray Analysis, Astrophysics Source Code Library [record ascl:1610.011]
Buchner, J. 2016b, UltraNest: Pythonic Nested Sampling Development Framework and UltraNest, Astrophysics Source Code Library [record ascl:1611.001]
Buchner, J. 2019, PASP, 131, 108005
Buchner, J. 2021, J. Open Source Software, 6, 3001
Buchner, J., Georgakakis, A., Nandra, K., et al. 2014, A&A, 564, A125
Burwitz, V., Reinsch, K., Greiner, J., et al. 2007, Adv. Space Res., 40, 1294
Burwitz, V., Reinsch, K., Greiner, J., et al. 2008, A&A, 481, 193
Cash, W. 1979, ApJ, 228, 939
CIAO Development Team 2013, CIAO: Chandra Interactive Analysis of Observations, Astrophysics Source Code Library [record ascl:1311.006]
Cowley, A. P., Schmidtke, P. C., Hutchings, J. B., Crampton, D., & McGrath, T. K. 1993, ApJ, 418, L63
Crampton, D., Hutchings, J. B., Cowley, A. P., et al. 1996, ApJ, 456, 320
den Herder, J. W., Brinkman, A. C., Kahn, S. M., et al. 2001, A&A, 365, L7
Dere, K. P., Landi, E., Mason, H. E., Monsignori Fossi, B. C., & Young, P. R. 1997, A&AS, 125, 149
Doroshenko, V. 2024, A&A, submitted [arXiv:2403.03127]
Fruscione, A., McDowell, J. C., Allen, G. E., et al. 2006, SPIE Conf. Ser., 6270, 62701V
Gänsicke, B. T., van Teeseling, A., Beuermann, K., & de Martino, D. 1998, A&A, 333, 163
Greiner, J. 2000, New A, 5, 137
Greiner, J., Hasinger, G., & Kahabka, P. 1991, A&A, 246, L17
Hachisu, I., & Kato, M. 2003a, ApJ, 588, 1003
Hachisu, I., & Kato, M. 2003b, ApJ, 590, 445
Hartmann, H. W., & Heise, J. 1996, in Supersoft X-Ray Sources, ed. J. Greiner, 472, 25
Heise, J., van Teeseling, A., & Kahabka, P. 1994, A&A, 288, L45
Huenemoerder, D. P., Mitschang, A., Dewey, D., et al. 2011, AJ, 141, 129
Ibragimov, A. A., Suleimanov, V. F., Vikhlinin, A., & Sakhibullin, N. A. 2003, Astron. Rep., 47, 186
Jimenez-Garate, M. A., Raymond, J. C., & Liedahl, D. A. 2002, ApJ, 581, 1297
Kahabka, P. 2006, Adv. Space Res., 38, 2836
Kahabka, P., & van den Heuvel, E. P. J. 1997, ARA&A, 35, 69
Kurucz, R. L. 1970, SAO Spec. Rep., 309
Lanz, T., Telis, G. A., Audard, M., et al. 2005, ApJ, 619, 517
Long, K. S., Helfand, D. J., & Grabelsky, D. A. 1981, ApJ, 248, 925
Maitra, C., & Haberl, F. 2022, A&A, 657, A26
McGowan, K. E., Charles, P. A., Blustin, A. J., et al. 2005, MNRAS, 364, 462
Nauenberg, M. 1972, ApJ, 175, 417
Nomoto, K., Saio, H., Kato, M., & Hachisu, I. 2007, ApJ, 663, 1269
Pakull, M. W., Motch, C., Bianchi, L., et al. 1993, A&A, 278, L39
Petz, A., Hauschildt, P. H., Ness, J. U., & Starrfield, S. 2005, A&A, 431, 321
Pietrzyński, G., Graczyk, D., Gallenne, A., et al. 2019, Nature, 567, 200
Rappaport, S., Di Stefano, R., & Smith, J. D. 1994, ApJ, 426, 692
Rauch, T., Orio, M., Gonzales-Riestra, R., et al. 2010, ApJ, 717, 363
Reinsch, K., van Teeseling, A., Beuermann, K., & Abbott, T. M. C. 1996, A&A, 309, L11
Reinsch, K., van Teeseling, A., King, A. R., & Beuermann, K. 2000, A&A, 354, L37
Schaeidt, S., Hasinger, G., & Truemper, J. 1993, A&A, 270, L9
Schandl, S., Meyer-Hofmeister, E., & Meyer, F. 1997, A&A, 318, 73
Seward, F. D., & Mitchell, M. 1981, ApJ, 243, 736
Southwell, K. A., Livio, M., Charles, P. A., O'Donoghue, D., & Sutherland, W. J. 1996, ApJ, 470, 1065
Suleimanov, V. F., & Ibragimov, A. A. 2003, Astron. Rep., 47, 197
Suleimanov, V., Meyer, F., & Meyer-Hofmeister, E. 1999, A&A, 350, 63
Suleimanov, V., Meyer, F., & Meyer-Hofmeister, E. 2003, A&A, 401, 1009
Suleimanov, V., Madej, J., Drake, J. J., Rauch, T., & Werner, K. 2006, A&A, 455, 679
Suleimanov, V. F., Mauche, C. W., Zhuchkov, R. Y., & Werner, K. 2015, Acta Polytechnica CTU Proceedings, 2, 143
Suleimanov, V. F., Tavleev, A. S., Doroshenko, V., & Werner, K. 2024, A&A, 688, A39
Swartz, D. A., Ghosh, K. K., Suleimanov, V., Tennant, A. F., & Wu, K. 2002, ApJ, 574, 382
Tavleev, A., Ducci, L., Suleimanov, V. F., et al. 2024, A&A, 689, A335
Trümper, J., Hasinger, G., Aschenbach, B., et al. 1991, Nature, 349, 579
van den Heuvel, E. P. J., Bhattacharya, D., Nomoto, K., & Rappaport, S. A. 1992, A&A, 262, 97
van Rossum, D. R. 2012, ApJ, 756, 43
Wilms, J., Allen, A., & McCray, R. 2000, ApJ, 542, 914
Wolf, W. M., Bildsten, L., Brooks, J., & Paxton, B. 2013, ApJ, 777, 136
Zhao, W., Meng, X., Cui, Y., & Liu, Z.-W. 2022, A&A, 666, A81